Generation, Modulation and Detection of Surface Plasmon Polaritons

McPolin, Cillian Patrick Thomas

Awarding institution:
King's College London

Generation, Modulation and Detection of Surface Plasmon Polaritons

Thesis submitted for the degree of

Doctor of Philosophy (PhD)

In the Department of Physics

By

Cillian Patrick Thomas McPolin

MSci Physics (Hons)

King's College London

September 2015

For my family

Abstract

Surface plasmon polaritons (SPPs) are electromagnetic surface waves that propagate at a metal-dielectric interface, arising from the coupling of light to free electron oscillations in metal. These plasmonic excitations offer the possibility of constructing compact optical components for use in many areas such as information technology, data storage, bio- and chemical sensing. In order to fully develop plasmonic technologies, a set of on-chip components is required to provide dynamic control over SPP signals. This includes plasmonic sources, detectors, switches and modulators, which, when combined with passive waveguiding plasmonic or dielectric structures, permit on-demand, nanoscale manipulation of optical energy flow. In this context, this thesis discusses on-chip plasmonic components based on a Vertical-Cavity Surface-Emitting Laser (VCSEL) platform. These laser diodes can be used as an electrically pumped source of plasmonic signals in various applications, as they are compact, inexpensive and power efficient. Constructing plasmonic circuitry upon a VCSEL platform would thus directly facilitate on-chip generation and waveguiding of SPPs, together with offering the capacity for signal detection. Additional plasmonic elements may be subsequently incorporated onto a laser chip to augment the functionality. This work experimentally demonstrates SPP excitation, waveguiding, frequency conversion and detection on a VCSEL based plasmonic platform, utilising diodes in direct and reverse bias. Additionally, the coupling efficiency of VCSEL emission to waveguided SPPs modes has been optimised via asymmetric plasmonic nanostructures. Modulation of plasmonic signals is also addressed by employing cavity structures that are amenable to integration with VCSELs. The principles and dynamics of mechanical, electrical and all-optical modulation using optical and plasmonic cavities have also been analysed. Ultrafast all-optical switching of SPP signals on a picosecond timescale is experimentally verified using pump-probe spectroscopy, together with mechanical control. The results demonstrate the potential of VCSEL based plasmonic circuitry, which offers immediate benefits to data transmission and storage applications, as well as sensor development.

Acknowledgements

My sincere thanks to Professor Anatoly Zayats for allowing me the opportunity to study fascinating nano-optical phenomena with his group, and for providing excellent guidance over the course of this project. I would also like to thank Doctors Gregory Wurtz and Jean-Sebastien Bouillard for all their help and insight, together with all my colleagues in the group. I am indebted to Doctors Nicolas Olivier, Daniel O'Connor and Alexey Krasavin and for their assistance with many experiments and simulations.

I would also like to thank Alexandra Henry, Andres Barborsa and Silvia Peruch. I also would not be able to undertake this project without the support of my friends and family, for which I am very grateful.

Lastly, I am thankful to the EPSRC for funding for this research.

Table of Contents

List of Figures

List of Tables

List of Publications

Conference Papers:

- C. McPolin, N. Olivier, J.-S. Bouillard, D. O'Connor, A. Krasavin, W. Dickson, G. Wurtz, A. Zayats, Ultrafast All-Optical Switching of Surface Plasmon Polariton Modes via Fano Resonances, *Talk at CLEO/Europe-EQEC Conference* (Munich, 2015)

- C. McPolin, J.-S. Bouillard, D. O'Connor, A.V. Krasavin, W. Dickson, J. Justice, B. Corbett, G. A. Wurtz, and A. V. Zayats, Directional Excitation of Surface Plasmon Polaritons by Vertical-Cavity Surface Emitting Lasers, *Talk at the Institute of Physics Conference, Photon 14* (London, 2014)

- C. McPolin, J.-S. Bouillard, D. O'Connor, A.V. Krasavin, W. Dickson, G. A. Wurtz, and A. V. Zayats, Experimental Demonstration of Plasmonic Switching via Optical Cavity Resonances, *Talk at 13th International Conference on Near-field Optics, Nanophotonics and Related Techniques* (Salt Lake City, 2014)

- C. McPolin, J.-S. Bouillard, D. O'Connor, A. V. Krasavin, W, Dickson, G. A. Wurtz, A. V. Zayats, Dynamic Switching Of Plasmonic Signals Via Optical Cavity Resonances, *Talk at Condensed Matter in Paris Conference* (Paris, 2014)

- C. McPolin, J.-S. G. Bouillard, D. O'Connor, A. V. Krasavin, W. Dickson, G. A. Wurtz, and A. V. Zayats, Experimental Demonstration of Plasmonic Switching via Optical Cavity Resonances, *Talk at SPIE Photonics Europe, Nanophotonics Conference* (Brussels, 2014).

- C. McPolin, N. Olivier, J.-S. Bouillard, D. O'Connor, A. Krasavin, W. Dickson, G. Wurtz and A. Zayats, Ultrafast plasmonic switching via optical cavity modes, *Poster at Faraday Discussions on Nanoplasmonics* (London, 2015)

- C. McPolin, J.-S. G. Bouillard, D. O'Connor, W. Dickson, G. A. Wurtz, and A. V. Zayats, Selective control of plasmonic modes in resonant cavities using spatial engineering of losses and boundary conditions, *Poster at 13th International Conference on Near-field Optics, Nanophotonics and Related Techniques* (Salt Lake City, 2014)

- C. McPolin, D. O'Connor, J.-S. Bouillard, A. V. Krasavin, W. Dickson, G. A. Wurtz, and A. V. Zayats, A Plasmonic switch based on Electrically Controlled Cavity resonances, *Poster at CLEO/Europe-IQEC Conference* (Munich, 2013)

- C. McPolin, D. O'Connor, J.-S. Bouillard, A. V. Krasavin, W. Dickson, G. A. Wurtz, and A. V. Zayats, A Plasmonic Switch based on an Optically Controlled Nonlinear Cavity, *Poster at 12th International Conference on Near-field Optics, Nanophotonics and Related Techniques* (San-Sebastian, 2012)

Journal Papers:

- C. P. T. McPolin, N. Olivier, J.-S. Bouillard, D. O'Connor, A. V. Krasavin, W. Dickson, G. Wurtz, and A. V. Zayats, Universal switching of plasmonic signals using optical resonator modes (in preparation)

- C. P. T. McPolin, J.-S. Bouillard, S. Vilain, A. V. Krasavin, W. Dickson, D. O'Connor, G. Wurtz J. Justice, B. Corbett, and A. V. Zayats, Integrated plasmonic circuitry on a Vertical-Cavity Surface-Emitting Semiconductor Laser Platform (Nature Communications – Accepted)

Patents:

- C. McPolin, G. Wurtz, and A. Zayats, Plasmonic Switch,
  UK Patent Application No. 1400393.3, filed 2014

Chapter 1

Introduction

In this introductory chapter, we will discuss the challenge of constructing components for the manipulation of optical energy on the nanoscale within the broader context of superseding current electronic devices. Plasmonic technology is explored as a potential route to achieving nano-optical circuitry, when implemented via a Vertical-Cavity Surface-Emitting Laser platform.

1.1 Nanophotonic Circuitry

The late 20th and early 21st centuries have witnessed the large-scale adoption of various new technologies for communication and computation, dramatically altering modern society in the process. This revolution may be traced back to the advent of the telephone, and subsequently the transistor, which paved the way for personal computers, mobile telephones and the Internet. Such is the prevalence of new technologies that the current period is often referred to as the 'Information Age'[1]. The plethora of benefits associated with these innovations drives their rapid development, and consequently new global industries have grown in a comparatively short period of time.

Therefore, as modern societies are becoming increasingly reliant on electronic devices, there is a constant demand for the manufacture of faster, smaller components that provide ever-greater functionality. Computational power must increase accordingly, with Moore's law dictating that the number of transistors in integrated circuits should approximately double every two years[2]. Nonetheless, this trend cannot continue indefinitely, as limiting factors become increasingly significant, including cross talk between wires, quantum mechanical effects, resistive-capacitive (RC) delay and increased power consumption[3].

As a result, one of the current aims of nanotechnology is the replacement of 'slow' electronic devices with 'fast' photonic, light based, ones[4]. Optical components would thus send data via photons as opposed to electrons, permitting higher transmission rates whilst not suffering from electronic limitations such as RC delay.

This necessitates the development of an optical analogue of the electronic integrated circuit, facilitating optical signal processing, routing and control. However, free space electromagnetic waves cannot be localised into nanoscale regions much smaller than the wavelength of light in the material, due to the diffraction limit, which stems from the wave nature of light and its interaction with optical systems. From the pioneering work of Abbe (1873)[5] and Rayleigh (1896)[6], the smallest resolvable distance δ_x is approximately[7]:

$$\delta_x \approx \lambda / 2 \tag{1.1}$$

Another consequence of the diffraction limit, as defined by Equation 1.1, is that light beams cannot be focused into spots smaller than this critical dimension. Nevertheless, this is not a fundamental limit, as there are many approaches that allow it to be overcome. For instance, the novel properties of evanescent fields provide opportunities for nano-optical physics and technology.

Freely propagating light waves are characterised by wavevectors (k) where all the spatial components are real:

$$k = \sqrt{k_x^2 + k_y^2 + k_z^2} \tag{1.2}$$

where $k = 2\pi / \lambda$ and λ denotes the wavelength. In contrast, an evanescent field contains a least one spatial component that is imaginary, corresponding to exponential amplitude decay in that direction, which permits the residual components to exceed the free space momentum. If we consider an evanescent wave where k_z is imaginary and $k_x > k$, there is confinement in the z direction due to the rapid field decay[7,8], potentially offering localisation beyond Equation 1.1 in one dimension. Furthermore, the diffraction limit may also be associated with the uncertainty principle, and in this regard, increasing k_x ensures a larger momentum component p_x, as $p_x = \hbar k_x$. As a result, this allows for a smaller positional uncertainty for photons in the x direction[9]. Moreover, a practical means of confining and manipulating optical energy on subwavelength scales with evanescent fields entails harnessing the coupling of light to plasma oscillations in metals.

1.2 Plasmonics

One approach to circumventing the free-space diffraction limit involves

exploiting the properties of excitations known as surface plasmon polariton (SPPs), which are surface waves propagating at metal-dielectric interfaces due to the coupling of light to free electron oscillations in the metal. Owing to their evanescent nature, SPPs offer the possibility of constructing compact optical components. In this respect, a fully functional plasmonic circuit would provide the speed and bandwidth of photonic networks, whilst maintaining the nanoscale dimensions of electronic circuits[10].

The propagation, localisation and guidance of plasmonic modes are studied within the field of plasmonics, which continues to attract considerable attention, due in part to the wide range of potential applications for plasmonic devices, including within areas such as information storage, data transmission, and sensing. Research into SPP based optics has recently experienced rapid progress, partially a result of parallel advances in nano-fabrication and characterisation techniques, as evidenced by the fivefold increase in the number of plasmonic papers published between 2001 and 2011[11]. Furthermore, plasmonic effects have also been unknowingly employed for centuries to create vibrant colours in glass.

(a) (b)

Figure 1.1 The Roman Lycurgus cup as viewed in (a) reflection (b) transmission. Used with permission from the British Museum. The colour change is a result of the presence of gold-silver alloy nanoparticles in colloidal form, typically 50-100 nm in diameter, which support localised surface plasmons – excitations distinct from SPPs, as discussed in Chapter 2.

The Lycurgus cup, which most likely originates from fourth century Rome, is a famous example of early plasmonic technology. The cup appears a striking red when viewed in transmission, whilst displaying a green colour in reflection. Its remarkable optical properties derive from the embedded metal nanoparticles that strongly absorb in the green region of the visible spectrum. Unfortunately, the methods involved in the creation of the cup proved difficult to replicate, and thus it remains a

unique example of Roman nanotechnology[12]. Similarly, medieval stained glass windows have also harnessed the optical properties of metallic nanoparticles to produce impressive displays of colour.

The emergence of scientific field of plasmonics began in the early 20th century, which included the establishment of a mathematical foundation for nanoparticle scattering that is utilised for staining glass[13]. Plasmonic effects were responsible for the anomalous decreases in intensity exhibited by reflection spectra of gratings, as observed by Wood in 1902[14]. During the same period, Sommerfeld and Zenneck laid the groundwork for mathematically describing surface waves in the context of radio waves[15,16], which was later followed by their excitation with visible light[17]. In addition, the electron diffraction experiments of Ritchie[18] illustrated unexpected peaks, with the energy loss subsequently explained in terms of surface plasmon oscillations. Thus, a cohesive description of all these phenomena in terms of plasmonic excitations was subsequently developed. However, the technology of this period did not allow the unique optical properties of these hybrid surface modes to be fully exploited.

The current resurgence in the study of plasmonics arguably began with the work of Ebbesenn, which illustrated extraordinary transmission in gratings due to plasmonic modes[19]. Recent developments in fabrication, characterisation and simulations tool have all greatly enhanced nano-optical research, which, over the past decade and a half, has highlighted the advantageous properties of plasmonic modes. This includes the large near-fields sustained by plasmonic excitations, which are ideal for sensing functions[20] and Surface Enhanced Raman Spectroscopy (SERS)[21]. Furthermore, the large field enhancements also provide opportunities for exploring nonlinear optical phenomena on the nanoscale[22]. Plasmonic technology is currently being employed in pregnancy tests, which entails gold nanoparticles clustering in presence of hormones[23]. Other areas that exhibit promise include information storage[24], localised heating[25], cancer treatment[23], solar cells[26] and applications involving water heating[27]. Crucially, the evanescent nature of SPPs provides the opportunity for developing nano-optical circuitry, which is the focus of this thesis.

In order to enable plasmonic excitations to be fully utilised in real life applications we require on-chip components for the dynamic control of SPPs[28]. Broadly speaking, there are four main categories of components, namely switches,

modulators, sources and detectors, which, when combined with passive waveguides, allow for the full manipulation of optical signals on the nanoscale. Research focused on SPP control has been termed 'Active Plasmonics', and is the subject of considerable effect, with numerous papers recently addressing the challenge[29,30].

At the juncture, it is important to note that other technologies are currently being developed for on-chip photonic circuitry, such as the endeavours of the team at IBM[31]. Nonetheless, the case for plasmonics has been extensively argued, due to the remarkable energy confinement it offers, together with the ability to guide optical signals on subwavelength scales. Plasmonics also naturally interfaces with dielectric photonics and semiconductor electronics, thereby promoting synergy between the two areas[4,32-34].

In this context, the successful establishment of a plasmonic platform requires an integrated, on-chip optical or electrical source to efficiently excite SPPs. As this represents the starting point of any circuit, it is important that the efficiency is high, such as to prevent an energy bottleneck from forming.

1.3 Vertical-Cavity Surface-Emitting Lasers

Vertical-Cavity Surface-Emitting Lasers (VCSELs) are a promising candidate for an on-chip optical source to couple to plasmonic modes as they are compact, reliable, inexpensive and power-efficient. VCSELs produce an output beam perpendicular to the wafer, in contrast to conventional edge-emitting lasers. This is achieved via the use of distributed Bragg reflectors (DBRs) to clad the active layer, giving rise to a vertical cavity[35]. VCSELs currently have the second highest production volume of all semiconductor lasers, with numerous current applications including data transmission, optical mice and printing[36]. Modulation speeds are also steadily increasing – commercial VCSELs are able to attain rates of around 25 Gbit/s. In 2013, the global market of VCSELs was worth approximately 300 million GBP, with a projected increase of 33% per year, reaching 1.3 billion by 2018[37]. Considering VCSELs were first commercialised in 1996[38], this represents significant, rapid growth. Resultantly, a considerable industry is already in place for VCSEL development and manufacture, ensuring that plasmonic components based on this technology are close to realisation and mass production.

VCSELs are composed of p-n junctions, enabling their operation as photodetectors[39], and consequently may serve dual roles as an optical source for SPP excitation and as a detector of SPPs. The planar structure of these laser diodes also makes them amenable to integration with other components, which may provide added functionality such as signal switching and modulation. Evidently, VCSELs may provide an effectual platform for implementing plasmonic circuitry, stemming from their advantageous optical characteristics and already established nature.

As an aside, whilst it is important to investigate new technologies, and indeed market forces drive a significant amount of research, the ability to glean new insights into the how the universe operates is its own reward. When investigating phenomena in any scientific area, one may become lost in details and lose sight of how remarkable it is that we can model the natural world and, to an increasingly larger extent, control its workings. Within the area of optics, we are able to manipulate lights waves to send signals with structures so small that they are invisible to the naked eye. At the other extreme, light from distant stars gives us clues as to their distance, temperature and even chemical composition. In fact, 2015 has been proclaimed the Year of Light by UN General Assembly[40], highlighting its already critical role in our daily lives, together with the promise for future technologies.

1.4 Thesis Structure

In this context, this thesis discusses on-chip plasmonic components based on a VCSEL platform. Firstly, we address the development of a VCSEL compatible with plasmonic components, in terms of its design and manufacture. Following fabrication, manipulation of SPPs on VCSELs is both numerically and experimentally investigated. Additional structures for directing and switching SPP signals on VCSELs are also explored, including optical and plasmonic Fabry Perot cavities. The overall thesis structure is thus as follows:

Chapter 1 – *Introduction*

This chapter addresses the aim of this thesis and the underlying motivation within the context of nanophotonic circuitry.

Chapter 2 – *Theory of Plasmonic Excitations*

We examine the characteristics of fundamental plasmonic modes, along with the optical excitation of SPPs in this chapter.

Chapter 3 – *Vertical-Cavity Surface-Emitting Lasers*

An outline of the properties of VCSELs is presented in this chapter.

Chapter 4 – *Experimental and Numerical Procedures*

The methods employed for the numerical modeling of plasmonic structures is discussed in this chapter, together with the experimental fabrication and characterisation techniques.

Chapter 5 – *Plasmonic components based on VCSELs*

The design and experimental demonstration of VCSELs integrated with plasmonic components is addressed in this chapter.

Chapter 6 – *Directional Excitation of SPPs on VCSELs*

This chapter explores directional coupling of SPPs via scattering structures.

Chapter 7 – *Modulation of SPPs using Cavity Structures*

In this chapter, we investigate controlling SPP excitation and propagation with cavity structures that are amenable to integration with VCSELs.

Chapter 8 – *Conclusions and Outlook*

This chapter draws conclusions from all the work addressed in this thesis, and discusses possible future avenues for investigation

Chapter 2

Theory of Plasmonic Excitations

This chapter presents an overview of the fundamentals of plasmonic excitations, including planar, coupled and localised modes. In addition, various practical means of coupling free space radiation to surface plasmon polaritons are also discussed, with an emphasis on attaining high efficiencies.

2.1 Plasmonic Excitations

The field of plasmonics addresses the physics and technology that is based on exploiting the coupling of electromagnetic radiation to coherent charge density oscillations in nanostructured metals. As its name suggests, the area is theoretically linked to plasma physics, for metals may be considered as free electron plasmas. Incredibly, it has been estimated that approximately 99% of the visible universe exists in a plasma state, spanning 32 orders of magnitude, from metallic films (10^{-9} m) to the gaseous plasmas of extragalactic objects (up to 10^{23}m)[41]. In the nanoscale regime, harnessing the interaction between photons and plasma oscillations allows for the unprecedented manipulation of optical energy on scales below the diffraction limit, making plasmonics an integral area within nanophotonics.

Plasmonic modes in metals were perhaps first explicitly illustrated in the experiments of Ruthemann and Lang, which entailed bombarding thin metal films with fast electrons and subsequently monitoring the energy of those that were undeflected. Their work displayed unexpected peaks spaced apart by 16 eV, with result later rationalised by Pines and Bohm in terms of the Coulomb interaction between the metal's valence electrons, which gives rise to longitudinal oscillations of the collective excitation of the electron density. As a consequence, the name 'plasmon' was coined to describe these excitations that possess an energy of $\hbar\omega_P$, where ω_P is the plasma frequency. In this regard, a plasmon is a quantum of plasma oscillation, in a similar respect to a photon representing of a quantum of electromagnetic radiation oscillation. Neglecting losses, these 'bulk' plasmons thus occur at the metal's plasma frequency ω_p, corresponding to longitudinal modes.

Moreover, electromagnetic waves may propagate in the material at frequencies above ω_p, and are often referred to as bulk plasmon polaritons. It is worth noting that the term polariton refers a quasi-particle that arises due to the coupling of light to a fundamental excitation of a system, which in this case is the bulk plasmon. Hence, bulk plasmonic excitations may take the form of 'pure' modes (longitudinal waves not coupled to photon fields), or modes combined with electromagnetic fields – bulk plasmon polaritons (transverse waves affected by the presence of free electrons).

Following on from this initial work, Ritchie investigated plasmonic modes in thin films, and postulated that, owing to the influence of the boundaries, another excitation would exist, possessing a reduced energy of $\hbar\omega_P/\sqrt{2}$ in vacuum. This was later confirmed by the electron energy loss experiments of Powell and Swan, with the excitations hence referred to as surface plasmons (SPs). At energies below $\hbar\omega_P/\sqrt{2}$, SPs exist in combination with a photon field, with this mixed mode often referred to as a surface plasmon polariton (SPP)[42].

2.1.1 Surface Plasmon Polaritons

The novel optical properties of SPPs are apparent from their dispersion relation, which may be derived by considering Maxwell's equations, with the appropriate boundary conditions, as shown by Raether[43]. Firstly, we define two semi-infinite half spaces, as outlined in Figure 2.1, where ε_1 refers to a dielectric permittivity and ε_2 is the complex permittivity of a metal, with $\varepsilon_2 = \varepsilon_2' + i\varepsilon_2''$.

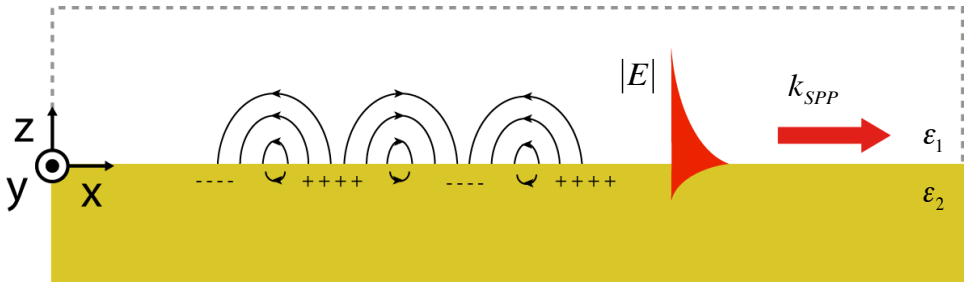

Figure 2.1 Electric field of a Surface Plasmon Polariton excitation propagating at metal (ε_2) – dielectric (ε_1) interface, with the wavevector given by k_{SPP}. The surface charge distribution, together with accompanying electric field lines, are also shown.

To begin, we consider a TM-polarised wave propagating the x direction, without any y dependence. The fields in the two media may be consequently written as:

$z > 0$

$$\boldsymbol{H}_1 = (0, H_{y1}, 0) \exp i(k_{x1}x + k_{z1}z - \omega t) \tag{2.1}$$

$$\boldsymbol{E}_1 = (E_{x1}, 0, E_{z1}) \exp i(k_{x1}x + k_{z1}z - \omega t) \tag{2.2}$$

$z < 0$

$$\boldsymbol{H}_2 = (0, H_{y2}, 0) \exp i(k_{x2}x - k_{z2}z - \omega t) \tag{2.3}$$

$$\boldsymbol{E}_2 = (E_{x2}, 0, E_{z2}) \exp i(k_{x2}x - k_{z2}z - \omega t) \tag{2.4}$$

These equations must satisfy the corresponding boundary conditions of the continuity of the tangential components of the E and H fields, along with the conservation of the normal displacement field D_z:

$$\varepsilon_1 E_{z1} = \varepsilon_2 E_{z2} \tag{2.5}$$

$$E_{x1} = E_{x2} \tag{2.6}$$

$$H_{y1} = H_{y2} \tag{2.7}$$

Where $D_z = \varepsilon E_z$ (constitutive relation). We relate equations 2.1-2.4 to Maxwell's equations:

$$\nabla \cdot \boldsymbol{D} = \rho_{ext} \tag{2.8}$$

$$\nabla \cdot \boldsymbol{B} = 0 \tag{2.9}$$

$$\nabla \times \boldsymbol{E} = -\frac{\partial \boldsymbol{B}}{\partial t} \tag{2.10}$$

$$\nabla \times \boldsymbol{H} = \boldsymbol{J}_{ext} + \frac{\partial \boldsymbol{D}}{\partial t} \tag{2.11}$$

together with the boundary conditions 2.5-2.7, to obtain an expression for each component of the wavevector in two half spaces:

$$k_{z1} = \frac{\omega}{c}\sqrt{\frac{(\varepsilon_1)^2}{\varepsilon_1 + \varepsilon_2'}} \tag{2.12}$$

$$k_{z2} = \frac{\omega}{c}\sqrt{\frac{(\varepsilon_2')^2}{\varepsilon_1 + \varepsilon_2'}} \tag{2.13}$$

$$k_x = \frac{\omega}{c}\sqrt{\frac{\varepsilon_1\varepsilon_2}{\varepsilon_1+\varepsilon_2}} \tag{2.14}$$

In the case where $\varepsilon_2' < 0$ and $\left|\varepsilon_2'\right| > \varepsilon_1$, the k_z components in both half spaces are purely imaginary. Consequently k_x corresponds to the propagation constant, with the SPP dispersion given by (2.14), which may be rewritten as:

$$k_{SPP} = k_0\sqrt{\frac{\varepsilon_d\varepsilon_m}{\varepsilon_d+\varepsilon_m}} \tag{2.15}$$

Where ε_m and ε_d are the permittivities of the metal and dielectric respectively, with k_0 referring to the free space wave vector. We may also write the dispersion in terms of the effective SPP index n_{SPP}, and thus Equation 2.15 becomes $k_{SPP} = k_0 n_{SPP}$. As before, we will denote the frequency dependent complex permittivity of the metal as $\varepsilon_m = \varepsilon_m' + i\varepsilon_m''$ and following this, the complex SPP wavevector will be written as $k_{SPP} = k_{SPP}' + ik_{SPP}''$, where k_{SPP}' refers to the oscillatory portion of the wave and k_{SPP}'' corresponds to the decay along the direction of propagation[42]. As we consider the SPP wavevector to be complex, the SPP frequency is thus exclusively real. Moreover, further analysis reveals that no surface modes exist for TE polarisation[44], and hence SPPs are TM polarised waves on a flat interface.

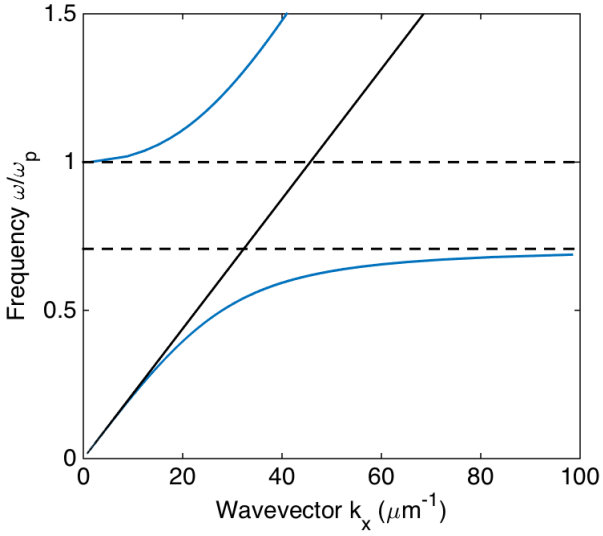

Figure 2.2 SPP dispersion relation (blue line) plotted where $\varepsilon_d = 1$ and ε_m relates to a Drude metal without losses (Equation 2.17). The black solid line corresponds to the dispersion of light in the dielectric. The dashed lines relate to the plasma ω_P and surface plasmon ω_{SP} frequencies, with $\omega_{SP} \approx 0.71\omega_P$.

As SPPs possess imaginary k_z components in the two media, the amplitude exhibits a rapid, exponential decay from the interface. This allows k_x to exceed the dielectric wavevector, $\varepsilon_1^{1/2}k_0$, and as a result SPPs represent a surface wave propagating at a dielectric-metal interface, evanescently confined in the perpendicular direction. These excitations are sustained by the interface due to the longitudinal surface charge oscillation. Another noteworthy property of SPPs is that the excitations possess both transverse and longitudinal electric field components.

Equation 2.15 is valid for real and complex permittivities, and therefore the dispersion may be plotted for a metal without losses, as shown in Figure 2.2 via Equation 2.17. The Drude dielectric function may be written as:

$$\varepsilon(\omega) = 1 - \frac{\omega_P^2}{\omega^2 + i\gamma\omega} \tag{2.16}$$

where ω_p again is the plasma frequency, and defined as $\omega_P = \sqrt{n_e e^2/\varepsilon_0 m}$, n_e the density of free electrons, e the negative electronic charge, ε_0 the permittivity of free space, m the electronic mass and $\gamma = 1/\tau$, with τ being the relaxation time of the free electron gas - we are considering the conduction electrons as a free electron gas. Moreover, for negligible damping we may write:

$$\varepsilon(\omega) = 1 - \frac{\omega_P^2}{\omega^2} \tag{2.17}$$

This relation is used to plot the SPP dispersion in Figure 2.2, where the linear dispersion of light is also plotted for comparison. In this case, $n\omega = ck$, with the refractive index $n = \sqrt{\varepsilon_d} = 1$ and c denoting the speed of light.

Looking at Figure 2.2, we can quickly indentify three regions:

1. Above ω_p the dispersion curve lies within the light cone, and relates to propagating waves in the material (Brewster modes).
2. Between ω_P and ω_{SP} there is a gap where propagation is forbidden.
3. Below ω_{SP}, the wavevectors of the dispersion curve exceed light in the adjacent dielectric, and thus correspond to evanescently confined waves (SPPs).

Therefore, at frequencies below ω_{sp}, in region 3, the surface wave consists of a surface plasmon polariton. As the dispersion curve of SPPs lies to the right of the light line, the large momenta of these modes ensures that they cannot radiate light or be excited by conventional illumination from the dielectric. For small wavevectors, the dispersion curve resides close to the light line and in this regime SPPs resemble grazing incidence light. However, as the frequency approaches the asymptotic limit, the surface plasmon frequency $\omega_{SP} = \omega_P / \sqrt{\varepsilon_d + 1}$, SPPs acquire a more electrostatic character and the group velocity $v_g = \partial\omega / \partial k$ vanishes, with the longitudinal and transverse electric field components becoming equal. This occurs when the permittivity of the metal and adjacent dielectric become equal in magnitude, whilst also opposite in sign[45], and thus from equation 2.15, $k \to \infty$. Moreover, whilst the energy flux stays the same, the energy density increases.

It is important to consider that real metals exhibit free electron and interband damping, which will modify the SPP dispersion, resulting in the curve reaching a maximum, finite wavevector and the bandgap disappearing. As an example, Equation 2.15 is plotted in Figure 2.3, with the permittivities of gold and silver taken from the experimental data of Johnson and Christy[46], in addition to the Drude model:

$$\varepsilon(\omega) = \varepsilon_\infty - \frac{\omega_P^2}{\omega^2 + i\gamma\omega} \tag{2.18}$$

where the first term ε_∞ is the contribution due to the interband transition, which is unity for a perfectly free electron gas, as in Equation 2.16. Furthermore, additional Lorentz oscillator terms may be added to account for the wavelength dependence of ε_∞. The terms used in the Drude model in Figure 2.3 for silver were: $\varepsilon_\infty = 3.7$, $\omega_p = 9.2\ \text{eV}$, $\gamma = 0.02\ \text{eV}$ and for gold: $\varepsilon_\infty = 6.9$, $\omega_p = 8.9\ \text{eV}$, $\gamma = 0.07\ \text{eV}$ (data taken from reference 47).

The experimental SPP dispersion for silver exhibits an obvious plasmonic lineshape as the curve bends back across the light line, which it then approaches from within the light cone (Figure 2.3b). In contrast, the experimental SPP dispersion on gold only displays a bump, approaching the light line from the right (Figure 2.3a). This difference in lineshape can be attributed to the higher losses of gold compared to silver, as shown by Figure 2.3d, which highlights the onset of interband transitions that occur at 2.3 eV and 3.9 eV for gold and silver respectively.

These interband transitions are not accounted for by Equation 2.18, and thus SPP dispersion plotted with the Drude model of gold also displays the back bending (Figure 2.3a) [44, 47, 48].

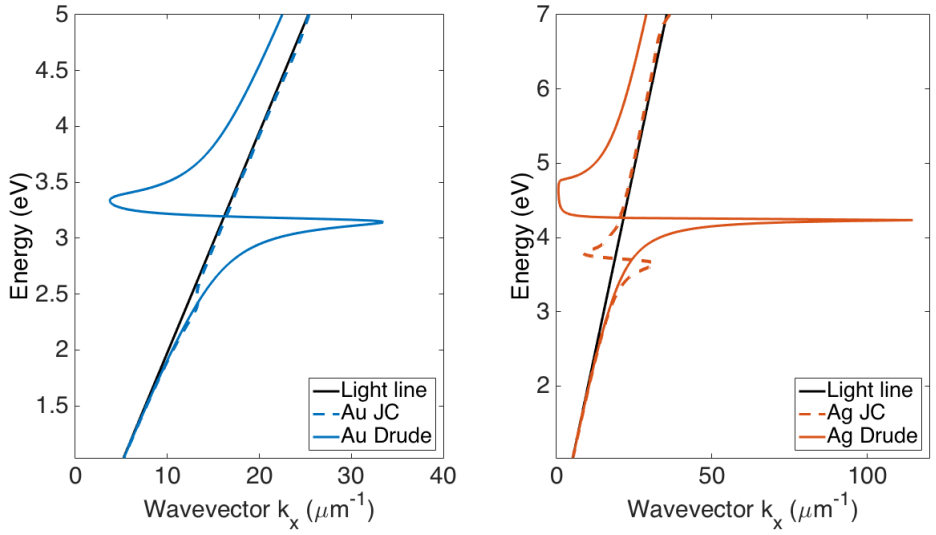

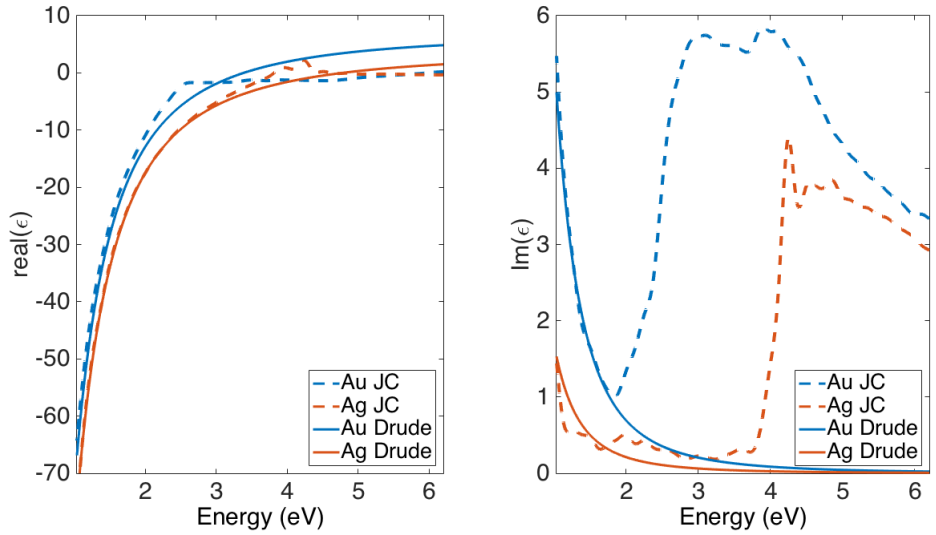

Figure 2.3 (a) Dispersion of SPPs at a gold-air interface. Solid blue line corresponds to the Drude model, whilst dashed blue line is calculated with the Johnson and Christy permittivity. (b) Dispersion of SPPs at a silver-air interface. Solid red line corresponds to the Drude model, whilst dashed red line is calculated with the Johnson and Christy permittivity. (c) Real part and (d) Imaginary parts of the permittivities of gold and silver for the Johnson and Christy experimental data and the Drude model (Equation 2.18).

Many aspects of SPPs can be appreciated from the dispersion relation, such as the confinement of energy to the interface, which results from the propagation

constant exceeding the wavevector in the dielectric. This localisation is characterised by the penetration depth of the field into the dielectric, which is defined as:

$$\delta_d = \frac{1}{k_0}\left|\frac{\varepsilon'_m + \varepsilon_d}{\varepsilon_d^2}\right|^{\frac{1}{2}} \tag{2.19}$$

Similarly, the penetration into the metal may be written as[45]:

$$\delta_m = \frac{1}{k_0}\left|\frac{\varepsilon'_m + \varepsilon_d}{(\varepsilon'_m)^2}\right|^{\frac{1}{2}} \tag{2.20}$$

Both of these penetration depths are defined as the distance over the field decays to $1/e$ of its original strength.

It is significant that as the real part of the SPP wavevector increases, so too does the localisation; however, the propagation length is concurrently decreased due to ohmic damping in the metal. As a result, there is a trade off between localisation and loss - a common theme in plasmonics. Furthermore, as the k-vector of SPPs is increased with respect to free space radiation, the wavelength correspondingly decreases:

$$\lambda_{SPP} = \frac{2\pi}{k'_{SPP}} = \lambda_0\sqrt{\frac{\varepsilon_d + \varepsilon'_m}{\varepsilon_d \varepsilon'_m}} \tag{2.21}$$

Losses in the metal (Joule heating) result in a finite propagation length, which is defined as the distance over which the power or intensity of the SPP excitations falls to $1/e$ of its initial value, and may be written as:

$$L_{SPP} = 1/2k''_{SPP} \tag{2.22}$$

In order to better appreciate the scales that we are considering, a number characteristic lengths are given in Table 1 for three wavelengths.

Considering Table 1, it is clear that as the free space wavelength increases from 650 nm to 1050 nm, the SPP effective index decreases and hence the fields resides more in the dielectric than the metal. Evidently, long-range modes exist in the infra-red regime, whilst highly confined SPPs are available in visible. Whilst plasmonics is an attractive means of achieving high confinement of EM waves, alternative

technologies exist, such as silicon photonics, where silicon is the optical medium. This is being actively developed by both IBM[49] and Intel[50], and may permit integrated optical chips that offer high speeds, together with low power consumption, to be fabricated using existing techniques.

Table 1. SPP characteristic lengths calculated for a gold-air interface (Johnson and Christy data).

λ_0 (nm)	λ_{SPP} (nm)	$\mathrm{Re}(n_{SPP})$	δ_d (nm)	δ_m (nm)	L_{SPP} (μm)
650	624	1.04	358	28	14
850	835	1.02	708	25	59
1050	1039	1.01	1135	24	104

Considering the refractive index of silicon to be $n \sim 3.48$, a waveguide may achieve a size as small as $\lambda_0 / n \sim 450nm$ at a free space wavelength of 1550 nm. This is greater confinement than SPPs attain at a single air-gold interface, where the penetration depth into the dielectric is $\delta_d = 2645nm$ at the same wavelength. In addition, only near ω_{SP} do SPPs attain sub-diffraction limit (i.e. below half the dielectric wavelength) field localisation[44]. Thus, the data in table 1 does not represent substantial optical confinement. However, plasmonic components may achieve greater nanoscale confinement in dual interface structures, whilst silicon photonics is hindered by the diffraction limit, which presents a challenge for high integration of silicon based optical components. This dimensional mismatch between silicon photonics and electronics is one of the motivations behind combining the two areas - 'Silicon Plasmonics'[51, 52]. This would allow photonic components to achieve nanoscale dimensions, whilst also enhancing the manipulation of optical signals in silicon. What is more, a plethora of other materials that support plasmonic modes are also the subject of considerable research, including titanium nitride and graphene[47, 53], in an effort to surpass the performance

of gold and silver. Lastly, whereas losses in silicon photonics are no longer a major concern, the relatively short propagation lengths of plasmonic modes (on the order of microns) is another limitation which must be addressed. For instance, incorporating gain media[44] into waveguides may serve to offset losses.

2.1.2 Slot Plasmon Modes

If we consider a three-layer geometry composed of Metal-Insulator-Metal (MIM) films, the SPPs at the two metal-dielectric interfaces may couple, provided the insulator thickness is similar to, or smaller than, the decay length of the plasmonic modes in that material. These excitations may be denoted as slot, MIM or gap modes, and offer the possibility of greater confinement of optical energy compared to single interface SPPs, as previously discussed.

An example of an MIM waveguide is a subwavelength slit aperture in a metallic film, which may possess plasmonic modes with symmetric or anti-symmetric electric field profiles. The symmetry of these modes can be defined in terms of their field or charge distribution profiles; here we will define it with respect to the transverse electric field component (as outlined in Figure 2.4b). The respective dispersion relations for the symmetric and anti-symmetric modes propagating in the x direction, are:

$$\tanh\left(\frac{w}{2}\sqrt{k_x^2 - k_0^2\varepsilon_d}\right) = -\frac{\varepsilon_d\sqrt{k_x^2 - k_0^2\varepsilon_m}}{\varepsilon_m\sqrt{k_x^2 - k_0^2\varepsilon_d}} \tag{2.23}$$

$$\tanh\left(\frac{w}{2}\sqrt{k_x^2 - k_0^2\varepsilon_d}\right) = -\frac{\varepsilon_m\sqrt{k_x^2 - k_0^2\varepsilon_d}}{\varepsilon_d\sqrt{k_x^2 - k_0^2\varepsilon_m}} \tag{2.24}$$

where w is the width of the waveguide and k_x is the propagation constant. In the case of normal illumination of a slit with TM polarised light, only the low-energy, symmetric mode (Equation 2.23) may be excited due to phase matching. Moreover, this is only slot mode that does not experience cut-off, meaning that in theory as the gap size goes to zero, $k_x \to \infty$. The dispersion for this excitation is plotted for a range of waveguide widths in Figure 2.4a, using the approximation $\tanh(x) \approx x$, which is valid for small values of w[54].

As displayed in Figure 2.4a, reducing the gap width from 100 nm to 25 nm increases the effective index and lowers the plasmonic wavelength. Consequently the slot mode becomes more confined, however at the cost of smaller propagation length. This reduced gap results in larger Coulomb forces that yield greater surface charge accumulation and near-fields. Nonetheless, for large gap widths, on order of microns, slot modes may in fact exhibit higher propagation lengths, together with greater confinement, than single interface SPPs[54,55,56]. This may be rationalised in terms of the electric field approaching a capacitor mode, yielding a constant field across the gap. Thus the energy in the gap is increased, which leads to less ohmic damping in the metal.

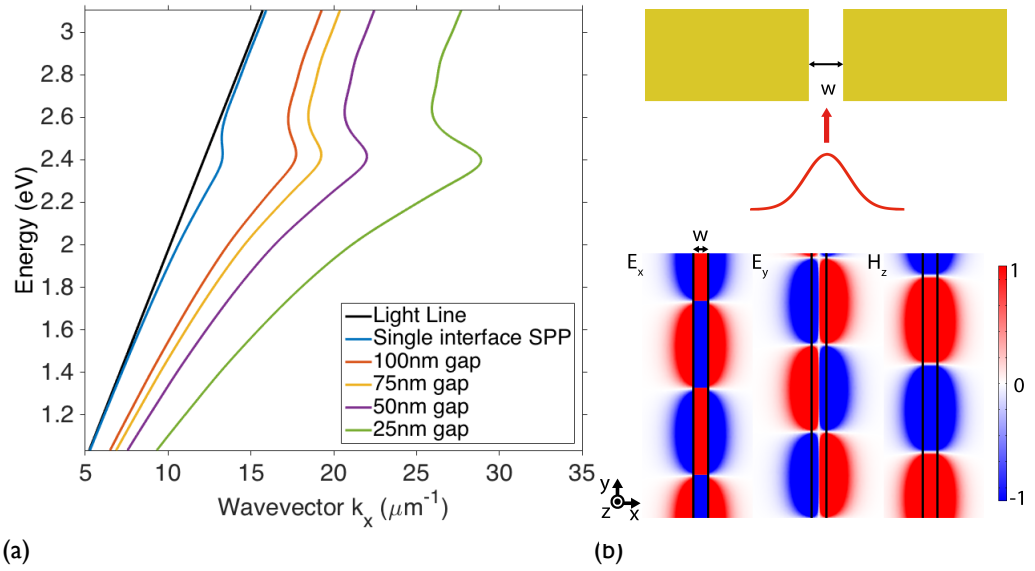

Figure 2.4 (a) Equation 2.23, the symmetric slot mode dispersion, plotted for different insulator thickness, where $\varepsilon_d = 1$ and ε_m is again taken from Johnson and Christy. Decreasing the gap results in a slower mode as the effective index grows. (b) Excitation of the symmetric mode in a nanoslit by employing a Gaussian beam. Top: Schematic of normal incidence illumination of a nanoslit. Bottom: Simulation showing the electric and magnetic field components of the symmetric slot mode. Each field profile has been normalised to the maximum value of that component.

The inverse geometry, namely an Insulator-Metal-Insulator (IMI) trilayer, also supports coupled excitations. These dispersions relations are equivalent to equations 2.23 and 2.24, but with ε_m and ε_d terms switched. IMI waveguides may support asymmetric modes with significantly longer propagation lengths compared to single interface SPPs, again as the fields reside more in the dielectric than the metal. Employing MIM and IMI waveguides plainly offers increased flexibility over the

localisation and propagation of plasmonic excitations; however, not all plasmonic excitations propagate.

2.1.3 Localised Surface Plasmons

As we have discussed, SPPs are dispersive electromagnetic excitations propagating at a planar metal-dielectric interface. However another distinct category of plasmonic excitation is supported by bounded geometries - localised surface plasmons (LSPs). These are non-propagating modes that arise due the confinement of the conduction electrons to a small volume. LSPs are characterised by complex frequencies that are dependent on the size and shape of the object, in addition to the local dielectric environment[57].

A metallic sphere with subwavelength dimensions is perhaps the simplest example of a structure that supports LSPs. Upon illumination, the conduction electrons are displaced by the electric field, with a restoring force originating from the Coulomb attraction between the nuclei and electrons. Thus an electronic oscillation occurs when the incident radiation possesses the necessary frequency, resulting in the enhancement of the near-field in the vicinity of the sphere, making LSPs ideal for sensing and optical devices.

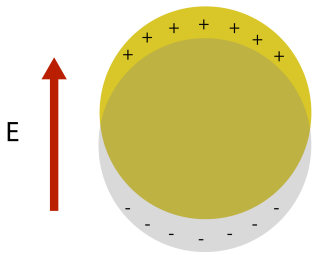

Figure 2.5 Au nanosphere under application of an external electric field, which acts to displace the free electron cloud.

LSPs are responsible for the optical properties of the Lycusus cup (Figure 1), as the small metal nanoparticles exhibit significant absorption in the green of region light[58]. As with SPPs, adjacent LSPs modes may couple, producing considerable electric field hot spots, for example in dimers and aggregated colloids. Moreover, optical excitation of LSPs may be achieved with the appropriate illumination frequency and polarisation, irrespective of the incident wavevector, as the sphere

breaks the translational invariance. This contrasts starkly with the wavevector matching requirement of planar SPP generation.

2.2 Optical Excitation of Surface Plasmon Polaritons

In order to couple light to SPPs, the inherent wavevector (momentum) discrepancy must be overcome, which is frequently achieved by availing of total internal reflection or scattering from nanoscale structures.

2.2.1 Prism Coupling

Prism coupling is one of the most prevalent methods for SPP excitation, as it may offer a coupling efficiency of close to 100% under resonant conditions. Light travelling in a dielectric medium has a naturally increased wavevector given by the product of the material's refractive index and the vacuum wavevector k_0. This results in an enlarged line cone that enables excitations of SPPs in a lower index material, as illustrated in Figure 2.6a. Under total internal reflection (TIR) conditions, an evanescent field is generated that may possess a wavevector matching k_{SPP}, and hence, for a given medium with an index n_d, the angle required to couple to SPPs is given by:

$$k_{SPP} = n_d k_0 \sin\theta \tag{2.25}$$

This may practically be achieved by coating a prism with a thin gold film, in the Kretschmann configuration, as illustrated in Figure 2.6b. Under these conditions the evanescent field penetrates the thin metallic layer and subsequently couples to SPPs at the air-metal interface. As light must tunnel through the metal, this technique is limited to suitably thin films. Alternatively, the Otto configuration may be employed, which requires a sufficiently small air gap between the prism and the metal, as displayed in Figure 2.6c. Consequently, the magnitude of coupling in both configurations is dependent upon degree of overlap of the radiation and SPP fields, and is thus sensitive to the gap between the TIR boundary and the SPP interface.

Prism coupling is naturally extremely sensitive to the local environment, making it an ideal technique for chemical and biological sensing applications, which exploit the large near-field intensities. Whilst this method yields a high efficiency of light-to-SPP coupling, the dielectric prisms that are required are bulky and thus would

compromise the compactness of a plasmonic source. Additionally, the requirement for a specific angle of incidence also adds complexity in terms of fabrication, and as a result the technique is unsuitable for on-chip SPP excitation.

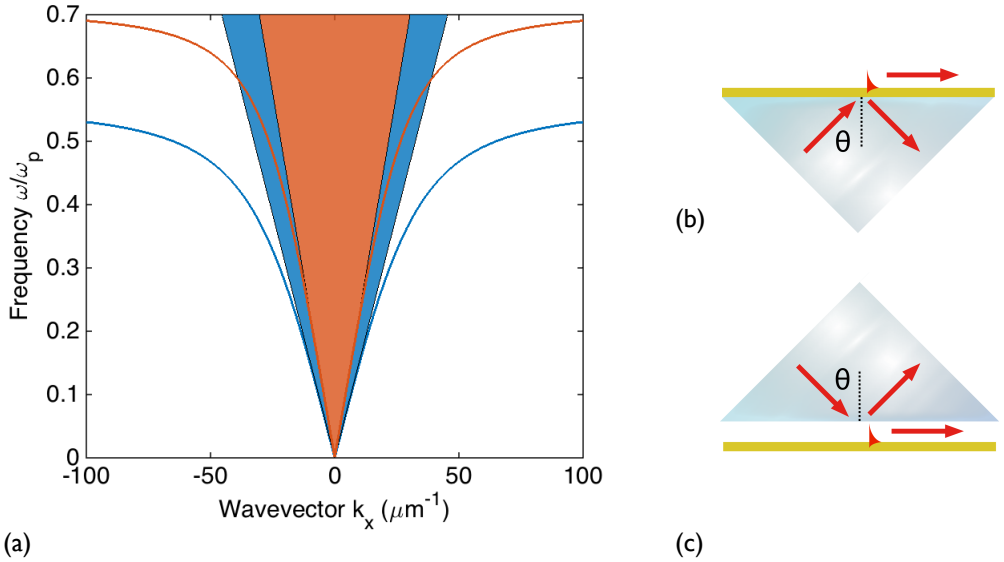

Figure 2.6 Prism coupling: (a) The light cone in air is shaded in red, with the blue region denoting the additional k_x values available in glass. The red line is the SPP dispersion at an air-Drude metal interface, with the blue line corresponding to SPPs at a glass-Drude metal interface. As a portion of the red curve lies within the blue region, air-metal interface SPPs may be excited via the dielectric. (b) Kretschmann configuration – tunnelling occurs through a thin metal film (c) Otto configuration – tunnelling occurs through an air gap. N.B. A prism geometry is often used so as to prevent additional, unwanted reflections. Alternatively, an immersion objective with a suitably high numerical aperture may be employed to excited SPPs using the same principle[44].

2.2.2 Diffraction coupling

A more compact, robust means of exciting SPPs involves matching the wavevector of light to SPPs via diffraction gratings and other small scattering structures. In the general case, light incident at an angle theta θ on a defect[59] will scatter accordingly, producing a continuum of k-vectors. This enables the launching of SPPs by fulfilling the phase matching condition:

$$k_{SPP} = k\sin\theta \pm \Delta k_x \tag{2.26}$$

where the first terms refers to the incident k_x value and the second term denotes additional k_x resulting from the scattering process. At normal incidence Equation 2.26 becomes $k_{SPP} = \pm\Delta k_x$, and consequently Δk_x must be greater than the dielectric

wavenumber (i.e. an evanescent wave). Rough metal films are example of a structure that may permit SPP excitation by via scattering. However, their ease of use is offset by their relatively low efficiency.

SPP excitation is more effectively achieved by employing a one dimensional diffraction grating embedded in a smooth film. This allows discrete momenta values to transferred to the incident photons via the periodicity of the system, and may thus generate SPPs on the smooth film. Considering a slit grating, as displayed in Figure 2.7a, light incident at an angle θ will subsequently scatter, increasing or decreasing the k_x component of the wavevector by integer multiples of the grating vector $G = 2\pi / d$, where d is the period. Consequently, the condition for grating coupling to SPPs on the adjacent smooth film is written as:

$$k_{SPP} = k_0 \sin\theta \pm mG \tag{2.27}$$

Where $m = 0,1,2,3...$

Moreover, the propagation of SPPs on a modulated surface, where the periodicity is similar to the SPP wavelength, may give rise to Bloch modes. The SPP dispersion thus is translated in reciprocal space to positions corresponding to multiples of the grating vector, with the resulting plasmonic modes fully characterised within the Brillioun zone ($-\pi / d$ to π / d), as displayed in Figure 2.7b. In this respect, diffraction gratings resemble crystal structures, and are therefore often referred to as surface plasmon polaritonic crystals (SPPCs), in a similar manner to photonic crystals[60]. A diffraction grating may hence be used to couple light to SPPs that now reside within the light cone, together with diffracting light to higher order Bloch modes.

It is also significant that, due to the periodicity, the SPP dispersion now intersects the $k_x = 0$ axis, permitting these modes to be excited with a beam at normal incidence, when $k_{SPP} = \pm mG$. Furthermore, the crossing of two SPP curves may open up a band gap due to coupling between counter propagating modes[61], which is not described by Equation 2.27.

Increasing the number of periods may allow a greater proportion of an incident beam to interact with the grating and hence couple to SPPs. However, this has the

added effect of increasing the out scattering losses of SPPs already propagating on the modulated surface, and consequently an optimal number of periods exists such as to maximise excitation of SPPs on an adjacent smooth film.

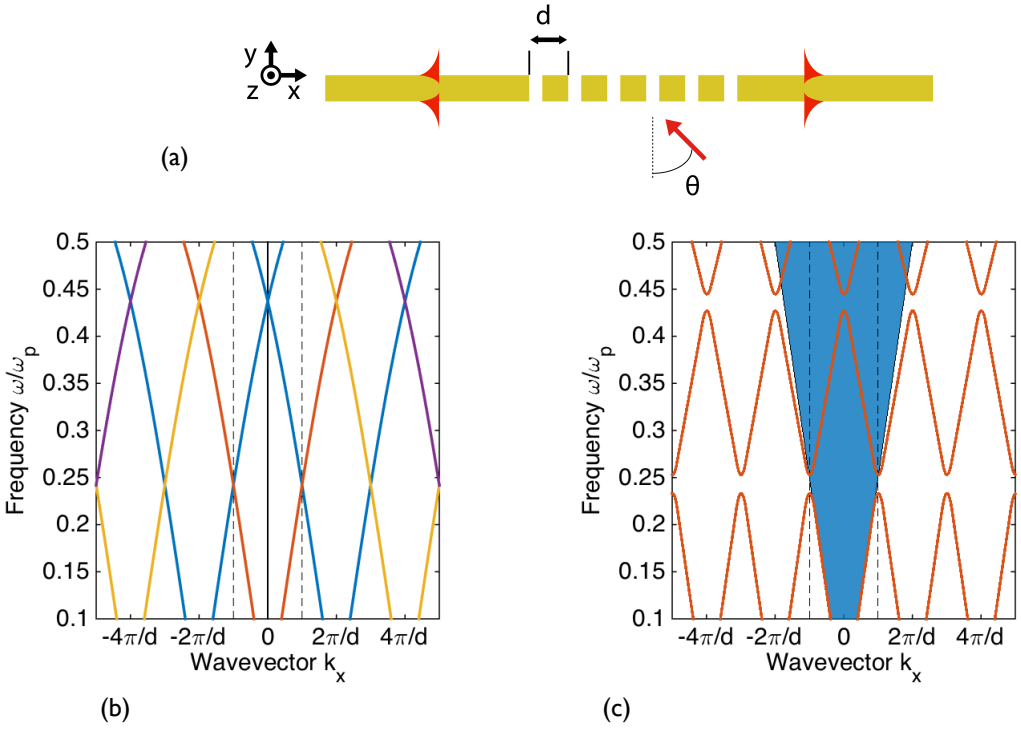

Figure 2.7 (a) A slit grating in an optically thick film under illumination in homogeneous dielectric environment, where d is the period. SPPs are excited from the grating and propagate on the adjacent smooth film (b) SPP dispersion due to an infinite, periodically modulated interface. The Brillioun zone is bounded by the dashed lines, within which the dispersion exhibits folding back. Red, blue, orange and purple lines correspond to $|m| = 0, 1, 2, 3$ diffraction orders respectively (c) Qualitative illustration (i.e. not calculated from Maxwell's equations) of the dispersion including the band gaps (red curves). The blue shaded region denotes the light cone in air.

Transmission gratings (SPP excitation on opposite side of the film with respect to the illumination), which are generally composed of an array of subwavelength apertures, are advantageous as they provide excitation of superstrate modes with minimal background radiation that would otherwise be present due to the illuminating beam. Correspondingly, a slit grating, such as that shown Figure 2.7a, permits SPPs excitation on both metal-dielectric interfaces. The band structures of these modes will thus depend on the superstate and substrate materials, in addition to the grating profile.

Besides optical coupling, SPPs can be electrically generated in metallic films upon impact with a charged particle, thereby generating an oscillating surface charge, as illustrated by the energy loss experiments discussed in Section 2.1. The original low-energy experiments measured electron diffraction and thus could only detect excitations with the asymptotic energy of $\hbar\omega_{SP}$. Nonetheless, subsequent experiments considered the transmission of electrons, and were therefore able to recover the full SPP dispersion[44]. More recently, Scanning Tunnelling Microscope (STM) arrangements have also demonstrated excitation of plasmonic modes[62].

Another route to generation of SPPs involves placing emitters or dipoles adjacent to a metal-dielectric interface, enabling coupling due to the large k-vectors present in the near-field[63]. Excited electronic or molecular states may hence non-radiatively decay into SPPs, offering the possibility of developing a localised plasmonic source[64].

In summary, over the course of this chapter we have briefly covered the basic elements of plasmonics, from the fundamental mode properties to their effective optical generation. Next we turn to VCSELs, which may form the basis for nanophotonic circuitry.

Chapter 3

Vertical-Cavity Surface-Emitting Lasers

The chapter discusses the general properties of Vertical-Cavity Surface-Emitting Lasers, with an emphasis on the advantages offered over edge-emitting laser diodes and other alternative optical sources. A more detailed discussion of the fundamentals of VCSELs, including topics covering threshold gain and current, differential quantum efficiency and power conversion efficiency, can be found in references 35-36.

3.1 Properties of VCSELs

The concept for a Vertical-Cavity Surface-Emitting Laser was first proposed in 1977 by Kenichi Iga whilst working at Bell Laboratories[35], with commercialisation following after almost 20 years of research and development[65]. The initial motivation was to develop semiconductor lasers with an emission wavelength longer than 1 μm, corresponding to the predicted low loss band for optical fibre transmission. However, VCSELs have since expanded into other areas of application, including computer mice, printing, data transmission, with further opportunities for industrial heating[66] and high density storage[36].

The structure of a VCSEL generally consists of two parallel reflectors that sandwich an active region that is electrically pumped, as outlined in Figure 3.1. The mirrors take the form of distributed Bragg reflectors (DBRs) that are composed of alternate layers of high and low refractive index materials with a thickness equal to one quarter of the material wavelength. Partial reflections at each interface interfere constructively, thus allowing the average reflectivity to exceed 99%, which is necessary to ensure a high Q-factor, $Q = \upsilon_0 / \Delta\upsilon$, where υ_0 and $\Delta\upsilon$ are the resonance frequency and full width half maximum of the resonance respectively. VCSELs often require Q-factors above 1000 in order for lasing to occur[36]. Consequently, light oscillates perpendicularly to the layers, as opposed to in a parallel fashion, as found in edge-emitters. Furthermore, the emission wavelength of VCSELs stems from the cavity resonance and not the gain peaks.

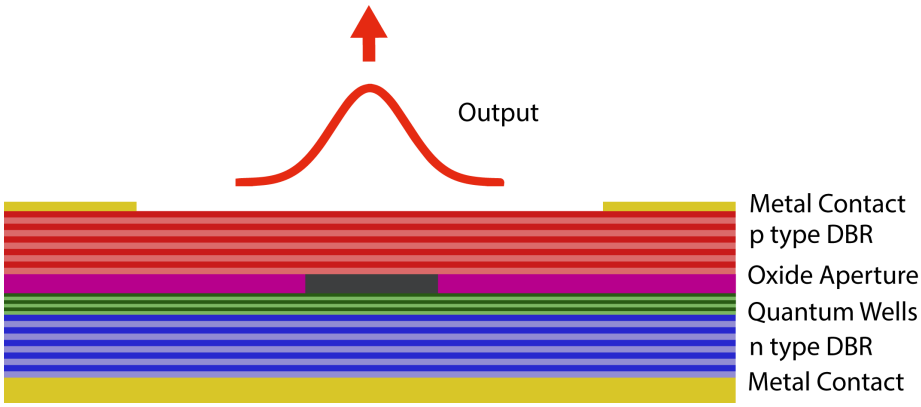

Figure 3.1 Cross section of VCSEL, showing the different compositional layers.

VCSELs are highly suited for use as an on-chip optical source, due to the number of advantages they confer over edge-emitters. These include:

- Compact dimensions
- Ultralow threshold operation due to the small cavity volume
- High-speed modulation with a low driving current
- Dynamic single longitudinal mode operation
- Low cost and small packing capability
- Monolithic fabrication
- Wide wavelength tuning and high circular beam quality

As semiconductor lasers, VCSELs rely on electron-hole recombination in the active region for photon emission. The structure is composed of a p-n junction, where the Bragg reflectors are usually p and n doped, and the active region between the mirrors contains quantum wells, providing the required gain. Often only one longitudinal mode is supported by the gain bandwidth, due to the small cavity length. Moreover, current confinement to active area is typically achieved by forming an insulating region that forces the current through a small aperture. This may be implemented by selective oxidation of DBR layers, which has the added benefit of providing index guiding.

Light travelling longitudinally is waveguided due to the oxide aperture, and various transverse modes may result. In this regard, we can consider the aperture in terms of a focusing lens, where the active area has a higher refractive index than the surrounding dielectric. Critically, single transverse mode operation may be

attained via employing a sufficiently small oxide aperture so that only the fundamental mode is supported, or such that higher order modes are overly lossy, and cannot attain threshold. Gain guiding, due to the presence of carriers in the active region, may also affect the mode profile. Single mode VCSELs are often employed for sensing applications, whilst multimode are typically used for data transmission. Moreover, VCSELs emitting at 850 nm are likely the most mature technologically, as 850 nm has many fibre-based standards for short haul datacom[36].

As the cavity resonance determines the emission wavelength, it is sensitive to thermal effects, including average variations in the layers' refractive index and expansion, which in turn allows the possibility of temperature control of the emission. In addition, Microelectromechanical (MEM) variation of the cavity length has also been demonstrated, whereby the top DBR is attached to a cantilever. Applying a voltage results in an electrostatic force that attracts the cantilever, shortening the cavity in the process and yielding wavelength tuning, which may exceed 100 nm[67]. It is also important to consider that the polarisation of VCSEL emission is inherently unstable, as there is not strong mechanism for selecting one specific orientation. This proves deleterious to many applications, nonetheless this issue may be overcome by the introduction of polarisation-dependent mirrors, such a grating structures etched into the top DBR[36]. Furthermore, replacing the mirror entirely with a subwavelength grating also allows for dispersion engineering of the cavity[68].

VCSELs represent an on-chip optical source that is electrically driven, and may be modulated, for instance, via directly controlling the current. The intrinsic speed is largely dictated by the photon density, differential gain of the active region and the cavity's photon lifetime. Modulation rates are steadily increasing as the technology matures - current commercial VCSELs are able to attain data rates of up to 25 Gbit/s, with rates as high as 55 Gbit/s also experimentally demonstrated[69]. As VCSELs offer fast modulation speeds with high reliability, they may be successfully employed in optical interconnections[38].

Surface plasmon resonances have also been implemented on VCSELs to provide an enhanced near-field[70,71]. This is particularly suited to the development of Heat Assisted Magnetic Recording (HAMR), which promises large data storage by reducing the size occupied by a single bit of information, and in the process

circumventing the superparamagnetic limit, where the magnetic state becomes thermally unstable. In theory, the significant near-field associated with a plasmonic resonance would provide sufficient local heating (above the Curie temperature) to ensure the coercively is lowered, hence allowing a realistic magnetic field to write data to a small area, and yielding a greater density of information stored on a hard disk[36].

3.2 Alternative On-Chip Sources

In addition to edge emitting lasers, it is pertinent to address other compact optical sources that may be considered as alternatives to VCSELs, including spasers[72], light emitting diodes (LEDs)[73], and surface plasmon emitting diodes (SPEDs). Spasers (Surface Plasmon Amplification by Stimulated Emission of Radiation) are the plasmonic counterpart of lasers, and have been dubbed the 'world's smallest laser'[29]. First proposed in 2003, spaser operation has since been experimentally demonstrated[74], however spasers (also referred to as nanolasers) have not reached the commercialisation stage. Interestingly, as Khurgin et. al discuss[75], both spasers and solid states lasers entail harnessing photons coupled to electronic oscillations – polaritons. In case of VCSELs, the oscillations originate from bound electrons, whereas spasers rely on free electrons. In the respect, the two are fundamentally similar, with the primary difference due to the proportion of energy stored in the electronic oscillations. In terms of performance, the out-coupling efficiency of VCSELs is currently superior to spasers, which are hindered by high power dissipation in the metal. Furthermore, the theoretical modulation speed of spasers at threshold operation is on the order of 100 gigahertz, which may also be realistically attained by VCSELs. Indeed, reducing the dimensions of VCSELs to the nanoscale via employing SPPs is also currently being researched[76]. Moreover, LEDs and SPEDs, by their nature, emit incoherent radiation, which places restrictions on their range of possible applications (e.g. interferometric).

To conclude, the discussed light emitting sources have different strengths and weakness, and thus lend themselves to diverse applications. VCSELs offer excellent optical performance, energy efficiency and compact dimensions, which, coupled with their already established nature, places them as the foremost candidate for an on-chip optical source.

Chapter 4

Experimental and Numerical Procedures

This chapter outlines the experimental and numerical methods employed in undertaking the challenge of designing and characterising VCSEL based plasmonic circuitry. Initially, sample fabrication is discussed, before turning our attention to experimental characterisation techniques and numerical modeling.

4.1 Sample Fabrication and Component Design

VCSEL development occurs on an industrial scale, and thus as the manufacturing processes are well documented, they lie outside of the scope of this thesis. Details on their growth and development can be found in references 35, 77 and 78. Here we will discuss the fabrication of nanostructures on metallic films for coupling free space radiation to SPPs, together with other optical components.

Gold was chosen as the SPP supporting material due to its beneficial optical and chemical properties. A good plasmonic material should possess a permittivity where the negative, real part is large and the imaginary component is small, corresponding to a small field penetration into the metal and low losses respectively. Thus, a quality factor Q_{SPP}, or figure of merit, generally takes into account both components of the permittivity. Following the analysis of West et al.[47] and Raether[43], we may define the factor to be the ratio of the real and imaginary part of the SPP wavevector, thus:

$$Q_{SPP} = \frac{k'_{SPP}}{k''_{SPP}} = \frac{\varepsilon'_m + \varepsilon_d}{\varepsilon'_m \varepsilon_d} \frac{\left(\varepsilon'_m\right)^2}{\varepsilon''_m} \tag{4.1}$$

If $\left|\varepsilon'_m\right| >> \varepsilon_d$ then Equation 4.1 becomes:

$$Q_{SPP} = \frac{\left(\varepsilon'_m\right)^2}{\varepsilon''_m} \tag{4.2}$$

From this equation it is apparent that the real component plays a greater role in determining the material's performance than the imaginary part. In this context, a high plasma frequency, or carrier concentration, is required to ensure a large, negative real component[42]. In addition to gold, both silver and aluminium fulfil this

requirement; nonetheless they rapidly degrade in quality. In contrast, gold is chemically stable and also offers low losses in the visible to near infrared region, making it one of the materials most suited for studies on plasmonics.

Thin gold films for plasmonic structures were fabricated primarily by thermal evaporation onto glass substrates. Gold exhibits a lattice mismatch with glass, requiring an adhesion layer to prevent delamination. Materials such chromium or tantalum pentoxide are frequently used to this effect. Once thin films have been fabricated, nanostructures may be etched into the surface by employing Focused-Ion-Beam (FIB) milling, a highly accurate technique that involves bombarding a sample with ions that displace material in a controlled fashion. A typical FIB involves accelerating Ga ions to 30 KeV via the potential established between the sample and the source, with focusing provided by electrostatic lenses. Upon impact with the surface, the ions sputter material, thereby permitting precise milling of various structures as the ion beam is raster scanned. Moreover, the ions may become implanted into the surface and generate secondary electrons, allowing the generation of images[79]. FIB systems may also incorporate Scanning Electron Microscopes (SEM) for imaging at high resolutions.

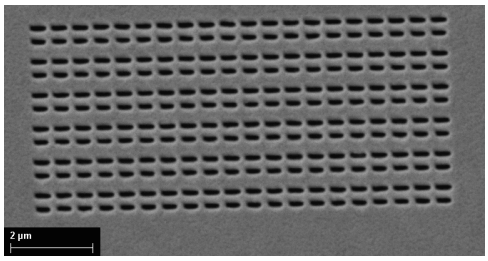

Figure 4.1 SEM image of an array of apertures patterned using FIB milling

The milled feature size and shape can be controlled by adjusting the beam current, together with the dwell time and number of scans. A Ga beam permits structures of down to approximately 10 nm to be patterned, depending on the sample parameters such as thickness and domain structure[80]. Redeposition of sputtered material is usually not significant for small structures, however, it is important to consider that the ion beam has a Gaussian profile. As a result, any rectangular structures, such as slit apertures, generally possess rounded edges, which will affect their scattering properties. Nonetheless, the versatility and

accuracy of FIB systems makes it a powerful tool for experimental fabrication.

In addition to creating plasmonic samples, we often require additionally non-standard optical components to enable their characterisation. 3D printing is an increasing prevalent technology that offers a significant degree of flexibility coupled with fast production speeds. The Solidworks software package enables the design of components that are converted to STL (STereoLithography) files, an industry standard for 3D printing.

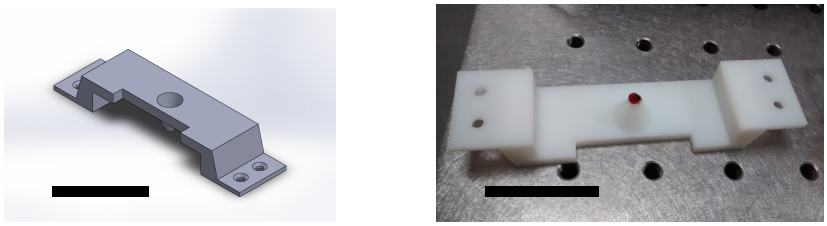

(a) (b)

Figure 4.2 (a) Example of a component designed in Solidworks (b) Photograph of the final printed model with a thin gold film glued underneath. Scale bars correspond to 4 mm.

Additionally, Solidworks may also be used to design mechanical parts, such as adapter plates, with the designs then converted into schematics for manufacture. Once nanostructures have been pattered in metallic films, and any other required components have been manufactured, we are subsequently able to characterise their optical response and image SPP using various optical techniques.

4.2 Imaging Surface Plasmon-Polaritons

Surface plasmon polaritons propagate at a dielectric-metal interface and accordingly cannot reach a detector located in the far-field. The presence of such modes can be inferred from a change in reflection or transmission, nonetheless imaging is possible if SPPs are out-coupled to light, in effectively the reverse process of optical excitation. Two of the most prominent techniques, namely Scanning Near-Field Optical Microscopy and Leakage Radiation Microscopy, offer contrasting means of mapping plasmonic modes, with differing advantages.

4.2.1 Scanning Near-Field Optical Microscopy

Conventional microscopy involves illuminating a sample with a monochromatic

wave and observing the scattered light via a collection lens placed in the far-field. Small object features correspond to large spatial frequencies, which produce large wavevector components in the light field that decay exponentially in the direction perpendicular to the surface, and thus cannot be collected by the lens. These non-propagating evanescent waves are thus confined to distances less than a single wavelength from the surface of the sample, within the near-field region. (In this regard, the near-field is generally characterised as the region in which evanescent fields cannot be neglected.) In contrast, the waves that possess small wavevectors, related to large object features, are able to propagate away from the object and towards the lens, and consequently a large observation distance effectively acts a low pass frequency filter. This leads to the diffraction limit, whereby the maximum spatial resolution is:

$$\Delta x = \kappa \frac{\lambda}{NA} \tag{4.3}$$

where Δx is the spatial resolution, $NA = n \sin \alpha$ is the numerical aperture (n is the refractive index of the surrounding medium, α is the acceptance angle), λ the illumination wavelength and κ is a factor that is dependent upon the intensity distribution of light incident upon the objective. In case of uniform illumination $\kappa = 0.61$ (the Rayleigh criterion)[7,81]. The diffraction limit thus is not fundamental to optical systems, but rather arises due to the assumption that collection occurs many wavelengths away from the sample[82].

The physicist E. H. Synge proposed a novel means of breaking the diffraction limit in paper published in 1928[83,84], which involved illuminating a sample via a subwavelength aperture in an opaque screen. The resulting light field behind the screen is confined to the size of the aperture, d, and hence will only interact with features that reside close to the aperture, i.e. within a distance d. Scanning the aperture across the sample thus produces a map of the scattered light with a resolution well below the illumination wavelength. Unfortunately, the technology available at time of publication was unable to realise Synge's microscope. In fact, it would be a further 56 years before the principle he described would be first experimentally validated with visible light, with a technique since known as Scanning Near-Field Optical Microscopy (SNOM or NSOM).

In 1984 Pohl et al. (IBM Zurich)[85] were the first to demonstrate SNOM in the visible regime, followed shortly by Lewis et al. (Cornell University)[86]. Pohl discussed SNOM in terms of an 'optical stethoscope', as the underlying principle is equivalent to that of the iconic medical tool. Moving a stethoscope across the chest enables the position of the heart to be determined roughly to within 10cm. If we assume a sound frequency of 30-100 Hz (wavelength of 100 m) the stethoscope provides a spatial resolution of approximately $\lambda/1000$. This is made possible by the use of a small aperture that is placed a small distance from the object (heart), as is the case with SNOM.

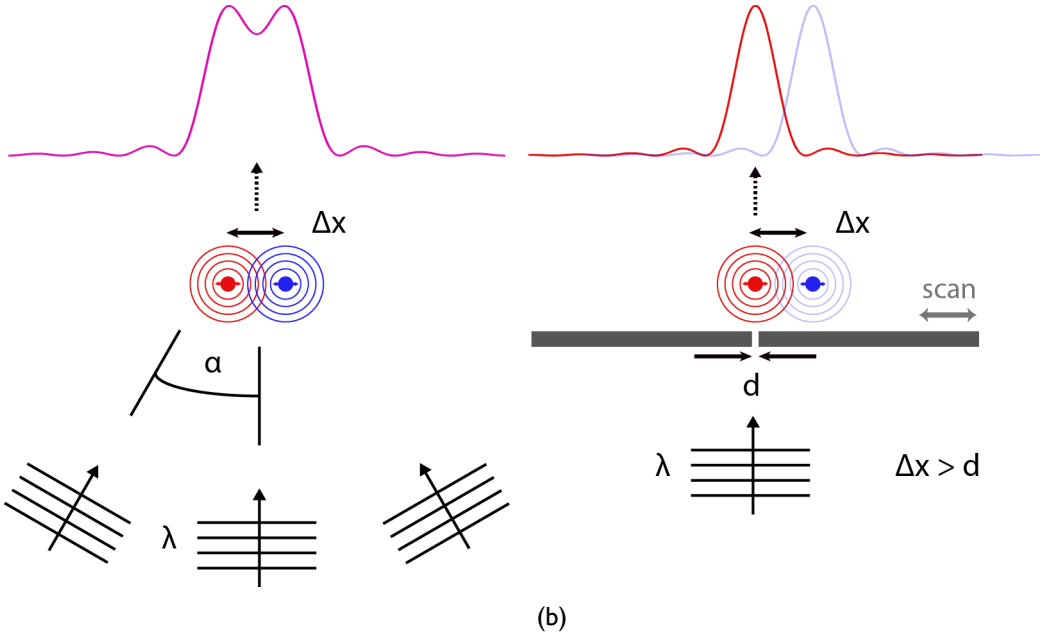

Figure 4.3 (a) Typical far-field collection of light originating from two scattering points. If Δx is smaller than Equation 4.3, then the two points cannot be resolved (b) Using a small aperture, an object may be illuminated locally such that the spatial resolution does not depend on the wavelength, but rather on a characteristic length, e.g. aperture size. (Figure adapted from Ref 81)

Furthermore, Pohl also suggests viewing SNOM in terms of Fourier space to gain an intuitive appreciation of the technique[7]. Light at the exit of a subwavelength aperture possess large lateral k-vectors, $k_{x,field} >> |k_0|$, i.e. evanescent fields. Small sample features in real space also correspond to large Fourier components (spatial frequencies, $k_{x,sample}$). The interaction between the large values of $k_{x,field}$ and $k_{x,sample}$ may produce k-vector combinations that lie within the light cone, allowing the waves to propagate to the detector, carrying information related the structure of

the sample. Essentially, all forms of SNOM entail locally scattering non-propagating (evanescent) near-fields into propagating far-fields. The resolving power of the aperture is comparable to its diameter, and derives from the relationship between its size and the relevant k-vectors involved.

SNOM has become a feasible tool for nano-optics due in part to the advancement of fabrication techniques and other scanning probe microscopy technologies, particularly Atomic Force Microscopy (AFM). An opaque screen with a hole, as envisioned by Synge, is impractical as samples are not usually flat, and thus the SNOM probe is often composed of a tapered optical fibre with a subwavelength aperture at the end. This allows the fibre aperture to be scanned across the surface by varying the height whilst maintaining a small separation with the surface. Furthermore, this implementation is advantageous for light delivery and collection, as the fibre is a waveguide. A number of modes of operation are possible for illumination and collection, as illustrated in Figure 4.4. Thus far we have considered the probe as the source of evanescent fields, but it may also act to scatter near-fields that are generated via far-field illumination , hence serving as the collection of the signal.

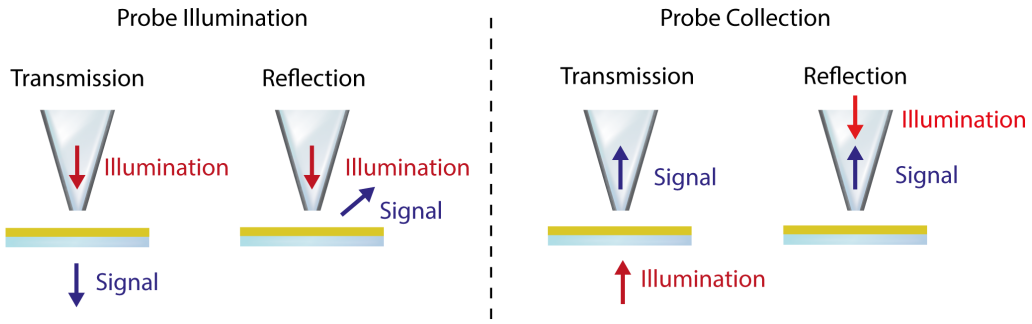

Figure 4.4 Example of different aperture SNOM modes of operation. Here transmission refers to the collection of signal on the opposite side of the sample, with respect to the illumination. Reflection denotes collection on the same side.

In order to maintain a sufficiently small separation between the aperture and sample, within 10s of nanometres (i.e. in the near-field region), some form is distance regulation is usually required. Typically feedback mechanisms resembling AFMs are employed, which also allows the topography to be mapped in tandem with the optical fields. For example, a mechanical sensor attached to the fibre is often utilised in a constant force setup. Piezoelectric quartz tuning forks, which

change dimension under application of an external electric field, offer high Q-factors, and thus are ideal as mechanical oscillators. Driving a tuning fork-fibre system at resonance and approaching the sample surface results in a modification of the resonance peak and Q-factor, due to the interaction with the surface. This may be monitored via a shear-force or tapping mode setup, which entails oscillation of the tip parallel or perpendicular to the surface respectively. Shear-force thus relies on the lateral forces produced during oscillation, whilst tapping mode utilises the atomic forces that occur due to the intermittent contacts with the surface.

SNOM is thus an invaluable tool in the investigation of plasmonic nanostructures and VCSELs as it provides simultaneous mapping of both the local electromagnetic field distributions and the topography, enabling correlation between the two. Considering that SPPs are confined to an interface, bringing a probe into the near-field results in the scattering of the plasmonic fields into modes that subsequently propagate in the fibre. As the probe acts to frustrate the evanescent fields to produce a far-field signal, there will be a degree of tip-sample interaction. Nonetheless, the images obtained should be largely representative of the field distributions in the absence of the probe. The excellent agreement of the experimentally obtained near-field images with numerical simulations confirms that this is often the case[87]. Additionally, SNOM probe may provide local excitation of SPP, due to the large wavevectors present near the probe apex upon illumination.

Figure 4.5a illustrates the setup employed to investigate plasmonic modes on VCSELs and smooth gold films. The probe is brought into the near-field such as to scatter SPPs, with resulting light collected by the fibre which is coupled to a photomultiplier (PM), thereby producing the detected signal. In order to create a tapered SNOM probe (Figure 4.5), a micropipette puller was employed to heat an optical fibre whilst applying a tensile force, which causes the fibre to break in a controlled manner. This method produces reproducible tips, for the pulling parameters may be tuned to alter the dimensions. Lastly, the probe tip is then bent 90 degrees by heating with a fibre splicer, to enable the use of tapping mode distance regulation.

The next step in probe fabrication involves thermal evaporation to coat the fibre in thin metallic film, commonly 100 nm of aluminium. This metal coating prevents the collected fields from leaking outside the probe during propagation. The fibre

probe acts as a waveguide, and thus as the tapered regions becomes smaller, all the modes experience cut-off, such that near the apex the propagation constants are imaginary and the field decays exponentially. In the cut-off region, some of the energy is dissipated in the metallic screen, producing heat. Consequently, there is a maximum power that can be transmitted though the probe before it is destroyed. In this context, aluminium is often used for coating fibres as it has a small skin depth in the visible region[7].

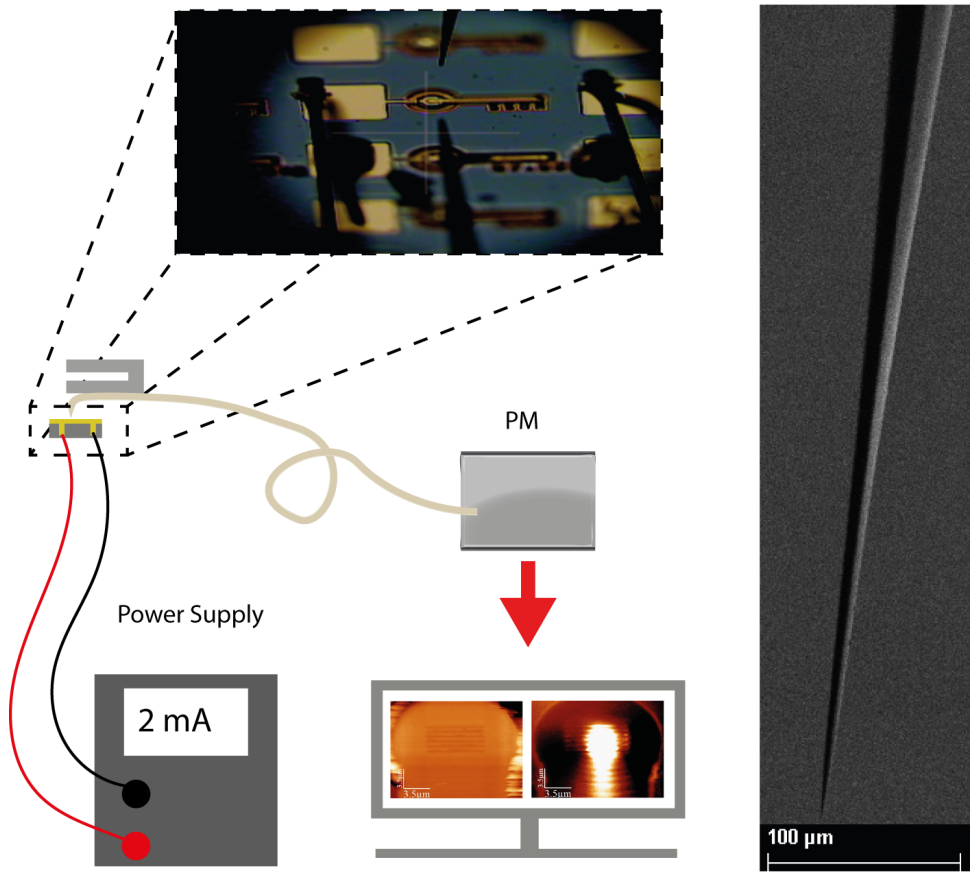

(a) (b)

Figure 4.5 (a) Schematic of a SNOM setup for characterising VCSELs. Applying a forward bias to a VCSEL and scanning the probe across the surface allows the near-field to be mapped in tandem with the topography. (b) SEM image of a typical SNOM probe tip.

Once a fibre has been coated with a metallic film, a FIB may be employed to produce an aperture cut to the desired diameter, and also to remove any protruding grains. If the SNOM aperture has a diameter that too small, it will result in a very poor signal to noise ratios. Additionally, increasing the diameter yields a larger signal but sacrifices spatial resolution. Hence there is a trade off between

resolution and signal, and consequently SNOM apertures typically have a diameter in the 80-150 nm range, offering a reasonable compromise.

Following the manufacture of a probe, it is then affixed to a tuning fork and mounted onto a piezo-stage, enabling x-y-z control. A frequency generator excites the system at its resonance frequency (~32.7 kHz), whilst the current is monitored. When the probe approaches the sample surface, its oscillations are damped due to the dispersive forces. The resulting feedback signal is thus maintained at a constant amplitude by the z-distance control, thereby producing a map of the sample topography as the probe is scanned.

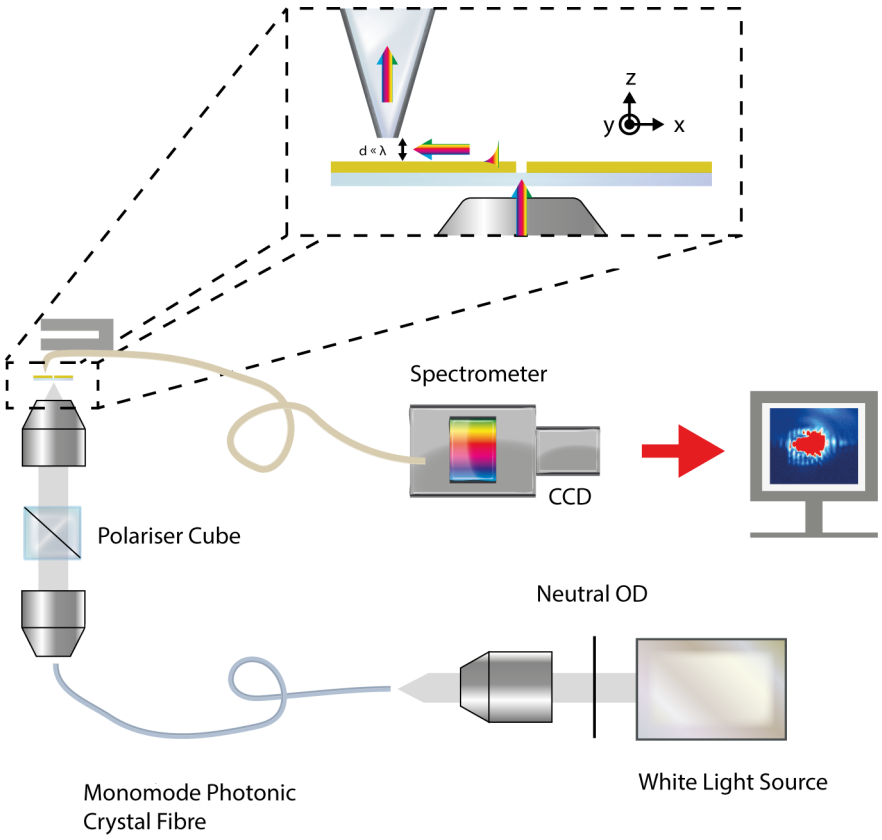

Figure 4.6 Schematic of the hyperspectral SNOM setup (figure adapted from 88). After passing through an optical density wheel, the broadband illumination is fed through a monomode photonic crystal fibre in order to obtain a Gaussian spot across the spectral range. The setup may be operated in probe collection or illumination mode, as described by Figure 4.4. The full spectral response is thus obtained at each probe position (pixel) during a single scan.

Many plasmonic nanostructures exhibit a wavelength dependent response, and thus illuminating with a broad spectral range allows a greater understanding of this

behaviour. This is especially pertinent to plasmonic grating and cavities, which exhibit well defined resonances[88]. Hyperspectral SNOM is advantageous in this regard, and may be implemented by illuminating a sample with coherent broadband light from a supercontinuum laser[88, 89], with detection via a spectrometer coupled with a high speed CCD, as outlined in Figure 4.6. The primary advantage of this setup is that the entire spectral response is captured in a single scan, negating problems such as image drift and tip deterioration between multiple scans.

Another category of SNOM involves discarding of the aperture entirely and using a pointed probe, or AFM tip, to locally scatter light. Apertureless SNOM (A-SNOM) probes can yield even greater near-fields for a given incident intensity compared to their apertured cousins[7]. Moreover, the enhanced field near the apex of A-probes may in principle achieve a resolution below 10 nm. The principal downside is the large background illumination, nonetheless this may be removed, for example via homodyne detection. Remarkably, A-SNOM was also essentially described by Synge in a letter to Einstein, in which he proposed using a colloidal particle to scatter near-fields[84].

The operating principle of SNOM may be understood in terms of converting evanescent fields into propagating waves, and there are several ways of understanding this process. Typically it is accepted that the near-field induces dipoles in the probe tip that subsequently radiate into the far-field. However, recent developments suggest this simple picture may not be sufficient, for additional multipoles, including magnetic dipoles, may be required to understand and model the near- to far-field conversion[87,90]. Continued developments in SNOM including interferometric techniques, whereby the signal is combined with a controlled reference, allowing phase and amplitude to be recovered. Phase sensitive implementations can thus be Fourier transformed, providing near-field images in k-space[91]. Moreover, simultaneous mapping of the electric and magnetic components has also been recently demonstrated[92].

SNOM is a powerful optical technique, however, as a form of surface probe microscopy it cannot characterise SPPs in conditions that prevent a probe from reaching the plasmonic field, such as inside a micron sized Fabry-Perot cavity. Nonetheless, another technique allows the SPP signal to be indirectly monitored for thin films based on radiation losses.

4.2.2 Leakage radiation Microscopy

Prism coupling of SPPs, as discussed in Section 2.2.1, involves increasing the wavevector of light via propagation in a dielectric with an index greater than air, such that $k_1 = n_1 k_0$, where n is the refractive index of the medium and k_0 the vacuum wavevector. Consequently, light incident at a specific angle will have a projection along the interface matching the SPP wavevector, permitting excitation by the resulting evanescent field.

Additionally, the reverse process is also possible, whereby SPPs tunnel through a thin metallic film and couple to light propagating in the dielectric, with the emission occurring at an angle given by Equation 2.25. In other words, SPPs effectively 'leak' into the substrate. These radiation losses may serve as a means of imaging SPPs, allowing the intensity of plasmonic modes to be indirectly monitored. The emission occurs at an angle greater than the glass-air critical angle, and so an oil immersion objective must be employed in order to prevent total internal reflection[93].

As SPPs couple to leakage radiation at a specific angle, LRM may be combined with Fourier imaging to obtain the plasmonic dispersion for modes propagating on a thin film. An example of a 4 lens Fourier arrangement is shown in Figure 4.7, which essentially yields the Fourier transform of the light field, allowing the SPP dispersion to be obtained. Real and k-space filtering may be implemented by placing filters in the corresponding planes, and also removing lens L3 allows real space to be imaged.

Advantages LRM holds over SNOM for imaging SPPs include its speed and ease of implementation. Whereas SNOM requires raster scanning a tip across the sample, LRM may quickly be set up, with the entire sample imaged at once. However, LRM is diffraction limited, and hence cannot rival the resolution of SNOM. Another disadvantage of LRM is its limitation to thin films, which does not apply to SNOM as it is a surface technique.

Other means of optically imaging SPPs include Fluoresce and dark-field mapping, and prominent electrical methods are electron energy loss spectroscopy and cathodoluminescence microscopy[94]. Hence, there are a plethora of methods for SPP imaging, which are being continually developed, each with its own advantages and limitations. Furthermore, combining SPP imaging with time-resolved setups allows the investigation of plasmonic dynamics.

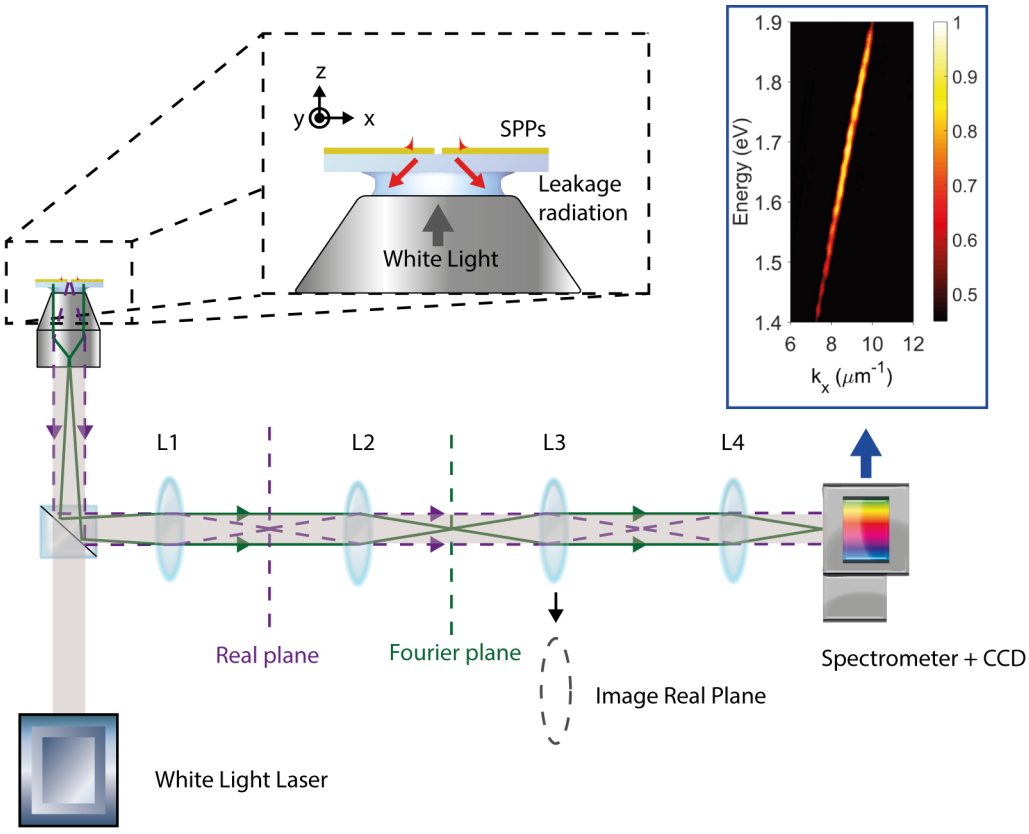

Figure 4.7 Schematic of the broadband Leakage radiation microscopy setup - a high N.A. objective collects the out-coupled light originating from SPPs with imaging in Fourier space. Also shown is the leakage radiation dispersion obtained by imaging the intensity in k-space, equivalent to the SPP dispersion of Figure 2.3.

4.3 Ultrafast Pump-Probe Spectroscopy

Many optical phenomena occur over a period of a few pico- or femtoseconds, a length of time that exceeds the speed of conventional electronic instrumentation. One approach to circumvent this technical challenge involves the use of ultrashort pulses with a duration comparable to, or less than, the timescale of the process being monitored. Ultrafast Pump-Probe Spectroscopy (UPPS) avails of femtoseond pulses to investigate optical systems, and may be thought of in terms of a stroboscopic camera. In this regard, the system takes a series of snapshots of the state of excitation, allowing the dynamics to be recovered. In this case of a pump-probe measurement, an initial pump pulse excites the system, with a second delayed probe pulse yielding information on the state of excitation.

As a simple example, we can consider an ensemble of two-level atoms. Upon illumination with a pump pulse, a number of atoms are raised to the higher energy

level, consequently decreasing the absorption of the probe pulse. In the time interval between the pump and probe pulses, a proportion of the atoms will return to ground state and thus the absorption will recover to an extent. Increasing the delay allows the absorption to return to its original value, with its rate providing information on the relaxation process of the atoms[95].

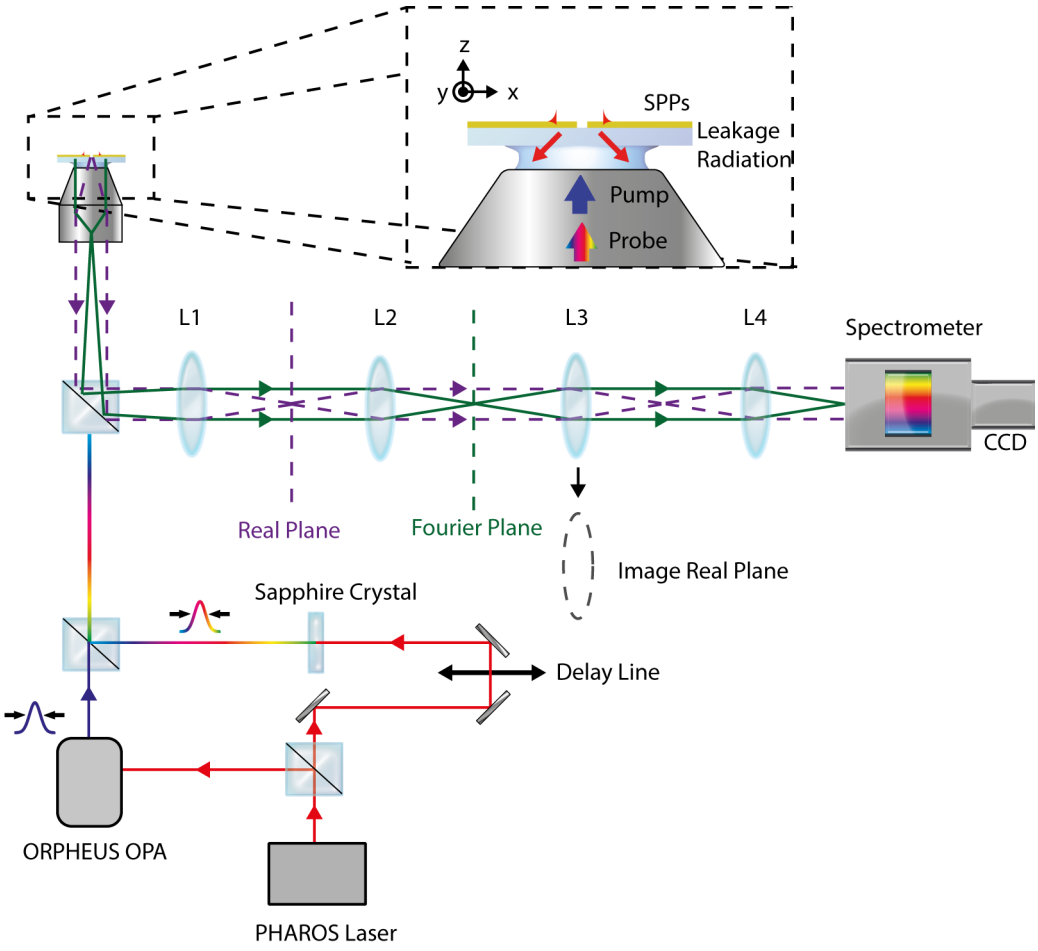

Figure 4.8 Schematic of the pump-probe setup with imaging of leakage radiation in Fourier space.

Focusing laser pulses may yield intensities sufficiently large so as to modify the optical properties of materials, and thus the large pulse energies and high temporal sensitivity available in UPPS make it an ideal technique for investigating nonlinear phenomena. The layout of the UPPS setup employed for charactering nonlinear dynamics is illustrated is in Figure 4.8.

In this instance, a UPPS setup has been combined with LRM, allowing the dynamics of SPPs to be recovered, but may also be implemented in conjunction with other techniques such as SNOM. The two beams originate from the same

source (PHAROS laser), with one path passed through a delay line and subsequently focused onto a sapphire crystal in order to produce a white light continuum that serves as the probe (signal) pulse. An ORPHEUS optical parametric amplifier (OPA) is pumped via the second path, thereby producing the pump pulse at the desired wavelength, with the two beams subsequently recombined and focused on a sample. A delay line controls the temporal delay between the pump and probe pulses, which may be scanned to recover the dynamics.

Once plasmonic structures have been experimentally characterised, they may also be numerically simulated, providing further insight into the optical response.

4.4 Numerical Modeling

Numerical modeling of the optical systems was carried out with COMSOL Multiphysics, which is finite element analysis software. The building blocks for this software are the laws of physics expressed in mathematical models, such as the laws of electromagnetism and mechanics. These mathematical models may consist of one or multiple partial differential equations (PDEs), together with boundary and initial conditions, with their solutions represented by dependent, unknown variables (field variables) such as electric and magnetic potentials described in space and time, which allow the system response to be predicted. However, such mathematical models are effectively continuous with infinite unknowns, and the analytical solutions may only be found in certain cases.

In light of this, the finite element method (FEM) may be employed to reduce the number of unknowns via dividing the simulation region into elements and expressing the unknown field variables in terms of approximating (i.e. interpolating) functions within these elements. These functions are defined in terms of the field variables at specific points called nodes, which then permit the field variables to be found at any point via interpolation. Hence, in the FEM, the unknowns are the field variables at the nodal points. After discretation of the model and selecting the interpolation functions, the element properties must be found and assembled to yield the global properties, in order to arrive at the system equations. Boundary conditions are also imposed, before the model is solved, producing the nodal unknowns. Additional calculation may also be required to obtain the desired values. The FEM thus makes a piecewise approximation, ensuring the continuity at nodal

points and element sides, where the values at points other than nodes are obtained by interpolation.

Upon solving the model, the difference between the solutions of the numerical and mathematical models is often termed the truncation error, which approaches zero as the element size is reduced towards zero, provided the numerical model is stable and consistent. Moreover, one of the major strengths of the numerical method is that it allows for the simulation of relatively complicated geometries with ease[96, 97].

Modeling of optical structures hence entails dividing the simulation area into various domains, typically consisting of air-metal-substrate, and subsequently defining their material properties and meshing the structure. Essentially COMSOL solves Maxwell's equations with the initial and boundary conditions, yielding an approximate solution of the optical response. A more detailed discussion on the specific method COMSOL employs can be found in the documentation, along with constructive example models[96]. Also, COMSOL has the ability to interface with MATLAB, providing a convenient method of controlling and automating simulations. One of the greatest strengths of the program is its ability to simulate various physical responses of systems (e.g. mechanical and electrical), including the optical properties of nanostructures via the Radio Frequency (RF) module.

4.4.1 Coupling and Propagation of Plasmonic Excitations

As discussed, creating an effectual COMSOL model of a plasmonic nanostructure involves defining domains with an appropriate mesh density, inputting the material properties and setting up a wave excitation boundary. Within the model, each component, or layer, is represented by a domain, with the material parameters input via the permittivity, permeability and conductivity quantities, which describe the optical response. For instance, a glass-gold bilayer would be modeled as two domains with refractive index of glass given by $n = \sqrt{\varepsilon_d} = 1.5$, and the complex, frequency dependent metal permittivity input via interpolating the experimental data of Johnson and Christy[46]. Furthermore, we can consider the permeability $\mu_r = 1$ for all the optical systems, thus reducing the number of input quantities. Upon running the simulation, a solution is obtained for each element and subsequently compared to the adjacent elements, ensuring that the result is

continuous and consistent with both the boundary conditions and material properties.

It is important to carefully consider the degree of discretisation, i.e. the size of the mesh elements. Every element has a number of degrees of freedom that are required to determine the physical response of the system. These degrees of freedom are related to the number of nodes, the points that determine the shape of the finite elements. Examples of mesh refinement techniques include global adaptive and wavelength adaptive, which serve to reduce the calculation time. Effective simulation of nanostructures typically involves utilising a triangular shaped mesh as it permits efficient fitting of diverse geometrical features such as curves and sharp corners. Additional sub-domains may also be defined to allow different mesh densities to be employed within a single material. For example, the element size in a dielectric superstrate may be decreased in areas far from scattering structures where the radiation closely resembles a plane wave. Nonetheless, the model should converge to the same solution, regardless of the mesh refinement technique[98].

Decreasing the element size may result in a lower error, however it concurrently increases the computation time. In light of this, an element size of $\lambda/10$ is a rough guide to obtain accurate solutions whilst maintaining a reasonable solving time, where λ is in wavelength of light being considered. The computer that was used in all the simulations presented here had the following specifications: Intel Core i7-2600 CPU @ 3.40GHz, 32GB RAM, Windows 7 64-bit. Simple 2D simulations, such as those presented in Chapters 5 and 6, typically take on the order of a few hours to calculate, whilst the nonlinear simulations in Chapter 7 require a few days of computation. Also, provided the structure is invariant in the third (out of plane) direction, we can model the system in two dimensions, considerably reducing the computation time.

As the models are finite in nature, care must be taken to minimise reflections from the exterior boundaries that would otherwise result in interference. Perfectly Matching Layers (PMLs) are one option to achieve this, which involves the gradual attenuation of propagating waves. When defining the PML regions, the thickness and mesh density should be appropriately chosen to ensure minimal reflection. Furthermore, an excitation port is often placed behind a PML domain, such that the beam must first pass through this layer before arriving at the structure, to prevent

multiple reflections from the structure and the external boundary. For simulations in linear optical regime we set the incident power to unity, and thus as the PML's attenuation is frequency dependent, the power emitted must be normalised across the spectrum.

To investigate the coupling of VCSELs to SPPs on metal films we initially set up a two dimensional finite area bounded by PMLs. A Gaussian beam, which approximates to the VCSEL emission at threshold currents, is subsequently used to illuminate the structure from beneath at normal incidence. The electric field profile at the x-axis excitation port then is defined as:

$$f(x) = A\exp-\left[(x-x_0)^2/2\sigma^2\right] \tag{4.4}$$

where A is the peak amplitude, x_0 the beam centre, and the full width half maximum is given by $FWHM = 2\sigma\sqrt{2\ln 2}$. When comparing simulations with experimental beams, we must consider the FWHM is typically defined in terms of the intensity and not the electric field. In the case of monochromatic, Gaussian beams, the two quantities are related via $I = |E|^2 c\varepsilon_0 n/2$, where c is the vacuum speed of light, n the refractive index and ε_0 is the vacuum permittivity. Whilst the full VCSEL operation may be simulated in COMSOL, for the purposes of plasmonic excitation, it is satisfactory to only consider the Gaussian output beam.

Figure 4.9a displays the general model setup, together with an example simulation of the power emitted by a subwavelength slit. An estimate for the power coupled to SPPs is given by integrating the time-averaged Poynting vector $\langle \mathbf{S} \rangle = 0.5 \bullet \mathrm{Re}\left(\mathbf{E} \times \mathbf{H}^*\right)$, where $\mathbf{E}$ and $\mathbf{H}^*$ are the electric field and complex conjugate magnetic field vectors respectively. Also, the exponential power decay of SPPs can be accounted for via Equation 2.22. Running the simulation in the frequency domain thus characterises the optical properties at the set incident wavelength. In addition, a parametric sweep can be used to obtain the spectral response, and also to investigate effect of the varying geometrical or other optical parameters.

The SPP dispersion is particularly useful for elucidating the plasmonic intensity and any coupling experienced by these modes. This may be obtained optically, i.e. by varying the angle of incidence, thus changing the incident wavevector. In conjunction with the necessary wavelength sweep, this calculation may require

significant computation time. However, the dispersion can be retrieved via Fourier analysis, which is not constrained by a maximum possible lateral k-vector. Sampling a component of the magnetic or electric field at regular intervals along the metal film and performing a Fast Fourier Transform (FFT) yields the spatial frequency in that direction, and thus allows the dispersion to determined from only a wavelength sweep, which is illustrated by Figure 4.9b. The evaluation points must be sufficiently close to the film so as to probe the SPP field, i.e. within the decay length in the medium. From the sampling theorem[99], the employed sampling frequency should be at least twice the maximum spatial frequency to be resolved, otherwise aliasing could occur. Since we are performing a discrete Fourier transform on a finite number of samples, there will be a degree of broadening (uncertainty) in k-space. However, this is typically not significant, provided the sampling range is sufficiently large. Once an FTT has been performed on the plasmonic field, the data is then FFT-shifted and padded with zeros, which allows for further interpolation in k-space. A sampling window may also be applied to reduce effect of spectral leakage[100].

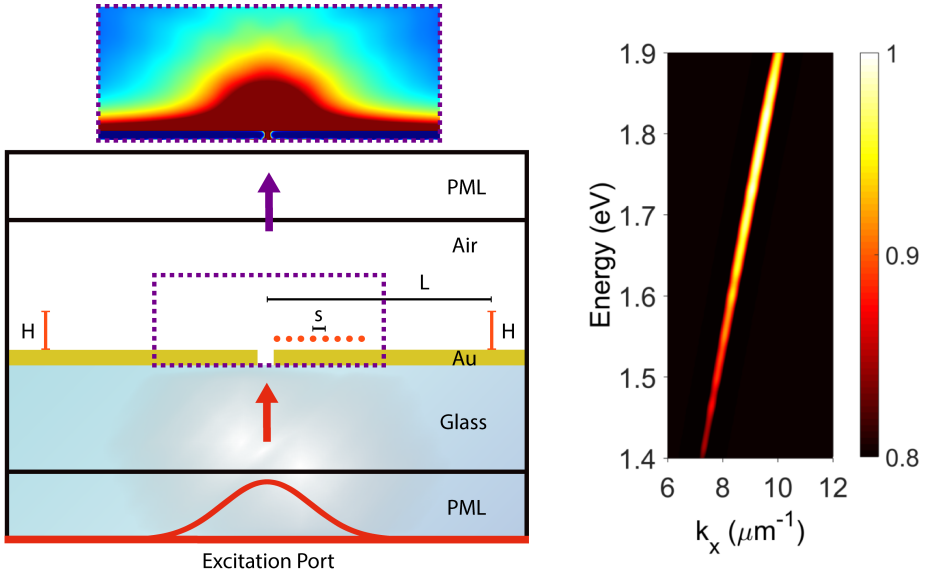

(a) (b)

Figure 4.9 (a) Typical COMSOL 2D simulation setup for investigating the optical response of plasmonic structures. Here *s* refers to the distance between adjacent evaluation points, for Fourier analysis of the light field. *H* is the height of the line for integrating SPP power flow, and *L* is the effective distance from the SPP source (slit edge), which enables the exponential power decay to be considered. Insert shows the time averaged power flow upon illumination of a subwavelength slit with a Gaussian beam. (b) SPP dispersion obtained via Fourier analysis of the magnetic field above the metal film, equivalent to dispersions of Figures 4.7 and 2.3.

It is pertinent to note that the imaginary part of the k-vector obtained in this analysis does not relate to the propagation length, but rather the to phase. An example of the SPP dispersion obtained via Fourier analysis is plotted in Figure 4.9b, which agrees with Equation 2.15, confirming its validity.

Additionally COMSOL has a module that permits the use of Monte Carlo methods for system optimisation, which entails repeated random sampling to obtain approximate solutions, and thus choosing the appropriate initial conditions and boundaries is critical to obtaining an optimal design. This technique may be employed, for instance, to optimise the scattering into plasmonic modes from various nanostructures.

Generally a Monte Carlo method involves defining the statistical properties of possible inputs, generating inputs that follow these properties, performing a deterministic computation on the inputs, and then analysing the results. To gain an appreciation of this method, we may consider the following simple case for approximating π: Suppose we define a square, with a side length equal to 2, which contains a circle, with a radius equal to 1, as shown in Figure 4.10. The areas of square and circle are thus $A_s = (side\ length)^2 = 4$ and $A_c = \pi(radius)^2 = \pi$ respectively. Dividing these areas gives $A_c / A_s = \pi / 4$, and hence we may calculate π from this equation. Monte Carlo simulation can then be used to approximate the ratio by sampling points within the square in a random fashion. As the origin is placed in the centre, the limits are: $-1 \le x \le 1$ and $-1 \le y \le 1$, i.e. a sampled point must lie within the square. In addition, if a sampled point has coordinates where $x^2 + y^2 \le 1$, then it also lies within the circle[101].

It follows that $A_c / A_s \approx (\text{No. of points in circle}) / (\text{No. of points in square})$, where the number points in the square equates to the total number of points. In other words, the percentage of points in the circle will be proportional to the area of circle as a percentage of the square (i.e. total) area. If, for example, we consider a sample size of $n = 1000$, where 790 points lay within the circle, then we obtain $\pi \approx 4 * (790/1000) = 3.16$. This helps to illustrate the importance of a large sample size, as this method will be ineffective if n is very small. Also, the sampled points should be uniformly distributed to ensure high accuracy. In the COMSOL implementation, the Monte Carlo optimisation module explores the full search space, and thus does not become stuck in local peaks [96,102].

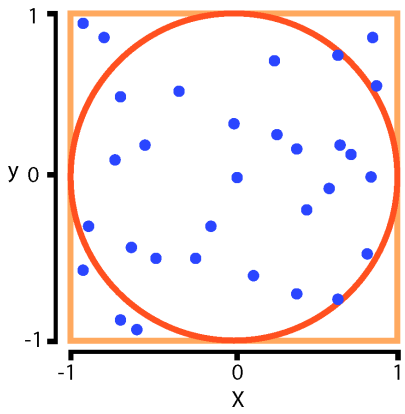

Figure 4.10 Monte Carlo approximation of pi: a red circle within an orange square, where the blue dots are the randomly sampled points. By taking the ratio of the number of points within the circle compared to the total number, pi may be approximated.

In the case of optimising scattering of light into SPPs, each geometric dimension of the scattering element that is under illumination is assigned a parameter (e.g. the width of slit). These parameters are then randomly varied within defined limits to in order maximise a predefined expression that describes SPP coupling (in the particular case, we maximise Equation 6.3). Thus the optimisation module requires setting the initial parameters, parameter limits and the number of iterations, in addition to the expression to evaluate. Furthermore, it is important to set reasonable limits such that the optimised geometry is practical to manufacture.

In addition to modeling plasmonic excitations, we may also simulate the nonlinear dynamics of nanostructured systems, with the aim of investigating active functionalities. Specifically, we aim to model the permittivity change in gold films upon excitation with ultrashort pulses, as per the experimental pump-probe setup outlined in Section 4.3. Thus we must consider the nonlinear response of gold, which relates to the nonlinear dependence of the polarisation in response an applied electric field[103].

4.4.2 Intensity Dependent Permittivity of Gold

Nonlinear phenomena occur in materials due to change in the optical properties, stemming from the presence of light. They are nonlinear as the response depends nonlinearly upon the strength of the applied field. To clearly

illustrate this, we may express the dependence of the polarisation P on the optical electric field E as power series, giving:

$$P(t) = \varepsilon_0\left(\chi^{(1)}E(t) + \chi^{(2)}E(t)^2 + \chi^{(3)}E(t)^3 + ...\right) \equiv P^{(1)}(t) + P^{(2)}(t) + P^{(3)}(t) + ... \quad (4.5)$$

Where $\chi^{(s)}$ is the sth order susceptibility of the material, ε_0 the vacuum permittivity and the time harmonic electric field $E(t)$. The first term in Equation 4.3 is dominant for low to moderate intensities, with the polarisation oscillating at the corresponding frequency. This linear response relates to conventional optical phenomena, such as refraction. However, at high intensities, the second and third order terms can no longer be neglected[103]. In the classical Lorentz model, we may consider an atom as a harmonic oscillator, which helps to describe the linear optical properties, wherein an electron is attached to a spring that restores its position following displacement via the Lorentz force of the electric field of light. This model may be then extended to include nonlinearity as a departure of the restoring force from Hooke's law[104]. For instance, the second term may give rise to phenomena such as Second Harmonic Generation (SHG)[22]. The third order response is given by $P^{(3)}(t) = \varepsilon_o\chi^{(3)}E(t)^3$, and if we assume an incident monochromatic field where $E = \beta\cos\omega t$, then the nonlinear polarisation may be written as:

$$P^{(3)}(t) = \frac{1}{4}\varepsilon_0\chi^{(3)}\beta^3\cos 3\omega t + \frac{3}{4}\varepsilon_0\chi^{(3)}\beta^3\cos\omega t \quad (4.6)$$

The first term in Equation 4.6 relates to third harmonic generation, as there is a response at frequency 3ω due to an applied field with a frequency ω. The second term describes a nonlinear contribution to the polarisation at the incident frequency ω, which leads to a nonlinear contribution to the refractive index experienced by the wave. Thus refractive index becomes intensity dependent, and may be expressed as:

$$n = n_0 + n_2 I \quad (4.7)$$

where ε is the permittivity, n_0 and n_2 are the linear and nonlinear refractive indices respectively, with I denoting the light intensity. This intensity dependent change in the refractive index is often referred to as the optical Kerr effect (N.B. In the frequency domain, we may write polarisation that influences propagation of a beam of frequency ω as: $P(\omega) = \varepsilon_0\chi^{(1)}E(\omega) + 3\varepsilon_0\chi^{(3)}(\omega)\left|E(\omega)^2\right|E(\omega)$ and thus we may also write

the index as $n^2 = 1 + \chi^{(1)} + 3\chi^{(3)}|E(\omega)|^2$). Self-focusing, which entails a beam modifying the index of the material through which it propagates, is an example of this phenomenon. In general, this nonlinear effect only becomes apparent at high intensities for most materials.

Modeling the Kerr response of gold under optical excitation can be done successfully within the Random Phase Approximation (RPA)[105]. Illumination of a metal such as gold may excite two different types of electronic transition, namely interband and intraband, which are dependent upon the photon energy, $E = \hbar\omega$. Intraband transitions occur within the conduction band, whilst interband excitations take place between the conduction and valence bands. Following optical excitation, the transient behaviour of gold is determined by the subsequent electronic relaxation processes. The three primary relaxation pathways exist: electron-electron, electron-phonon and phonon-phonon scattering. Generally, the electron-electron relaxation time τ_{e-e} is a few tens of femtoseconds and the electron-phonon relaxation time τ_{e-p} is on the order of picoseconds. Phonon-phonon scattering establishes thermal equilibrium within the material, and the relaxation time τ_{p-p} is typically on the order of hundreds of picoseconds. Redistribution of the electron density in momentum space thus accounts for the modification of the permittivity upon excitation, which may be modeled via the time-dependent electron temperature[106-108].

In this context, the temperature dependent permittivity of gold may be expressed as the sum of the interband and intraband contributions:

$$\varepsilon(\omega) = \varepsilon_{\text{inter}}(\omega) + \varepsilon_{\text{intra}}(\omega) \tag{4.8}$$

Considering gold, the $\varepsilon_{\text{intra}}$ term relates to free electron motion within the sp band and $\varepsilon_{\text{inter}}$ denotes the interband transitions between the d and sp bands. Moreover, the intraband contribution may be expressed by a Drude-like response:

$$\varepsilon_{\text{intra}} = \varepsilon_{\infty} - \frac{\omega_p^2}{\omega\left(\omega + ih\gamma_{\text{intra}}(\omega)\right)} \tag{4.9}$$

Where ε_{∞} is the high frequency permittivity limit, ω_p the plasma frequency, and $\gamma_{\text{intra}}(\omega)$ characterises the damping process of free-electrons.

Additionally, the interband term may be described within the RPA[105] as:

$$\varepsilon_{\text{inter}} = K\int_0^{\infty} \frac{\sqrt{\hbar x - E_g}}{x}\left[1 - f\left(x,T_e\right)\right]\frac{\left(\omega^2 - x^2 - \gamma_{\text{inter}}^2 - 2i\omega\gamma_{\text{inter}}\right)}{\left(\omega^2 - x^2 - \gamma_{\text{inter}}^2\right)^2 + 4\omega^2\gamma_{\text{inter}}^2}\,dx \tag{4.10}$$

Where K a wavevector independent constant related to the magnitude of the dipole transition moment for the interband transition. E_g is the transition energy between the d and sp bands and γ_{inter} is the interband scattering rate for electrons excited via interband transitions. $f\left(x,T_e\right)$ is the Fermi-Dirac distribution for the electrons at an equilibrium temperature T_e. Electrons are fermions, possessing half-integer spins and obeying the Pauli exclusion principle, with the Fermi-Dirac distribution given by $f\left(x,T_e\right) = 1/\left(\exp\left[\left(\hbar x - E_F\right)/\left(k_B T_e\right)\right] + 1\right)$, where E_F is the Fermi energy. RPA acquired its name from the assumption that, under certain circumstances, a sum of exponential terms with randomly varying phases may be neglected – mutual compensation takes place[109]. RPA is essentially a method to describe the collective response of the electron gas in which electrons are considered as independent excitations. Moreover, the modeling also assumes a Drude-Lorentz behaviour in which the interband transitions are occurring between a flat d band and a parabolic conduction band with the electronic energy distribution following an equilibrium Fermi-Dirac probability distribution.

It is also important to consider that Equation 4.8 may also be corrected to account for a change of the mean-free path of electrons in the material, due to fabrication process. The modification may be introduced via:

$$\varepsilon_{corrected} = \varepsilon_{metal} + \varepsilon_{correction} \tag{4.11}$$

Where:

$$\varepsilon_{correction} = \frac{i\omega_p^2 \dfrac{\left(L - R\right)}{\gamma_{\text{intra}}}}{\omega\left(\dfrac{\omega}{\gamma_{\text{intra}}} + i\right)\left(\dfrac{\omega}{\gamma_{\text{intra}}}R + iL\right)} \tag{4.12}$$

Here R is the effective mean free path and L is the bulk mean free path. This correction is particularly relevant for plasmonic structures such as nanorod arrays[106].

Once a gold film is optically excited, the electrons respond almost instantaneously, and the energy subsequently decays via collisions amongst the

electrons and lattice phonons. These particles possess temperatures T_e and T_L respectively, which are proportional to the particles' velocities. Consequently, the temperatures are dependent on the particles' momenta, which are influenced by the energy decay collisions. The two temperature model[105] may be used to relate T_e and T_L:

$$C_e T_e \frac{\partial T_e}{\partial t} = \nabla \cdot \left(K_e \nabla T_e\right) - g\left(T_e - T_L\right) + \omega_0 \,\mathrm{Im}(\varepsilon)\left\langle \mathbf{E}(r,t) \cdot \mathbf{E}(r,t) \right\rangle$$

$$C_L \frac{\partial T_L}{\partial t} = g\left(T_e - T_L\right) \tag{4.13}$$

Where $C_e = 67.96 J/m^3 K^2$, the heat captacity of electrons, $g = 2 \times 10^{16} W/m^3 K$, which is a constant related to the coupling between electrons and phonons. Additionally, $\left\langle \mathbf{E}(r,t) \cdot \mathbf{E}(r,t) \right\rangle$ is the time averaged electric field, K_e is the electron heat diffusion constant and C_L is the lattice heat capacity. Thus the three terms in the first equation refer to the electron heat diffusion, electron-phonon coupling and input optical power. In this regard, an imbalance between T_e and T_p occurs once the gold has been pumped, resulting in a change in the permittivity.

Modeling of the nonlinear response of metallic films was achieved by employing COMSOL to solve the two temperature model, together with Maxwell's equations. Intially, the gold nanostructures are illuminated by a pump beam with a Gaussian mode profile (Equation 4.2) and a Gaussian temporal profile, given by $I(t) = I_0 \exp\left(-t^2 / 2t_d^2\right)$ where t_d is the FWHM pulse duration and I_0 the peak intensity. Maxwell's equation's are thus solved in the frequency domain, and the power dissipation density $q(\boldsymbol{r}, \omega, t_0)$ is retreived for time t_0. This density is then input into the two temperature model, which is subsequently solved for a time step of $\Delta t = 30$ fs, during which $q(\boldsymbol{r}, \omega, t_0)$ is assumed to be constant. In this regard, the two temperature model (Equation 4.13) may be rewritten as:

$$C_e T_e \frac{\partial T_e(r,t)}{\partial t} = \nabla \cdot \left(K_e \nabla T_e(r,t)\right) - g\left(T_e(r,t) - T_L\right) + q(\boldsymbol{r}, \omega, t_0) \tag{4.14}$$

Also, as phonons possess a relatively large heat capacity and we are neglecting their dynamics here. Consequently we retrieve the electron temperature distribution $T_e(\boldsymbol{r}, t_0 + \Delta t)$ and the gold permittivity is correspondingly recalculated. However, the

permittivity will now be position sensitive, for it is dependent on the electron temperature which possesses a non-homogeneous distribution as a result of pumping. Therefore we obtain the permittivity $\varepsilon\left(\omega,T_e\left(\boldsymbol{r},t_0+\Delta t\right)\right)$ that is then input into the frequency domain model, allowing a wavelength sweep of the structure, representing a white light probe pulse. Once the spectral response has been obtained the permittivity is subsequently used in the calculation of the power dissipation density for the next time step $q\left(\boldsymbol{r},\omega,t_0+\Delta t\right)$. This process is the repeated until the pulse intensity has approximately reached zero[108].

It is important to note that the dynamics of phonons may be accounted for by solving the coupled equations, where phonons are associated with a finite heat capacity. In the two-temperature model, the equilibrium temperature of the electron-phonon system would then be increased by the amount of energy first deposited in the electronic system by the optical pump, which would affect the relaxation time. Moreover, the dissipation of heat to the environment is important to consider for certain cases. This is especially pertinent to metal nanoparticles that are used as nano heat sources, in applications such as cancer treatment or water heating. Consequently, if we assume a spherical gold nanoparticle is heated with an ultrashort pulse, Equation 4.13 may be modified to include a heat sink, yielding:

$$C_L \frac{\partial T_L}{\partial t} = g\left(T_e - T_L\right) - \frac{H(t)}{V} \tag{4.15}$$

where $H(t)$ is the instanteous heat realeased through the gold-environment interface and V is the nanoparticle's volume[110], with the negative sign indicating the cooling effect. The time evolution of $H(t)$ then depends on the ability of the surrounding medium to evacuate heat, thereby cooling down the particle. For small length scales and times, $H(t)$ may be generally described by a Boltzmann transport equation, with an overview available references 110 and 111.

Considering all the methods discussed in this chapter, we are well equipped to manufacture, characterise and model plasmonic structures for integration on VCSELs.

Chapter 5

Plasmonic components based on VCSELs

The chapter details the development of plasmonic components based on Vertical-Cavity Surface-Emitting Lasers, together with demonstrating on-chip plasmonic signal generation, frequency conversion and detection.

5.1 Development of VCSELs for Plasmonic Applications

In collaboration with the Tyndall National Institute in Cork, Ireland, we have developed a VCSEL that is based on an 850 nm wavelength diode integrated with plasmonic waveguiding structures, as outlined by Figure 5.1[112,113]. A thick gold film covers the diode's emission area, into which nanoapertures may be etched. Infrared light emitted by the laser consequently scatters from these structures, in the process exciting SPPs that may couple to the adjacent waveguide. The laser diode itself contained p- and n-doped distributed Bragg reflectors (DBRs) that were composed of 35.5 and 22 pairs of graded index $Al_{0.12}Ga_{0.88}As$–$Al_{0.9}Ga_{0.1}As$ respectively. An $Al_{0.98}Ga_{0.02}As$ layer was set in place of an $Al_{0.9}Ga_{0.1}As$ layer in the upper half of the structure, next to the p-type reflectors, for selective oxidation to form an aperture. Sandwiched between the DBRs was the active region, made up of three 6 nm think GaAs quantum wells. Mesas 46 μm in diameter, together with an extended platform that formed the base of the plasmonic waveguide, were lithographically patterned and dry etched. Selective oxidation resulted in 4 μm apertures, thereby determining the area that contributes to light generation, with the platform entirely oxidised such as to prevent any current flow in this region. Once the SiO_2 layer was opened, the p- and n-type metal contacts (Ti-Pt-Au and Au-Ge-Ni respectively) were deposited. A lift-off process was then employed to form the Au-Cr-SiO_2 trilayer. Chromium acted as an adhesion layer and additionally inhibits any substrate SPP propagation that would otherwise occur at an Au-SiO_2 interface. Moreover, the thickness of the SiO_2 layer was approximately equal to half of the wavelength in the material, ensuring that an electric field antinode occurred at the boundary with the Cr film.

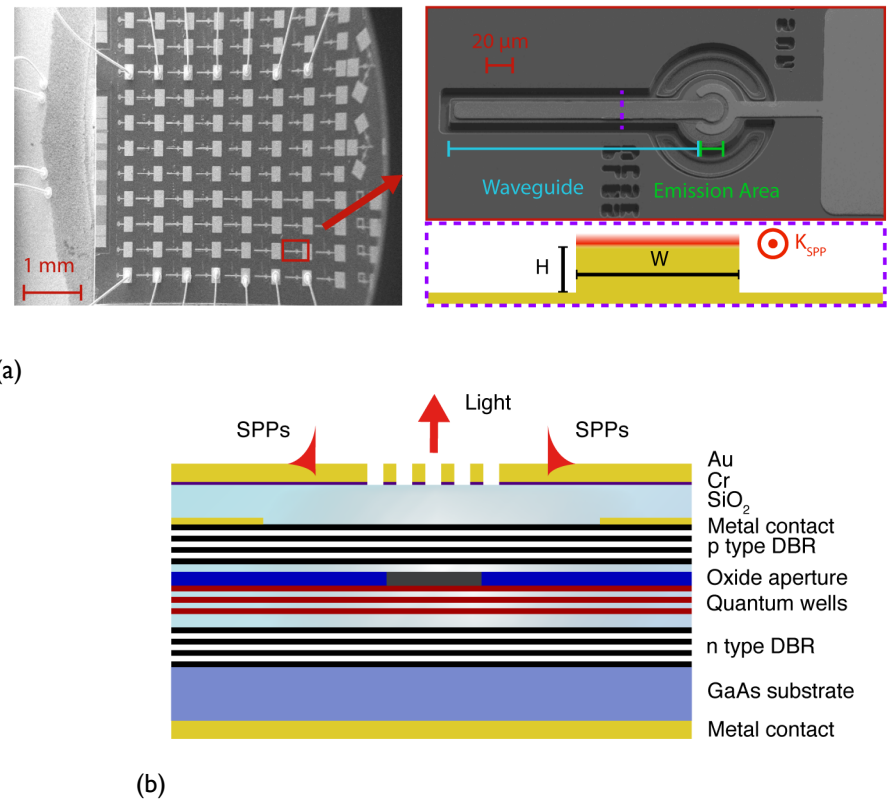

Figure 5.1 (a) SEM image of an on-chip VCSEL array with a single VCSEL highlighted. A cross section of the stripe waveguide is shown with the dimensions labelled as width (W) and height (H). (b) Cross section of a VCSEL - The emission area, and thus SPP excitation region, is defined by the underlying position of the oxide aperture[114].

The VCSEL free space wavelength of 850 nm corresponds to a SPP propagation length of approximately 60 µm, and matches the first optical fibre transmission window. A threshold current of 0.6 mA was typically exhibited by the diodes, which also operated with a single mode until approximately 0.8 mA. This fundamental transverse mode possesses a Gaussian profile that is suitable for coupling to SPPs via simple, one-dimensional nanoslit gratings. Furthermore, the output is relatively unpolarised, meaning that the gratings may be placed with any orientation above the emission area to provide SPP excitation in the two opposing directions that are perpendicular to the long axis. To demonstrate SPP excitation, periodic nanoslits were milled into the VCSEL Au-Cr layers using a FIB, with the long axis orthogonal to the direction of the plasmonic waveguide. Applying a forward bias to the VCSEL resulted in optical emission, with a portion of the emitted light coupling to SPPs that subsequently propagated onto the waveguiding structure.

5.2 SPP Waveguiding

The gold slab adjacent to the emission area forms a stripe plasmonic waveguide, which may support multiple modes, depending upon its width, W. Mode formation in these waveguides may be considered in terms of SPP reflection at the stripe boundaries[115, 116], together with edge effects[117]. The numerically calculated effective index n_{SPP} of the plasmonic modes supported by both 15 μm and 1 μm wide waveguides approximately equals the index of planar SPPs ($n_{SPP} \approx 1.018 + 0.001i$) as determined by Equation 2.15, for a free space wavelength of 850 nm.

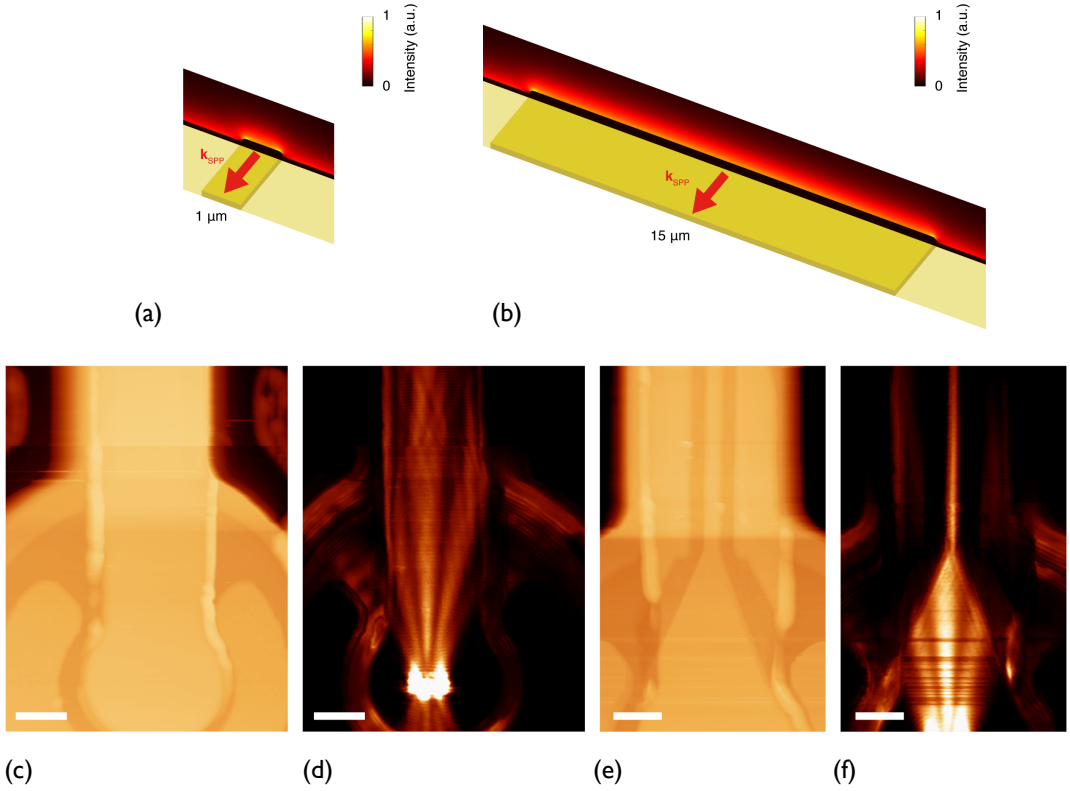

Figure 5.2 (a, b) Simulation: numerical eigenmode calculations, illustrating the in plane power flow for a stripe waveguide with (a) W = 1 μm and (b) W = 15 μm, where H = 100 nm in both images. (c – f) Experiment: Topographies and near-field images of multimode (c, d) and singlemode (e, f) waveguides on VCSELs. As the Au thickness is 200 nm, with a 50 nm Cr underlayer, the leakage of the modes into the substrate is negligible.

Figures 5.2a and b display the in plane SPP power flow, where k_{SPP} is directed into the plane, for the two stripe widths, highlighting the fact that most of the mode energy resides on the flat interface. A large stripe height, H, ensures minimal interaction between the waveguided modes and the lower Au surface. Whilst a degree of field localisation occurs at the corners, it does not play a significant role.

Additionally, rounding the edges of the stripes in the simulation, to more closely resemble the fabricated structures, reduces this hotspot effect.

Figures 5.2c-f illustrate the near-field study, via SNOM, of SPP waveguiding on VCSELs. Gratings ion etched into the gold films excite SPPs that are apparent in the near-field images as high intensity beams that decay exponentially with distance from the emission area. The localisation of optical energy to the near-field is confirmed by the absence of these features in far-field images obtained when the SNOM probe was not in contact with the surface. Additionally, propagation of SPPs away from the emission area and onto the multimode waveguide in Figure 5.2d is reasonably efficient when W is large. Gradually tapering a stripe waveguide effectively filters the signal, such that the mode maintains a constant lateral profile across the length of the waveguide, as presented by Figure 5.2f. Notably, the multimode profile, shown in Figure 5.2d, alters as the signal propagates, suggesting that interference occurs between reflected SPP waves.

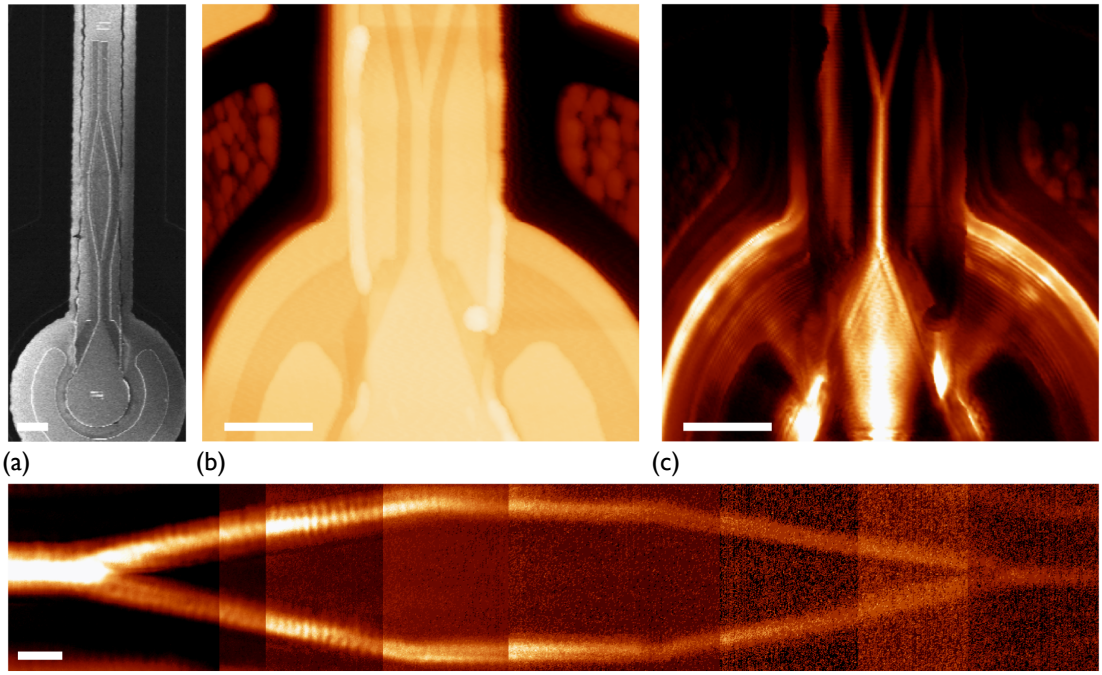

Figure 5.3 Experiment: Mach–Zehnder interferometer integrated on a VCSEL. (a) SEM (b) topographic and (c) near-field images of the interferometer. (d) Near-field images of the two interferometer branches. The input SPP signal is split into two branches, which are later recombined, with the resulting interference producing a modulation in the output SPP signal.

More complex, passive structures may also be implemented on VCSELs, such as

a Mach–Zehnder interferometer, which is particularly suited to biosensing applications[118]. Figure 5.3a outlines such an interferometric structure integrated on a VCSEL, wherein the plasmonic signal propagates onto the two separate branches that extend for a few microns before subsequently recombining, which allows the SPP waves to interfere. As a result, the output SPP intensity depends upon the phase difference between the signals on the two branches, which may be modulated, for instance, when molecules are absorbed onto the metal surface. Monitoring the output signal therefore enables the presence of molecules to be inferred, as the SPP path lengths are perturbed. Further control over the propagation of SPPs on a VCSEL platform can be achieved by integrating additional scattering structures into the waveguides, including plasmonic elements such as Bragg mirrors and nanoparticles that provide beam focusing. Such structures offer passive control over the direction of the SPP, nonetheless it is also feasible to manipulate the mode wavelength.

5.3 SPP Frequency Conversion

SPP Frequency conversion is possible on the VCSEL platform by incorporating a layer of quantum dots (QDs) adjacent to the metal film[119]. The VCSEL emission generates SPPs with a wavelength close to 835 nm, which lies within the absorption band of PbS quantum dots, and thus the plasmonic signal may efficiently excite the dots that reside on the waveguide. Subsequent decay of these electronic excited states results in the excitation of SPPs with a wavelength determined by the PbS emission spectrum. Importantly, the Stokes shift ensures a red-shift in the peak plasmonic wavelength, and thus the system demonstrates effective SPP-to-SPP frequency conversion. This frequency conversion was verified by collecting the light that originated from out-scattering of SPPs at the end of gold stripe, after the signal had effectively traversed the waveguide and interacted with the layer of QDs. The broad peak shown in Figure 5.4a is thus equivalent to the SPP spectrum, and overlaps with the expected QD emission, peaking at ~1500 nm.

It worth noting that in order to transmit data along an optical fibre via wavelength division multiplexing, a wavelength separation is required between channels, allowing multiple signals to be transmitted. Typically the standard separation between channels is 0.8 nm for wavelengths near 1550 nm and thus a

broad, continuous spectrum, as shown in Fig 5.4a, is not immediately suitable for this application[120]. Moreover, it is evident that the maximum detected signal increases linearly with applied current, once the lasing threshold current has been exceeded, in this case > 2mA. Hence, the experiment illustrates on-chip manipulation of the SPP wavelength, a key process for plasmonic technology. Furthermore, VCSELs may serve a second role in plasmonic circuitry, in addition to being an electrically pumped SPP source.

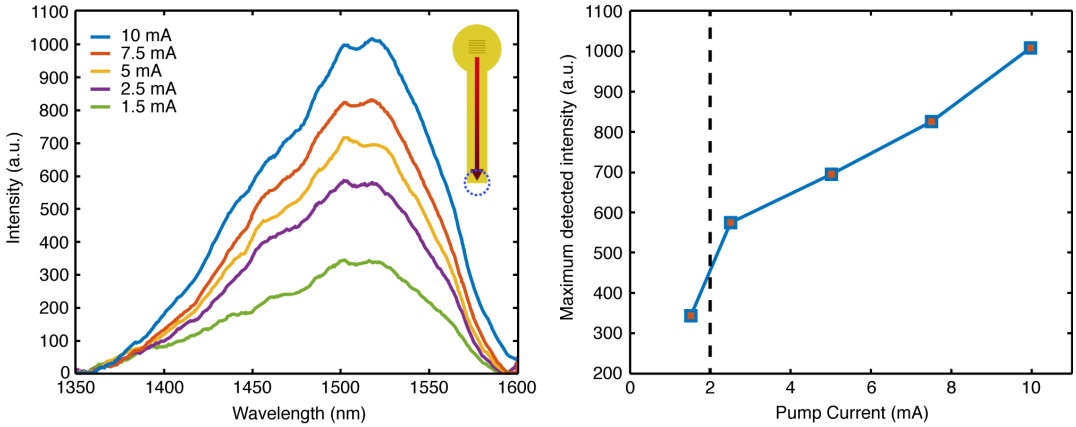

Figure 5.4 Experiment: Shifting the SPP frequency on VCSELs. (a) Spectrum of the collected light as the current is varied. The peak emission wavelength of the PbS dots was close to 1500 nm. The insert shows the collection area, wherein SPPs out-couple due to scattering at the end of the waveguide. (b) The dependence of the peak intensity on the pump current. The threshold current for this particular diode was ~2 mA, as shown by the dashed line.

5.4 Detection of SPPs

SPP detectors are one of the basic components required to process plasmonic signals, in tandem with sources, modulators and passive waveguides. Electrical generation and detection of SPPs is particularly advantageous for on-chip plasmonic circuitry, allowing further integration with other electronic components. Consequently, electrical detection of plasmonic signals has been previously demonstrated[121-124], which typically involves the generation of electron-hole pairs via SPPs directly, or indirectly - by light resulting from out-coupling.

Photodetection is a significant application of p-n junctions, which entails an incident photon generating an electron-hole pair that subsequently gives rise to a photocurrent. If no bias is applied, the diode operates in photovoltaic mode,

resulting in a voltage being established. Conversely, applying a reverse bias, in the photoconductive mode, widens the depletion junction, yielding a higher responsivity (ratio of photocurrent to incident optical power). VCSELs, as laser diodes, may thus function as a photodetector when operated in reverse bias, thereby serving dual roles in photonic components[125]. Upon illumination, the thin active layer only weakly absorbs the incident radiation. However, as light is recycled within the cavity, the multiple reflections increase the probability of photocurrent generation[126]. It is important to consider that light incident on a VCSEL may also reflect from the upper DBRs, therefore reducing the proportion that enters the active region. Removing several of the upper DBR layers would thus allow greater percentage of the incident radiation to contribute to a photocurrent. Nonetheless, this has a detrimental effect on the Q-factor, and as a result there is a trade off between the light emission and detection roles. In addition, the presence of oxide modes, due a refractive index variation between the oxidised and non-oxidised regions, may be inferred from photodetection peaks occurring at wavelengths spectrally shifted with respect to the cavity emission[39].

In this regard, VCSELs have the capability of detecting SPPs, once the have been scattered into free space radiation that subsequently propagates into the diode. To demonstrate this, plasmonic groove and slit gratings were ion milled onto a VCSEL, acting as the SPP input and output structures respectively, which is illustrated by Figure 5.5b. The groove grating is located on the waveguide, and serves to launch SPPs that propagate towards the emission area. Centred above the oxide aperture is the slit grating that acts to out-couple SPPs to light, with a proportion of this radiation entering the cavity. It is essential that the input grating be composed of grooves, to safeguard against direct transmission into the cavity.

The experimental setup that was employed is outlined by Figure 5.5a, which allows the photocurrent to be monitored by an ammeter, placed in series with the diode. Focusing the emission of an 850 nm, 100 mW diode and scanning the spot across the VCSEL surface permits the resulting photocurrent to be spatially resolved. Additionally, a reverse bias may also be applied across the VCSEL, so as to increase the responsivity, and, as the photocurrent is on the order of nanoamps, a picoammeter was utilised to record the signal.

Evidently, two hotspots are present in the photocurrent map of Figure 5.5c,

corresponding to the two gratings. Direct transmission into the cavity, when the illumination was incident upon the slit grating, produces a spot comparable in size to the VCSEL oxide aperture. Signal localised above the groove grating relates the SPPs out-coupling into the cavity, confirming the detection ability of VCSELs. Moreover, the hotspots disappear when the illumination is TE polarised, as shown by Figure 5.5e, confirming the plasmonic origin of the signal. Lastly, Figure 5.5d presents the photocurrent map when only a slit grating was milled into the VCSEL surface, which illustrates only one hotspot.

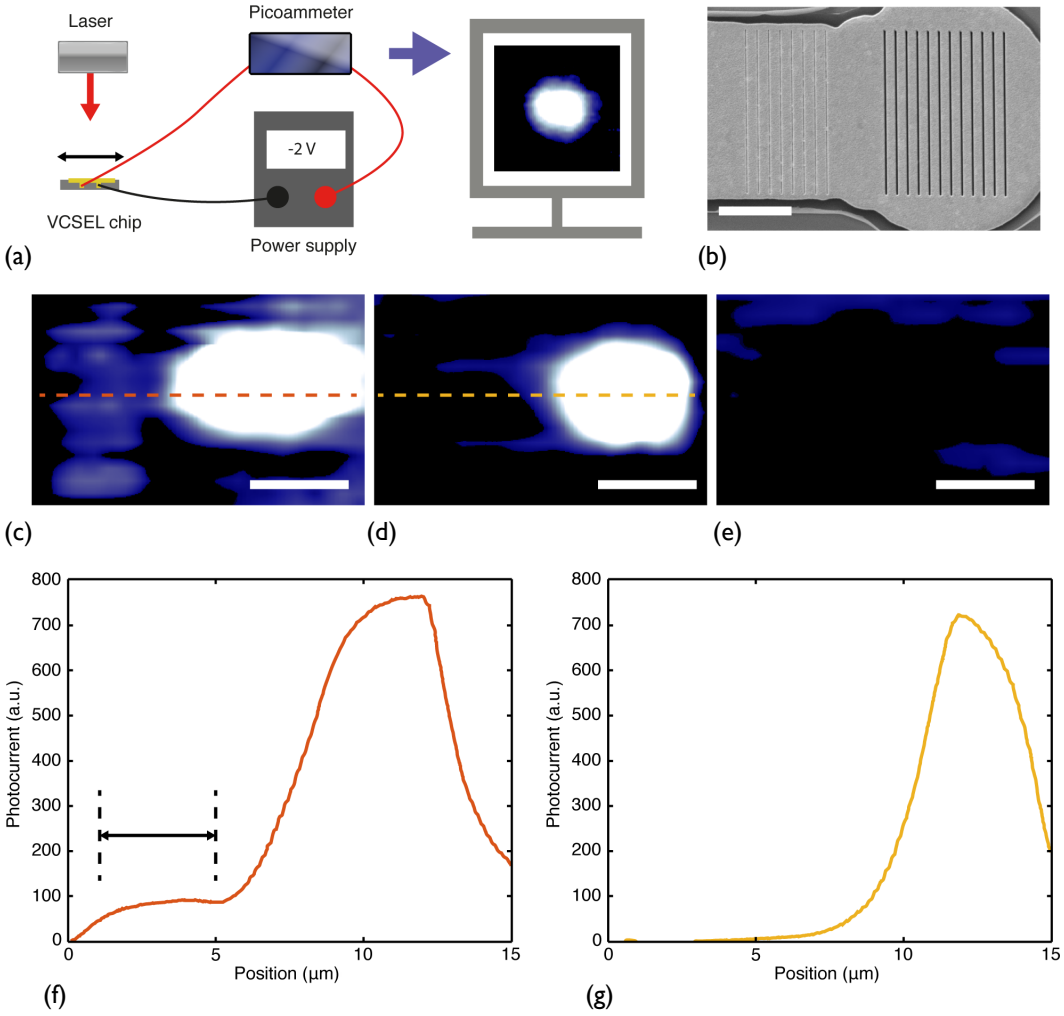

Figure 5.5 Experiment: (a) Reverse bias setup for illustrating the detection of SPPs via spatially resolving the photocurrent (b) SEM image of the groove and slit grating milled in a VCSEL. Photocurrent maps: (c) TM polarised illumination of the slit and groove gratings. The 8 grooves have a 50 nm width with an 800 nm period, whilst the 12 slits are 100 nm in width, with a 760 nm period. (d) TM illumination of an isolated slit grating, displaying a single hotspot. (e) TE illumination of slit and groove gratings, corresponding to structure in (c). (f) and (g) are cross sections of (c) and (d) respectively. The position of the groove grating is marked with a line in (f).

In this proof-of-principle experiment there are many sources of loss, requiring a high power diode to provide the illumination. For instance, only a fraction of incident radiation will couple to SPP via scattering from the groove grating. Following this, the signal decays almost exponentially due to losses arising from propagation on the gold film. Once the signal reaches the output slit grating, a proportion of the incident SPP intensity is then out-coupled in the direction of the VCSEL cavity. The radiation that is not initially reflected by the DBRs, and successfully enters the cavity, may then generate a photocurrent. Nonetheless, whilst these diodes have not been optimised for photodetection, they still exhibit the ability to detect SPP signals. Subsequent improvements over the diode geometry may yield more efficient SPP detection.

Since VCSELs detect the out-coupled light originating from SPPs, the diode's quantum efficiency is applicable as a figure of merit, which is defined as the number of electrons produced divided by the number of photons absorbed. Responsivity R and quantum efficiency η are thus related via $R = \eta\left(q/h\nu\right)$, where q is the electron charge, h is Planck's constant and ν is the optical frequency. There are many factors in this experimental demonstration that cannot be easily quantified, e.g. the in and out coupling magnitudes and propagation loss, and hence determining a detection efficiency of SPPs is difficult. Looking at previous work on VCSEL photodetection, Dragas et al. demonstrated a quantum efficiency of 14% under zero applied bias, with an avalanche gain of 10 under reverse bias. Additionally, photodetectors based on VCSELs with the upper DBR layers partially removed have exhibited efficiencies of up to 73%[125]. Consequently, VCSELs represent a practical means of on-chip electrical SPP detection.

5.5 Summary

Over the course of this chapter we have discussed the development of a VCSEL platform for plasmonics, on which we have demonstrated on-chip SPP waveguiding, frequency conversion and signal detection. Additionally, in order to ensure the high performance of VCSELs, the SPP excitation efficiency must be maximised.

Chapter 6

Directional Excitation of Surface Plasmon Polaritons on VCSELs

In the chapter, we will address the numerical design of nanostructures for efficient generation of SPPs in a unique direction on VCSELs, together with experimental verification using SNOM.

6.1 Asymmetric SPP excitation

As we have covered in the previous chapter, ion milling gratings onto the VCSEL emission area allows for the effective generation of on-chip plasmonic beams. However, normal incidence illumination of these structures produces two SPP beams propagating in opposing directions, perpendicular to the long axis of grating. In this regard, essentially half of the plasmonic signal propagates in the opposite direction of the waveguide, thereby constituting a loss channel, as evidenced by Figures 5.2d and 6.1. Thus, in order to optimise the coupling of VCSEL emission to plasmonic modes, the signal must be launched directionally, i.e. exclusively towards the gold stripe. The challenge of optimising the coupling of light to SPPs has been extensively considered in the recent literature, and the methods utilised to this effect may be broadly sorted into the following categories: oblique incidence on slit structures[127-129], grooves structures[130-133], antennae[134,135], cavities[136], gratings[137], Bragg reflectors[138], phase engineering slit emission[139,140], blazed structures[141], dual excitation beams[142] and near-field interference effects[143]. Most likely, there is no single optimal structure, but rather the choice of geometry is dependent upon the particular application. Effective compatibility with the VCSEL geometry stipulates that the asymmetric excitation method be practical (e.g. not contain apertures of various dielectrics) and operate in transmission coupling (i.e. contain apertures) at normal incidence.

Figure 6.1 considers more closely the gratings employed to excite SPPs on VCSELs, as discussed in the previous chapter. The individual slits are visible in the near-field image, together with the two plasmonic beams, almost equal in amplitude,

propagating in opposite directions.

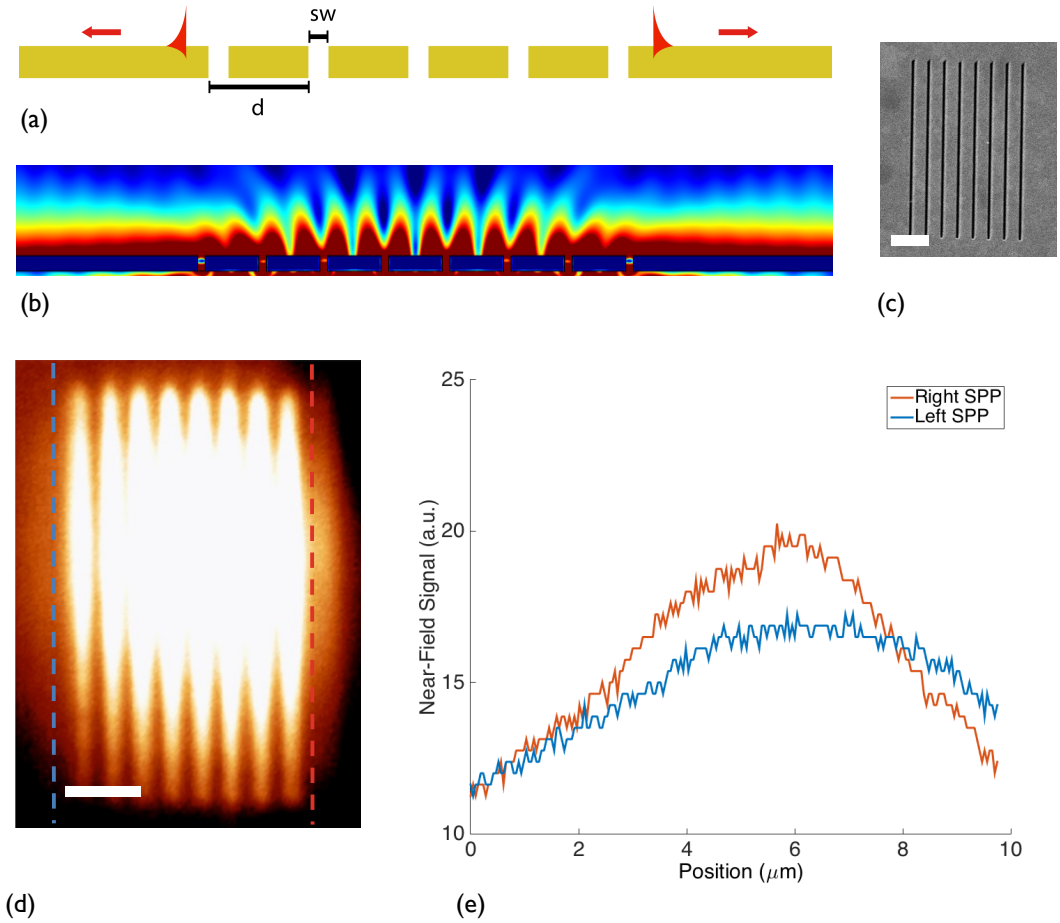

Figure 6.1 Symmetric slit grating: (a) Schematic of the grating, where the period d = 800 nm and the slit width sw = 100 nm. (b) Simulation: norm of the electric field upon illumination with a Gaussian beam. (c) Experiment: SEM image of the grating milled in a VCSEL. (d) Experiment: SNOM image of grating, with cross sections shown in (e). Scale bars correspond to 2 μm.

Additionally, as the size of the VCSEL beam and plasmonic grating is comparable, it is essential that the incident emission be centred upon the grating, as asymmetric illumination may result in an apparent directional signal. In essence, the challenge of optimising SPP coupling entails redirecting all of the incident energy into a SPP channel in a single direction, and clearly out coupling counter-propagating SPPs does not help to achieve this. We may consequently define three conditions for a directional plasmonic structure:

1. **High efficiency** - Maximal coupling in a unique direction upon normal illumination with a 850 nm wavelength Gaussian beam

2. **Robust** – small variations in the geometrical parameters do not significantly affect the performance
3. **Compact** – the structure should fit within the output area of VCSELs

Quantifying the performance of plasmonic structures is possible by defining the appropriate figures of merit. Accordingly, to determine the ability of structures to launch SPPs preferentially in a single direction, we term directionality as the SPP power flow in a single direction, divided by the total SPP power flow:

$$D = \frac{P_R}{P_R + P_L} \tag{6.1}$$

Where P_R and P_L are the SPP power flows in the right and left directions respectively, i.e. we are considering SPPs with antiparallel propagation constants, such as modes launched by gratings under TM illumination. From this definition, as also used by Sonnefraud et al., D = 0.5 equates to symmetric coupling; 1 equates to a signal travelling exclusively to the right, and if D = 0, then SPPs propagate solely to the left. Following on from this, we will arbitrarily choose to optimise coupling to the right, when D > 0.5. Also, the coupling efficiency describes how much of the energy impinging on the structures is coupled to SPPs, and we designate it in the right direction as:

$$CE_R = \frac{P_R}{P_0} \tag{6.2}$$

Where P_0 is the power incident on the aperture area, without the presence of the actual structure, i.e. setting all domains in the simulation model to the substrate dielectric material. Alternatively, if we defined the coupling efficiency with respect to the total incident power, then this figure would depend on the beam width, making it unsuitable for comparisons between structures. Equations 6.1 and 6.2 are clearly linked, as they both contain the P_R term. However, they can be modified independently of each other, and thus it is critical to maximise both. Equation 6.2 must also take into account the exponential power decay of SPPs as the modes propagate, and hence we may write $P_R = P_X / \left[\exp\left(-2\,\mathrm{Im}\left(k_{SPP}\right)X\right)\right]$ where P_X is the

power flow evaluated at a distance X from the SPP source, e.g. edge of the slit aperture.

The simplest aperture geometry is perhaps a single hole, which launches SPPs with a two-dimensional dipolar emission pattern, with its axis orientated along the polarisation direction of the illumination[144]. In contrast, due to their extended nature, slits and slit gratings impose a degree of directionality as they excite SPP beams in only two opposing directions, perpendicular to the long axis. Ergo, we will consider a slit as the basic aperture unit to be subsequently modified to yield excitation in a unique direction. Nanoaperture coupling has been considerably studied, and the precise coupling mechanism to SPPs may be examined from different perspectives. Here, we will consider the subwavelength aperture to produce a spectrum of wavevectors, given by a Fourier transform of the slit field, and thus a proportion of the transmitted energy couples to SPPs via phase matching[145]. Moreover, illuminating a slit with a TM polarised wave induces displacement of the conductions electrons in gold. As the slit surface is discontinuous, current cannot cross the aperture and thus charge accumulates at the edges. This results in horizontally oscillating electric dipole, which may be considered as the source of radiation, including SPPs[146].

In view of the large parameter space, the challenge of optimising aperture coupling at normal incidence is indeed significant. Looking at the problem from an engineering perspective, a viable approach involves designing a structure that yields asymmetric scattering (e.g. due to an asymmetric profile), and subsequently optimising the geometry using numerical methods.

6.2 Slit-Groove Structures

A 100 nm wide slit in a 200 nm thick gold film (equivalent to the VCSEL Au layer) yields an efficiency of $CE_R \approx 0.16$ and thus, upon illumination with an 850 nm wavelength Gaussian beam, approximately 16% of the energy incident on the slit is coupled to SPPs. Following this, adding a groove (indentation) adjacent to a subwavelength slit results in asymmetric scattering, and thus a directional plasmonic signal, as outlined by Figure 6.2. Compared with Bragg reflectors, single grooves are more compact, and may be easily integrated into periodic structures. The electric

field distribution plotted in Figure 6.2b clearly illustrates the asymmetric excitation, which may be appreciated in terms of coupling to modes within the groove.

SPPs launched by the slit may transmit directly across the groove, or be coupled sideways, generating gap plasmons. These slot modes subsequently scatter at the groove exit, also launching single interface SPPs. As a result, SPPs excited by the groove may interfere destructively with SPPs directly transmitted across the groove, and thus effectively the groove acts as a mirror. Moreover, the groove may also behave as a slot mode cavity, due to multiple reflections at the groove base and exit, leading to resonant effects[147].

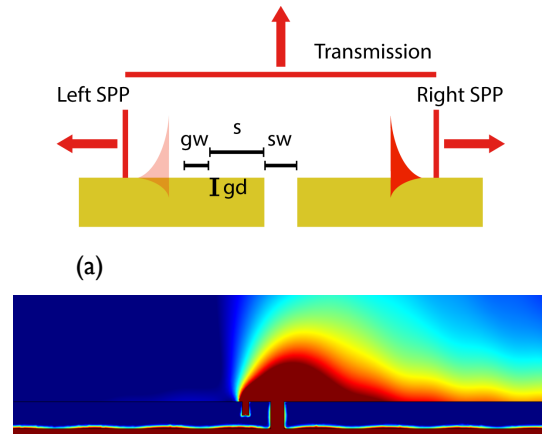

Figure 6.2 Slit-Groove: (a) The geometrical parameters are defined as gd (groove depth), gw (groove width), s (separation) sw (slit width). Also shown are the integration lines for determining the power flow of SPPs and far-field transmission. (b) Simulation: norm E, with the directionality arising due to interference.

A slit-groove structure with subwavelength dimensions consequently generates a directional plasmonic signal, and, in order to achieve the highest possible performance, Monte Carlo optimisation was employed to determine the geometrical parameters. The figure of merit F encapsulates both Equations 6.1 and 6.2, where:

$$F = (2D - 1) \cdot CE_R \tag{6.3}$$

Using this definition, maximising F ensures a large directionality and coupling efficiency. In the case of symmetric coupling, F goes to zero, whilst if all of the incident energy is coupled to right propagating SPPs, F reaches unity. During the optimisation process, all the geometrical parameters defined in Figure 6.2a are thus

randomly varied within a realistic range, such as to arrive at the largest value of F. The optimisation procedure was run multiple times with different initial conditions and boundaries, and the following parameters were found to yield a high performance: gd = 100 nm, gw = 50 nm, s = 150 nm, sw = 100 nm (parameter set 1). The addition of a single groove yields and efficiency $CE_R \approx 0.3$, thus coupling 30% of the incident energy, and directionality $D \approx 0.9$, leading to $F \approx 0.24$. This increase is perhaps made more perceptible by normalising the SPP power generated by a slit-groove with respect to the power of SPPs launched by an isolated slit:

$$P_{R,N} = \frac{P_{R,Slit-Groove}}{P_{R,Slit}} \tag{6.4}$$

Thus if $P_{R,N} > 1$ then the structure offers an increased coupling efficiency over a single slit. Similarly, the far-field transmission may be normalised with respect to an isolated slit as: $P_{T,N} = P_{T,Slit-Groove} / P_{T,Slit}$. Figure 6.3 addresses the spectral response of a slit-groove structure, illustrating the broadband nature of the asymmetry.

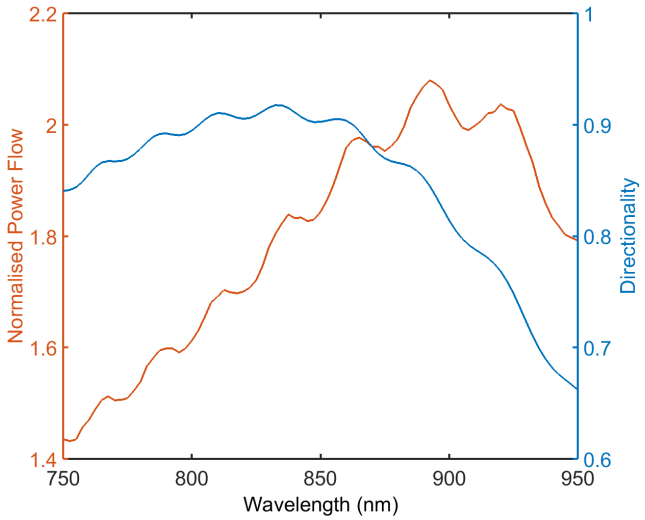

Figure 6.3 Simulation: Normalised SPP power flow (Equation 6.4) and directionality (Equation 6.1) as a function of the illumination wavelength, for a slit-groove (parameter set 1).

From Figure 6.3, it is evident that a slit-groove structure may offer improved performance over an isolated slit, as both figures of merit maintain a high value across the range 750 – 950 nm.

As previously mentioned, the process of reflection from grooves may be considered from the perspective of a side-coupled gap plasmon cavity[148]. Thus varying the groove width alters the gap mode dispersion (Figure 2.4a), changing the

phase of light emitted by the groove in the process. Additionally, the groove depth effectively defines the slot cavity length, and as a result the parameters gw and gd may be tuned to provide a resonant response from the groove. The geometry here contains an additional slit, and therefore varying the slit-groove separation (s) provides further insight into the asymmetric scattering process, as presented by Figure 6.4

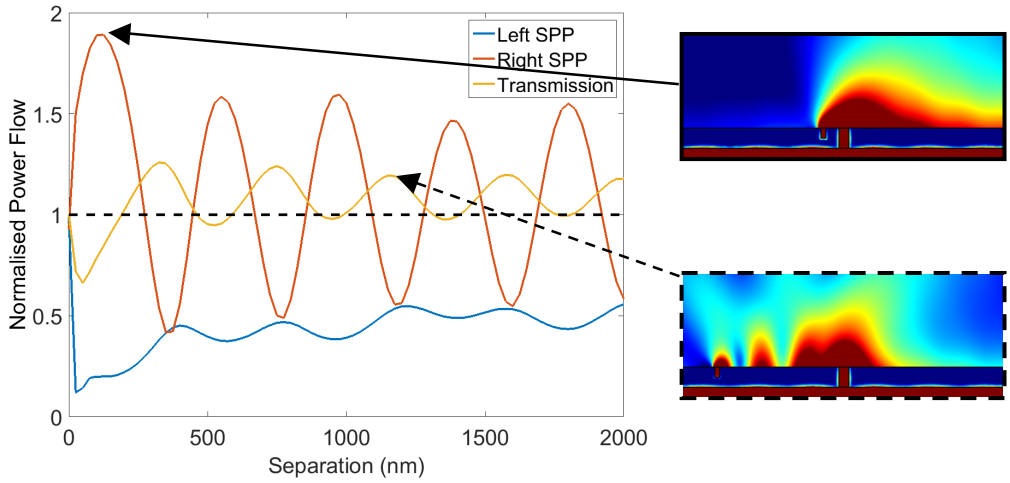

Figure 6.4 Simulation: SPP and transmission power flow of a slit groove structure, normalised with respect to an isolated slit ($P_{R,N}$, $P_{L,N}$ and $P_{T,N}$), as the slit-groove separation s is varied (parameter set 1). Norm E is plotted for two different separations, illustrating a large directional SPP signal and high transmission.

An obvious oscillation occurs in Figure 6.4, as minima in the right propagating SPP intensity occur in tandem with peaks in the far-field transmission. Moreover, at these points, the right and left SPP intensities becomes almost equal and equivalent to half of the intensity launched by an isolated slit. Looking at the wavelength these minima occur at, it is evident that they approximately coincide with $q(\lambda_{SPP}/2)$, where q is an integer, suggesting that SPP resonances are supported between the slit and groove. SPP anti-nodes are also visible in the electric field distribution shown in the right panel of Figure 6.4, matching the mode number. Hence, at these groove-slit separations, energy is essentially redirected away from SPPs propagating on the film, and into far-field transmission. Furthermore, patterning a number grooves adjacent to a subwavelength aperture has been extensively utilised to

demonstrate plasmonic beaming, in which the transmitted beam exhibits a reduced divergence[149,150].

Neglecting the role of slit-groove resonances, the phase difference between SPPs excited by the groove to the left with respect to SPPs directly transmitted across the groove is unaffected by varying the slit-groove separation. Thus destructive interference always occurs to the left, as the groove forms an effective mirror. However, the presence of slit-groove resonances introduces resonant scattering with an associated sharp phase shift, which would account for the dramatic decrease in SPP intensity to the right.

The structure also proves to be robust; for instance, setting sw = 150 nm, gw = 100 nm, gh = 70 nm and s = 200 nm yields an efficiency of 0.26, directionality of 0.6 and thus $F = 0.052$. This is beneficial for the effective fabrication of the structures, as high precision is not required. Using the smallest slit-groove separation is preferable, for it ensures a small structural footprint. If the slit and groove widths are equal, the geometry still yields asymmetric scattering, albeit with reduced efficiency. However, when the groove depth is equal to the film thickness, then the structure becomes a double slit, and in this case, the two apertures must differ in width, or constituent dielectric material, to achieve directionality[136].

A slit with a width of 100 nm will evidently only capture a small proportion of the incident energy of a 5 μm FWHM Gaussian beam, which approximates to the VCSEL emission. As a result, including multiple scattering elements in the illumination area can increase the overall intensity of SPPs launched by VCSEL emission.

6.3 Slit-Groove Gratings

If we consider a slit-groove to be a unit cell, we may add additional structures within the beam area, thus coupling more of the incident optical energy to SPPs. Taking two unit cells, the separation between them must be tailored to provide the greatest figures of merit. The intensity of SPPs propagating to the right peaks when the period d, for two cells, is close to 800 nm, which is also equivalent to the period for resonant excitation on symmetrical gratings. This suggests that if we generate a structure composed of the unit cells repeated periodically, we might

take advantage of diffraction coupling via the slits, together with the directionality offered by the grooves.

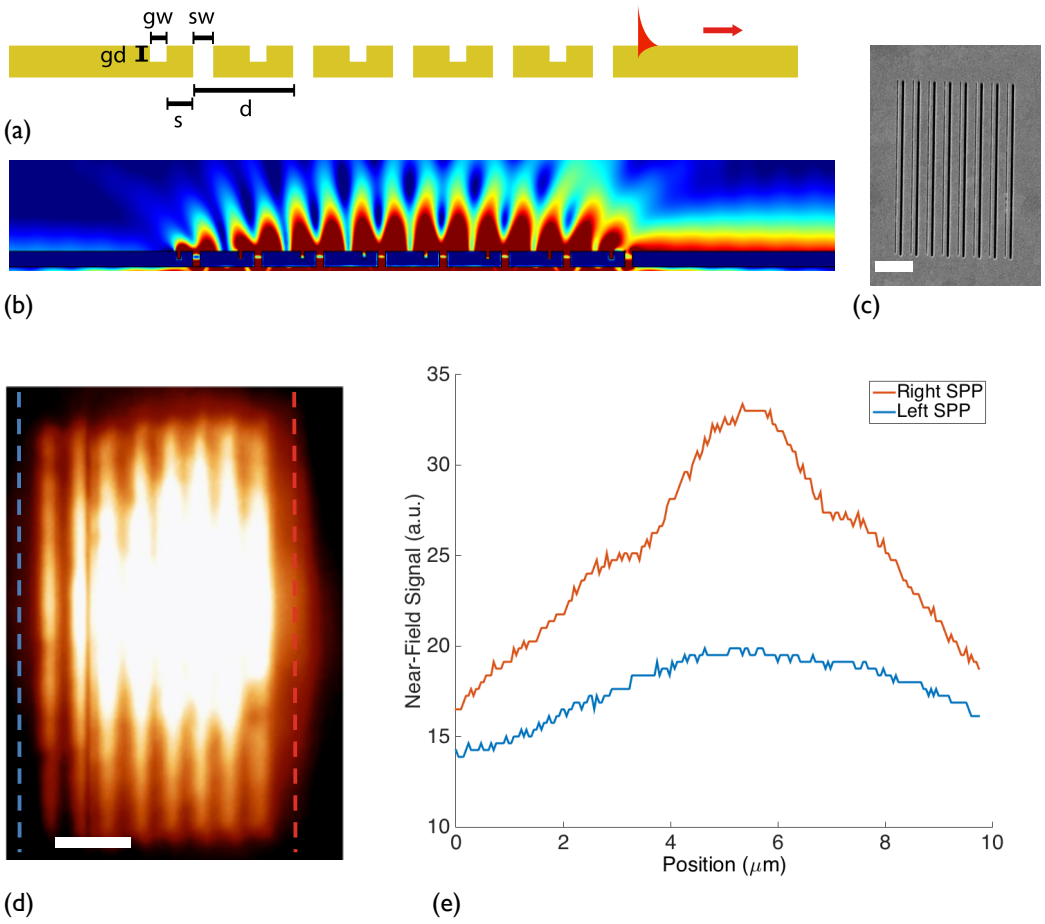

Figure 6.5. Slit-Groove Grating: (a) Schematic of a slit-groove grating (b) Simulation of the norm E, where the geometrical parameters are d = 800 nm, sw = 100 nm, gw = 50 nm, s = 150 nm (c) Experimental: SEM image of the grating milled into a VCSEL (d) Experimental: SNOM image of grating, with cross sections shown in (e). Scale bars correspond to 2 μm.

Hence, in effect the reflector is integrated into the excitation grating, ensuring that the coupler dimensions are minimised. In contrast, typical SPP mirrors, such as Bragg reflectors, lie outside the excitation grating, thus requiring a larger area for generating directional beams. As with the previous structure, we employed Monte Carlo optimisation to determine the optimal geometrical parameters, including the period.

Figure 6.5 outlines a slit-groove grating, with the simulated power flow distribution evidently exhibiting a directional signal. The experimental near-field image also confirms the asymmetry, yielding a directionality of approximately 0.65.

We may consider the structure to be composed of an excitation, slit-grating and a reflection, groove-grating offset by a distance equal to the separation (s) plus the groove width (gw). Since the periodicity of both gratings is equal, effects observed in Moire surfaces (e.g. a beat frequency due to the superposition of two similar periodicities) or biharmonic gratings are not expected[151]. Additionally, chirped gratings, which entail a linear change in period across the structure, and aperiodic groove structures have also demonstrated control over SPP excitation[88,152].

An ostensible downside of adding grooves to a grating is that SPPs that are already propagating in the desirable direction have a greater probably of out-coupling or reflecting, decreasing the performance of the structure in the process. However, introducing a smooth decrease in the groove depth across the structure can reduce this deleterious effect. Generally, the smaller the depth, the higher the probability SPPs will be transmitted, though this effect is dependent on the groove dimensions and the incident wavelength. The transmission of SPPs across a groove is examined by Figure 6.6, which highlights the gradual decrease in reflectivity as the depth is reduced.

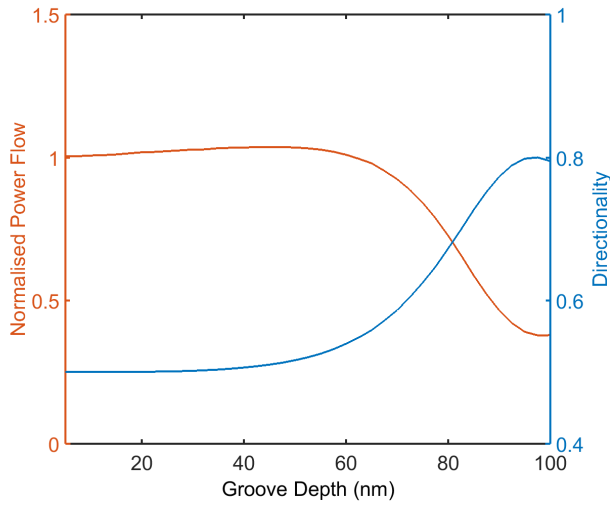

Figure 6.6 Simulation: SPP power transmitted across a groove, normalised with respect to the case without a groove (isolated slit). Here the slit-groove separation s = 600 nm, corresponding to the groove of an adjacent unit cell (on the right), as per the grating addressed in Figure 6.5. A gradual decrease in the SPP reflectivity is evident as the depth is reduced.

In terms of fabrication, ion milling precise groove depths is difficult; nonetheless, a linear decrease in the dwell time provides a graded decrease in depth, as delineated by the SEM image of Figure 6.7c. A decrease in the out-scattering losses

is apparent from the electric field distributions when comparing Figures 6.5b and 6.7b. What is more, the experimental near-field image also displays an increased directionality of ~ 0.7. Simulations of the structures indicate that the directionality, at 850 nm, of the constant groove depth grating, is approximately 0.8, whilst the graded depth grating is 0.9. In addition, introducing the gradual decrease in groove depth increases F from 0.2 to 0.6. The lower performance of the experimental results compared to the simulations could be partially attributed to deviations from the designed geometrical parameters, and rounding of the groove and slit edges, stemming from ion milling.

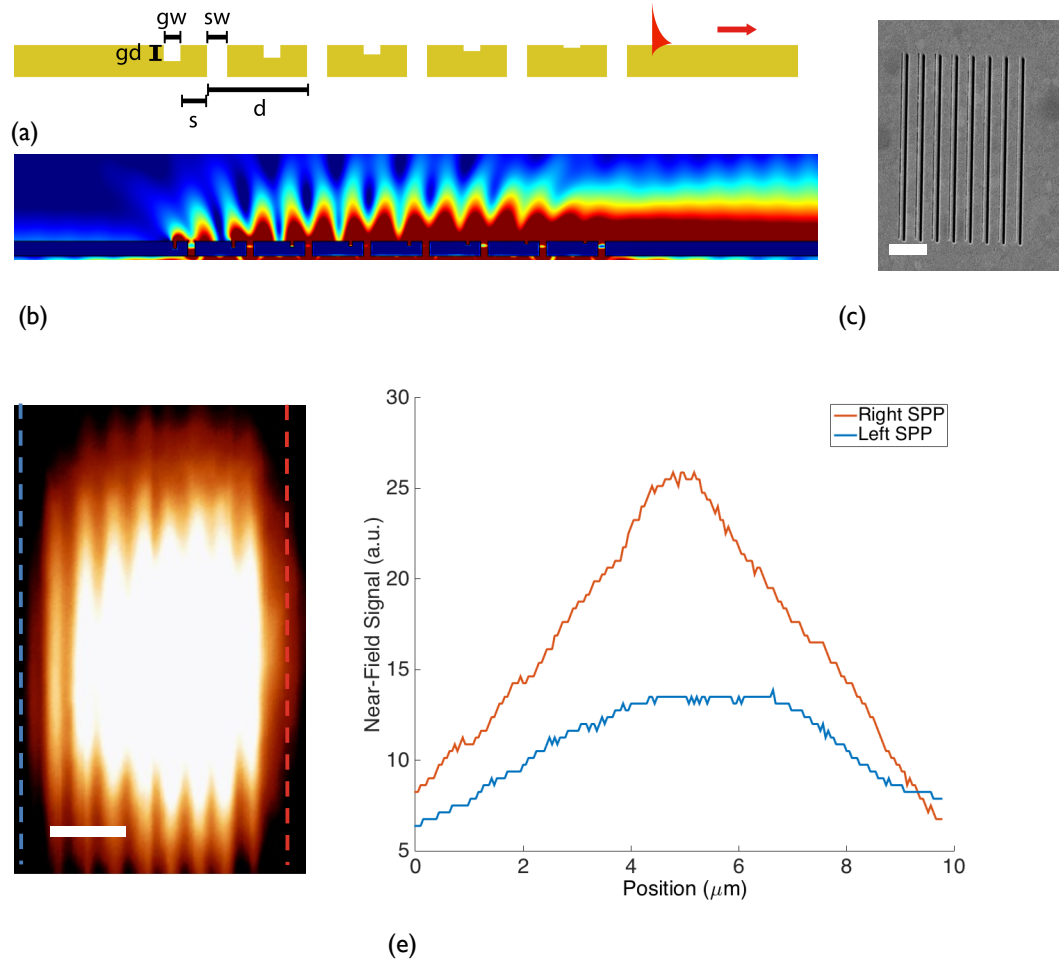

Figure 6.7 Slit-Groove Grating: (a) Schematic of a slit-groove grating (b) Simulation of the norm E, where the geometrical parameters are d = 800 nm, sw = 100 nm, gw = 50 nm, s = 150 nm (c) Experiment: SEM image of the grating milled into a VCSEL. A linear decrease of groove depth is introduced from left to right, decreasing the SPP reflectivity. (d) Experiment: SNOM image of grating, with cross sections shown in (e). Scale bars correspond to 2 μm.

Moreover, the grating structure also exhibits a broadband response, similar to the unit cell, as attested to by Figure 6.8a, wherein the directionality exceeds 0.6 across a 200 nm range. The SPP power flow, normalised to SPP power launched by a slit grating, maintains a value higher than 1 in the range 830 - 870 nm, confirming that the asymmetry arises from a redirection of optical energy, and not from increased out-coupling losses in the opposite direction. Also, figures 6.8b-d display the hyperspectral SNOM images obtained from the same structure on an isolated Au film, which further demonstrates the broadband response.

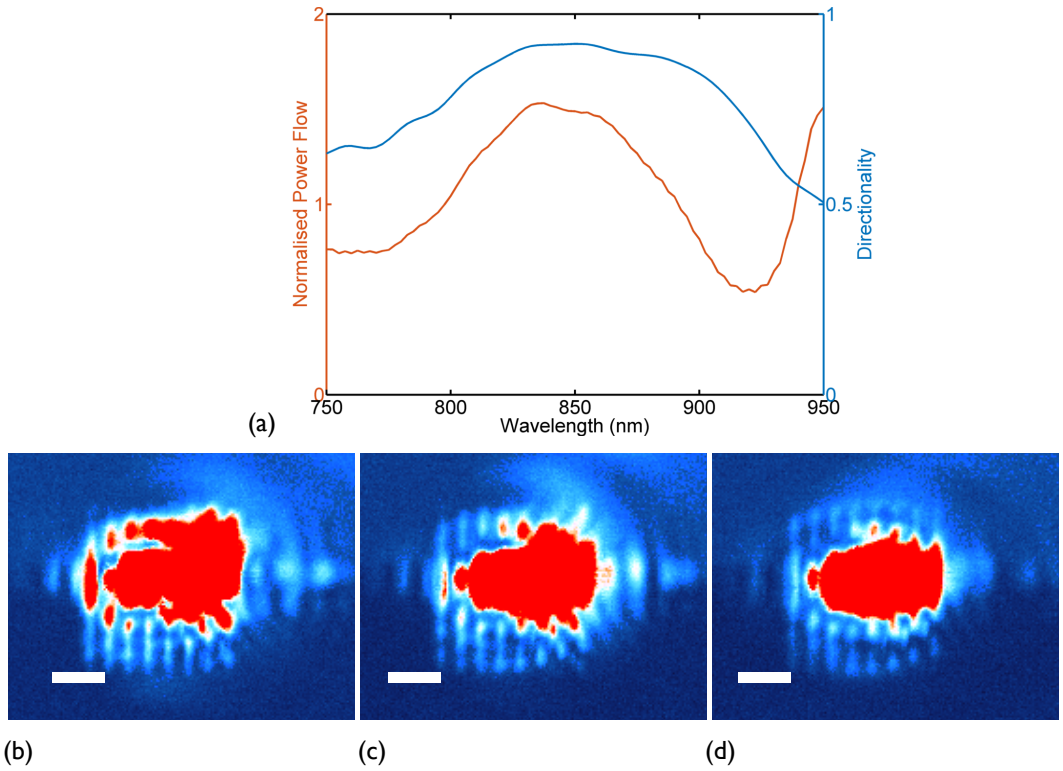

Figure 6.8 (a) Simulation: SPP power flow and directionality of a slit-groove as a function of incident wavelength. The SPP power flow is normalised with respect to an isolated slit grating, as $P_{R,N} = P_{R,Slit-Groove\ Grating} / P_{R,Slit\ Grating}$. (b-d) Experiment: Hyperspectral SNOM images of the slit-groove grating, with a linear decrease in groove depth, on an Au film for incident wavelengths: (b) 830 nm (c) 850 nm (d) 870 nm. Scale bars correspond to 2 μm.

Lastly, whilst we have only considered a constant value of d, as arrived at via optimisation, varying the periods of the slit and groove gratings independently, such as introducing a chirp, may provide further control over SPP excitation and propagation.

6.4 Summary

To conclude, we have developed, and numerically optimised, slit-groove gratings that are efficient, robust and compact. Furthermore, these couplers were successfully integrated with VCSELs, highlighting directional, on-chip SPP excitation. As the previous two chapters have covered SPP signal generation, routing and detection with VCSELs, we now turn our attention to the final category of active components, namely switches and modulators.

Chapter 7

Modulation of SPPs using Cavity Structures

Modulation of SPPs via optical and plasmonic resonances is discussed in this chapter, via structures that are amenable to integration with VCSELs. Additionally, various methods of switching are addressed, including mechanical, electro-optical and all-optical control.

7.1 Active Plasmonics

One of the foremost challenges in developing a nanoscale plasmonic platform entails achieving dynamic and real-time control of electromagnetic signals, with the term 'Active Plasmonics' often used in this regard[29,30]. In view of this, many approaches have been proposed to switch plasmonic signals, including the use of quantum dots, photochromic molecules, and electro-optic media. Modulation speed is a critical parameter for many processes, such as data transport, and thus ultrafast control of plasmonic signals is the focus of considerable research effort. Furthermore, minimising the switching energy is essential for on-chip integration of plasmonic devices and ensuring the range of applications is not unduly limited.

A promising route to achieving this goal involves employing nonlinear plasmonic structures, which offer the opportunity of manipulating signals with low switching energies, due to large local fields associated with plasmonic modes. Moreover, these excitations may respond on a short timescale of a few femtoseconds, opening up the avenue for ultrafast signal control[22]. Recent developments in this context include the work of Pohl et al., with their experiments demonstrating a 3% intensity change by using a 0.5 mJ cm^{-2} pump fluence to optically modify the permittivity of plasmonic crystals[153]. Bloch modes arising in SPPCs significantly influence the transmission, and may be actively controlled via altering the refractive index of the metal or an adjacent dielectric through optical excitation[154]. Furthermore, optically modifying the permittivity has been shown to affect the coupling of light to plasmonic modes, as Rotenberg et al. effectively demonstrated. In this case, a grating patterned structure on gold was pumped with a fluence of 50 mJ cm^{-2}, yielding a 14% change in coupling efficiency[155]. Considering smooth films, MacDonald et al.

optically modulated the plasmonic losses of an aluminium stripe waveguide to achieve a 7% differential transmission via excitation with a 10 mJ cm^{-2} fluence pump, which alters the SPP decay length via an optical Kerr process[156]. In addition to planar structures, plasmonic metamaterials have also exhibited great potential for achieving ultrafast control of signals, as their optical properties can be easily tailored. For example, an 80% change in transmission upon optical excitation of a plasmonic nanorod metamaterial with 7 mJ cm^{-2} fluence was experimentally obtained by Wurtz et al.[106], an effect arising due to increased losses and nonlocal effects. Additionally, Neira et al. presented a gold nanorod metamaterial integrated with a silicon waveguide, which allowed signal switching by controlling the hybridisation of hyperbolic modes. This was achieved via the variation of the refractive index of gold, induced upon optical excitation, thereby illustrating a modulation depth of 35% on a picosecond timescale[157].

In this context, this chapter will outline a planar, cavity-based switch that can be easily incorporated onto VCSELs. Cavity resonances are particularly suited to switching applications, as they are extremely sensitive to changes in the optical path and losses. Whilst the typical modulation speed of current VCSEL technology lies within in the GHz range, nonlinear optical effects have exhibited THz rates. Thus by introducing cavity structures onto the emission area of VCSELs we may attain additional functionality, increased efficiency, and offer ultrafast switching speeds.

7.2 Optical Cavity Switch

The general design of the switch is illustrated in Figure 7.1a, which is composed of an optical cavity with a slit placed in one of the mirrors. The underlying mechanism is based on the coherent coupling between a spectrally sharp Fabry-Perot (FP) cavity resonance and a broadband source, as represented by the slit, with the relative phase relationship between both entities providing an efficient pathway to control the emitted power. The switching process thus relies on two interfering pathways and may be rationalised by modeling the coupled system as a Fano resonator.

In the vicinity of FP resonances, the field inside the cavity takes on a well-defined phase with respect to that of the field emitted by the slit source, leading to an efficient coherent interaction that determines the power emitted by the source.

This resonant effect accounts for the asymmetric, inverted resonance in SPP power visible in Figure 7.1b as L is varied, and also the sharp phase shift. Looking at the field profiles of Figure 7.1, there is an obvious reduction in the SPP amplitude close to the fundamental optical resonance, when $L \approx \lambda/2$. Also notable is the enhanced coupling efficiency off-resonance (>1), due to the multiple reflections between the two mirrors that increases the interaction with the slit, and thus also the light-to-SPP conversion efficiency. This non-resonant effect is dependent upon the Q-factor, and consequently larger cavities provide a greater increase.

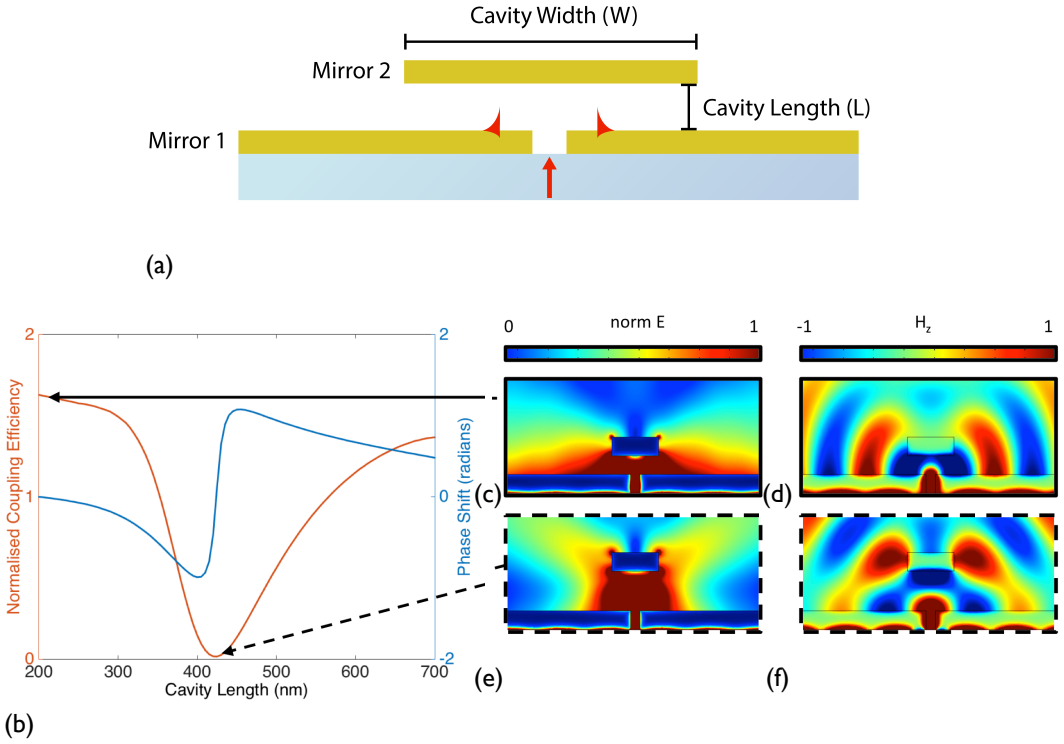

Figure 7.1 (a) General geometry of the cavity switch, composed of two metal films, with mirror 1 containing a slit and also acting as an SPP waveguide (b) Simulation: The SPP power flow on the gold film, outside the resonator, as the cavity length is varied. Additionally, this SPP power has been normalised to the cavity-less case (i.e. without mirror 2). (c-f) Field distributions in and around the cavity for off (c, d) and on (e, f) resonant conditions. (c, e) are the norm of the electric field, while (d, f) are the out of plane magnetic field. Here, W = 500 nm and the incident wavelength is 850 nm, with the gold films both 200 nm in thickness. The phase shift of SPPs on the adjacent film is calculated with respect to the initial phase for a 200 nm cavity length

The presence of the optical resonator modes thus modulates the coupling of light to SPPs, thereby permitting the present geometry to function as a plasmonic

switch. The output power of this coherent switch effectively relies on the resonant conditions under which the cavity is operating, providing the prospect for this switch to be both efficient and fast[158]. Furthermore, whilst we are primarily concerned here with controlling SPP signals, the switch also modulates scattering into free space radiation by the slit, and is thus also applicable to photonic systems.

As an experimental illustration to demonstrate this general concept, the dynamically modulated power emitted by a broadband slit embedded in a FP cavity was monitored indirectly by probing the SPP leakage radiation in Fourier space via the setup described by Figure 4.7. Hence, a slit was milled in a 50 nm thick Au film, which also served as the supporting medium for SPP modes that are excited upon illumination. In this geometry, the leakage radiation originated from SPPs propagating at the air-Au interface, and was collected in the glass substrate by an immersion oil microscope objective (x100, NA=1.42). The slit width of approximately 150 nm provided a broad transmission spectrum both in terms of spectral width and momentum spread, ensuring SPP excitation across the visible spectrum. The FP cavity was then formed between two mirrors with the SPP-supporting film acting as one mirror and a second 50 nm thick Au film, positioned a few microns away, acting as the second cavity mirror, as presented in Figure 7.2a.

The position of this second mirror was controlled by a closed-loop piezoelectric stage, which also allowed the cavity length to be mechanically varied. This geometry contained a relatively significant cavity length (on the order of microns), ensuring that the interaction between the two films was minimised for SPPs leaking into the substrate. Additionally, the presence of air inside the cavity, instead of a dielectric material, prevents unwanted intra-cavity SPP refraction and subsequent interferences as SPPs transmit from the resonator, of finite lateral width, to the Au-air interface waveguide. It is important to emphasise that the choice of using air in the cavity is guided only by the necessity of inducing leakage for SPPs created by the source. A more effective switch could otherwise take various geometries, including a cavity composed of two extended films in a homogeneous dielectric environment. Moreover, the electromagnetic feed to the cavity is also provided by the slit, which is a necessary condition to demonstrate the intended coherent effect. In practical terms this implies illuminating the cavity via transmission through the slit.

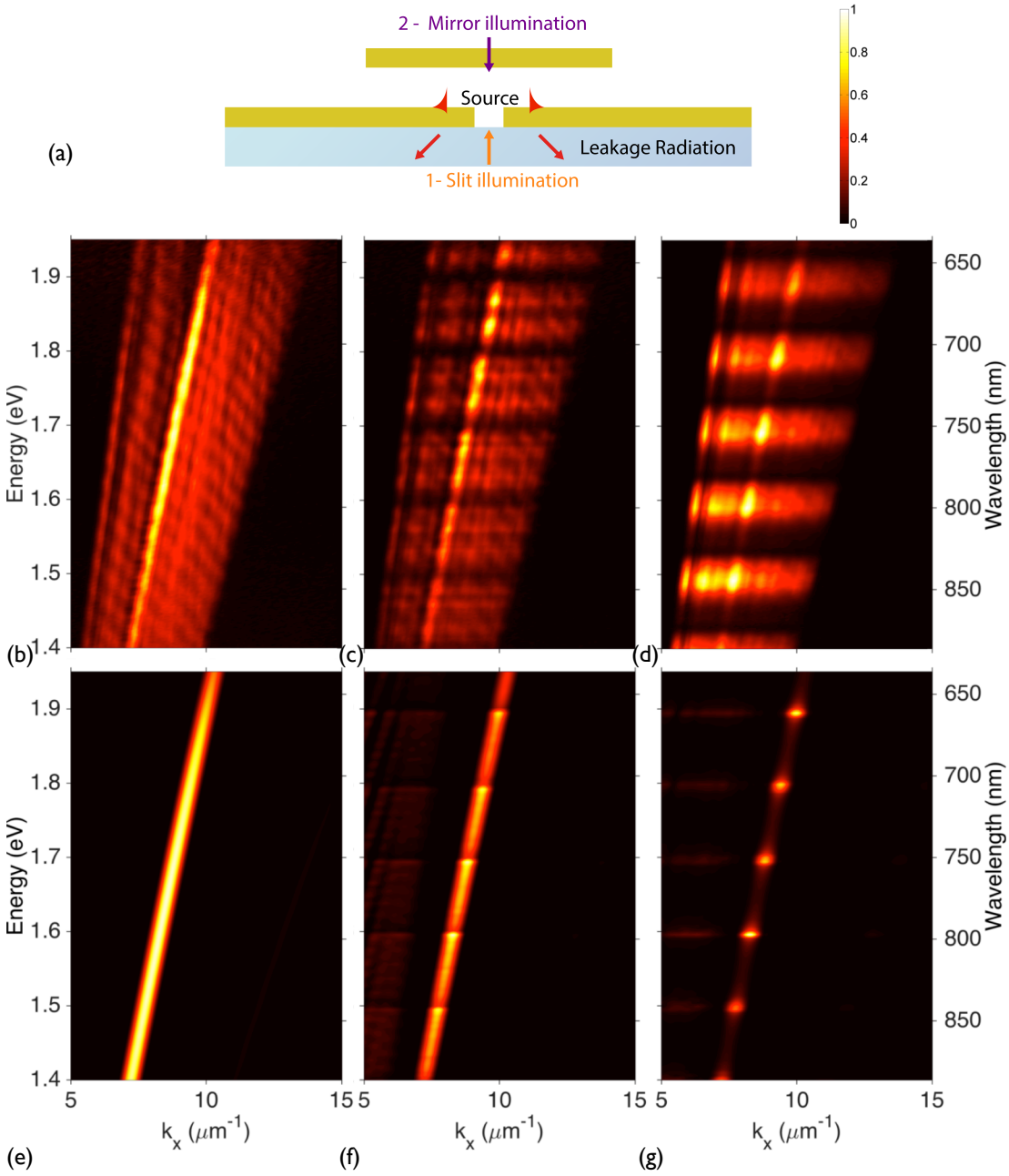

Figure 7.2 (a) Schematic of the experimental structure and (b – d) are experimental results (intensity). (b) Smooth film SPP dispersion obtained via Fourier imaging of the intensity of leakage radiation. (c) SPP dispersion obtained upon illumination of the cavity via the slit (path 1), where L is approximately 6 μm and W is on the order of 10s of microns. (d) SPP dispersion when the same cavity structure, when illuminated through the upper mirror (path 2). (e - g) are simulations of (b - d) respectively, where the FTT amplitude is plotted.

Figure 7.2b shows the SPP dispersion as obtained experimentally by imaging the back focal plane of the immersion-oil microscope objective. SPP modes are observed as maxima in the dispersion via radiation losses, as discussed in Chapter 2.

Figure 7.2c shows the same dispersion but obtained in the presence of the second mirror placed such as that the cavity length is about 6 μm. Compared to Figure 7.2b, Figure 7.2c displays marked horizontal dark bands, indicating a lack of reflected power at specific frequencies relating to FP resonances established in the cavity. Modes excited in the cavity correspond to the range of resonances with frequencies $\omega_r = r\pi c/L$ where *r* is the mode number, *L* is the wavelength sensitive cavity length, and *c* is the speed of light. The dispersion of Figure 7.2c displays 5 dispersion-less cavity modes with $\hbar\omega_r = [1.45-1.95]\,\mathrm{eV}$ corresponding to $r = [15-19]$ and equidistant by $\pi c/L \approx 0.1\,\mathrm{eV}$. These dark bands also extend through the SPP dispersion curve, signifying that the plasmonic signal is modulated, in addition to scattered free space light.

Figure 7.2c contrasts with the dispersion obtained by illuminating the cavity through the top mirror instead of through the slit, as displayed in Figure 7.2d. In this case, monitoring light transmitting through the cavity and into the substrate again reveals 5 FP resonances in the dispersion, but these are now observed as maxima in transmittance rather than minima, as in reflectance, which is expected for such a cavity. However, the main insight given by Figure 7.2d is in the presence of maxima in the SPP dispersion, where these modes are coupled to by the scattering from the slit edges. Their correspondence with cavity resonances is indicative of the enhanced field near the slit at these frequencies, and further confirms the orthonormality of SPP and cavity modes, both being able to coexist in the cavity independently. In this case, the slit can be viewed as a cavity defect, launching SPPs regardless of presence of optical resonances. Simulations equivalent to the switch geometry and illumination conditions are displayed in Figures 7e-g, and are in excellent agreement with the experimental dispersions. These numerical dispersions were obtained via Fourier analysis of the out of plane magnetic field, and again highlight the dark and bright bands corresponding to the optical cavity modes.

Combining the observations made in Figure 7.2c and Figure 7.2d allows us to formulate the assumption that light emitted by the slit coherently interacts with light trapped in the FP cavity to modulate the power emitted by the slit source. This assumption is evidently supported from an analysis of the cross-sections along the SPP dispersion in Figure 7.2c and Figure 7.2d. These are respectively shown in Figures 7.3a and 7.3b, along with a schematic of the two illumination conditions and

proposed interaction mechanisms.

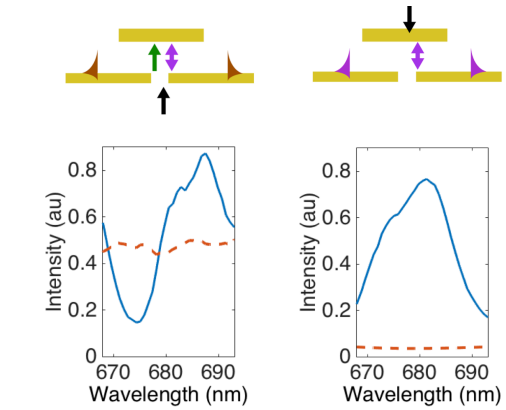

Figure 7.3 Experiment: (a) Upper panel: Schematic of slit illumination of the structure, showing interference between direct (green) and indirect, resonant (purple) scattering, which yields the plasmonic signal (brown). Lower panel: An example of the SPP asymmetric lineshape obtained with the cavity under slit illumination conditions (solid blue line), with the reference for a single film (dashed red line). (b) Upper panel: Schematic of mirror illumination of the structure, wherein indirect, resonant scattering (purple) is the dominant process. Lower panel: An example of a symmetric SPP lineshape obtained with the cavity under the mirror illumination conditions (solid blue line), with the reference for a single film (dashed red line).

It is apparent that illumination through the slit, in the presence of the FP cavity, leads to the formation of asymmetric lineshapes in the SPP dispersion at frequencies close to optical resonances. The resulting modulation in the SPP intensity exhibits both considerable enhancement and suppression compared to the cavity-less, single film geometry. A similar analysis on the cross-section corresponding to the SPP dispersion for the cavity fed through the top mirror reveals symmetric Lorentzian-like resonances in the SPP intensity. The contrasting behaviour of the two illumination conditions may be understood in the context of Fano resonances, whereby the lineshape is expressed as:

$$F(\omega) = \frac{\left[q + 2(\omega - \omega_r) \,/\, \Gamma\right]^2}{1 + \left[2(\omega - \omega_r) \,/\, \Gamma\right]^2} = \frac{(q+\varepsilon)^2}{1+\varepsilon^2} \tag{7.1}$$

where Γ is the resonance linewidth, ε is the reduced energy, ω_r is the FP resonance frequency, and the Fano parameter q describes asymmetry of the lineshape[159,160]. In contrast to Lorentzian resonances, Fano resonances may exhibit distinctly asymmetric profiles, arising due to the constructive and destructive interference between a narrow band resonance and broad spectral line or

continuum. Figure 7.4 outlines the formation of Fano resonances and examines the lineshapes attained the q parameter is varied.

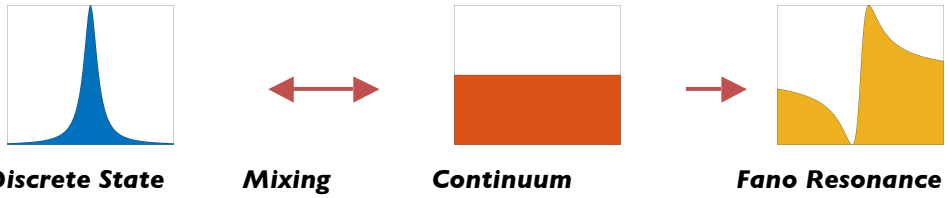

(a)

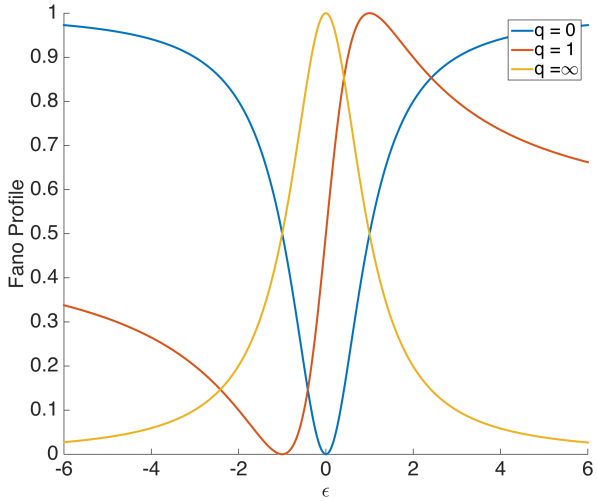

(b)

Figure 7.4 (a) Illustration of the Fano resonance as a superposition of a Lorentzian resonance with a flat background. (b) Fano lineshapes for three regimes, as represented by varying asymmetry parameter *q*. Figure adapted from reference 159.

Fano studied this type of resonance when looking at asymmetric peaks in extinction spectra, where the asymmetry was due to interference between a discrete autoionised state with a continuum. If we consider a system described by a Hamiltonian $\hat{H}$, the coupling $V_{E'} = \langle \psi_{E'} | \hat{H} | \varphi \rangle$ between a discrete state $|\varphi\rangle$ with energy $E_\varphi = \langle \varphi | \hat{H} | \varphi \rangle$ to a continuum of states $|\psi_{E'}\rangle$ which possess energies E' (a range that includes E_φ), gives rise to a perturbed state:

$$|\phi\rangle = |\varphi\rangle + p.v. \int \frac{V_{E'} |\psi_{E'}\rangle}{E_\varphi - E'} dE' \tag{7.2}$$

where p.v. refers to the principal value of the integral. The probability of transitions involving such states, normalised by the probability of transitions for non-perturbed

states, is yielded by the Fano formula, Equation 7.1[161].

As Joe et al. discuss[162], Fano interference is a universal phenomenon, as the manifestation of configuration interference is not dependent on the particular matter. Consequently, whilst Fano originally derived the formula in the context of atomic systems, we may discuss a classical analogy to gain an intuitive understanding of the interference process[162-165]. In this case, we consider two weakly coupled harmonic oscillators with losses, as described by Figure 7.5a. The first oscillator has a resonance frequency ω_b and a high damping constant γ_b, whilst the second oscillator possesses a resonance frequency ω_d and low damping constant γ_d. A harmonic external force, with amplitude $fe^{i\omega t}$, then drives the first, highly damped oscillator, leading to the equations of motion:

$$\ddot{x}_b + \gamma_b \dot{x}_b + \omega_b^2 x_b + g x_d = f e^{i\omega t} \tag{7.3}$$

$$\ddot{x}_d + \gamma_d \dot{x}_d + \omega_d^2 x_d + g x_b = 0 \tag{7.4}$$

If $g = 0$, the two oscillators move independently at their natural frequencies. Moreover, the displacements x_b and x_d are harmonic and hence $x_b = c_b e^{i\omega t}$ and $x_d = c_d e^{i\omega t}$. The amplitude of the driven, highly damped oscillator may be written as:

$$c_b = \frac{\omega_d^2 + i\gamma_d\omega - \omega^2}{\left(\omega_b^2 + i\gamma_b\omega - \omega^2\right)\left(\omega_d^2 + i\gamma_d\omega - \omega^2\right) - g^2} f \tag{7.5}$$

And the second oscillator's amplitude is given by:

$$c_d = -\frac{g}{\left(\omega_b^2 + i\gamma_b\omega - \omega^2\right)\left(\omega_d^2 + i\gamma_d\omega - \omega^2\right) - g^2} f \tag{7.6}$$

Where the phases are defined through:

$$\begin{aligned} c_b(\omega) &= \left|c_b(\omega)\right| e^{-i\phi_b(\omega)} \\ c_{d(\omega)} &= \left|c_d(\omega)\right| e^{-i\phi_d(\omega)} \end{aligned} \tag{7.7}$$

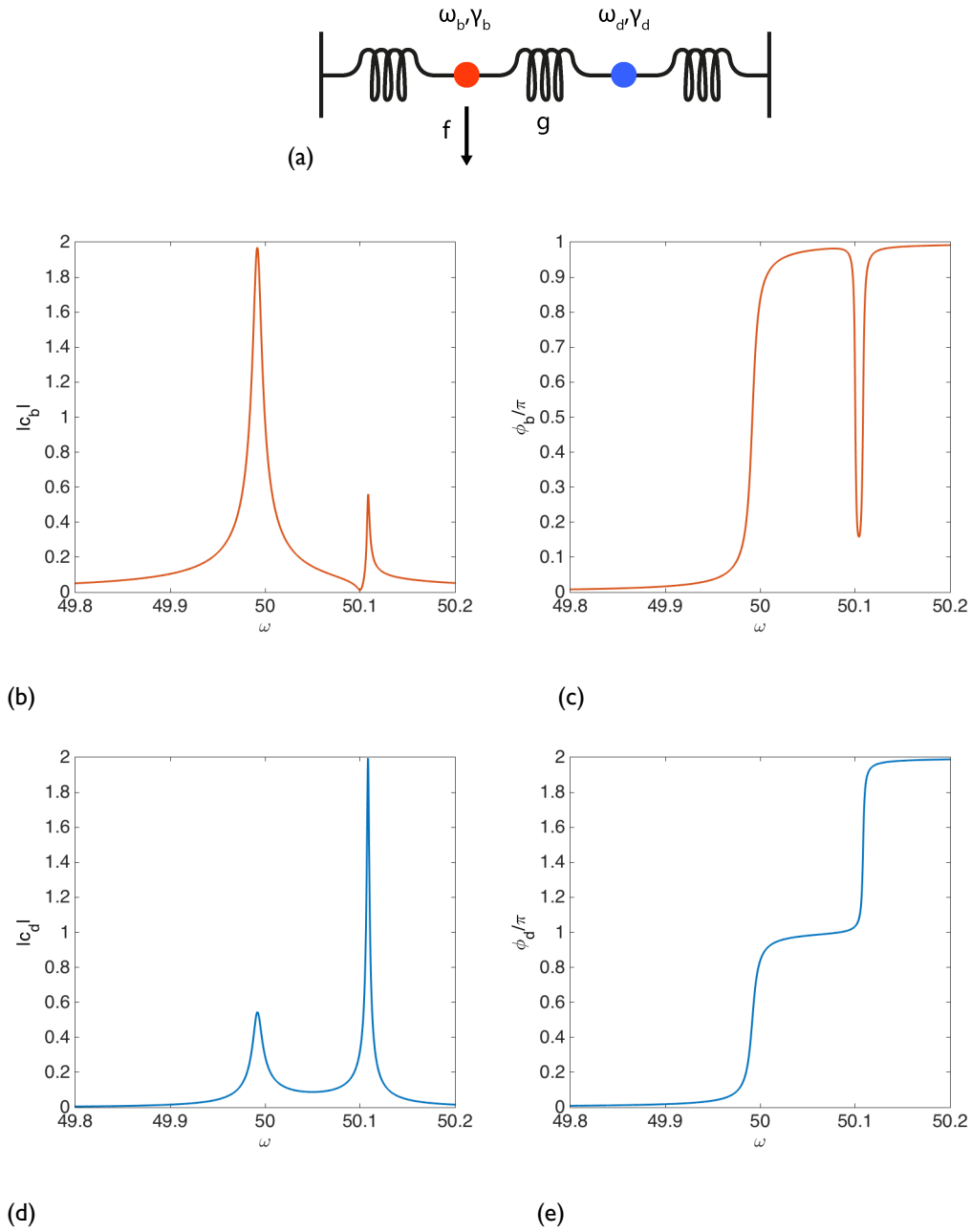

Figure 7.5 (a) Mechanical model of Fano resonances consisting of two coupled oscillators with the resonance frequencies ω_b and ω_d together with damping constants γ_b and γ_d. One oscillator (red) is driven by an external force of amplitude f where the coupling constant is g. (b) Amplitude of the forced oscillator as frequency is varied, where $\omega_b = 50, \omega_d = 50.1, g = 2, \gamma_b = 0.1, \gamma_d = 0.01$ and $f = 10$ (c) Phase behaviour of the first oscillator. (d) Amplitude of the second (blue) oscillator (e) Phase behaviour of second oscillator. Figures adapted from references 162 -163.

Equations 7.5-7.7 are plotted in Figure 7.5, where Figure 7.5b illustrates the distinctive asymmetric lineshape in the response of the forced oscillator at the frequency of the second oscillator, ω_d. The amplitude of the first oscillator becomes zero due to the destructive interference of oscillations from the external

force and the second oscillator. In other words, there are effectively two driving forces acting on the first oscillator, with these forces being out of phase and thus act to cancel each other out. Lastly, as Gallinet et al. demonstrate[163], we may use Equation 7.5 to arrive at the familiar form of the Fano equation (Equation 7.1) by considering a narrow spectral range around ω_d and taking the ratio of the amplitude of the forced oscillator with and without coupling.

From this perspective of Fano resonances, the interference process in the switching geometry occurs between the broad resonance of the slit that is driven by incident radiation, and the narrow resonances of the FP cavity. Hence, the asymmetric lineshapes in Figures 7.2c and 7.3a, resulting from slit illumination, represent the Fano regime where *q* is close to unity, as the two scattering pathways possess similar amplitudes. Conversely, the symmetric resonances of Figures 7.2d and 7.3b signify the case when *q* approaches infinity, as resonant scattering becomes the dominant process. Therefore, Figure 7.3a may be viewed as a case in which the slit emits a plasmonic signal directly, whilst also feeding a cavity that resonantly emits a signal, also via the slit. Interference between these two pathways produces a Fano lineshape, with the profile dependent on the amplitudes of direct and resonant scattering. In contrast, Figure 7.3b represents the state in which a FP cavity mode almost exclusively generates SPPs via scattering from the slit edges, producing symmetric spectral lineshapes in the vicinity of FP resonances.

Because the interference process is based on the spectral behaviour of a FP cavity, the resulting Fano lineshapes are highly sensitive to the geometry of the FP resonator, including changes in the cavity's refractive index and cavity length, making such a coherent switching system particularly suited to the design of efficient, dynamic optical functionalities. For example, reducing the cavity width (W) decreases the Q factor, which in turn leads to a smaller resonant scattering amplitude and thus alters the Fano lineshape. In the case of slit illumination, the SPP intensity may take on an inverted Lorentzian profile for sufficiently small values of W, as *q* approaches zero, which is apparent in Figures 7.1 and 7.6b. Larger, micron scale, cavities yield an asymmetric Fano lineshape (Figures 7.2c,f, 7.3a). Additionally, offsetting the upper mirror laterally, breaking the symmetry of the system, produces a directional SPP signal, as explored by Figure 7.6. In this case, the asymmetry in resonant scattering due to the mirror displacement leads to differing Fano

lineshapes for the right and left propagating SPPs. This in turn results in a degree of directionality, as shown by Figure 7.6c-f, thus offering further control over plasmonic signals.

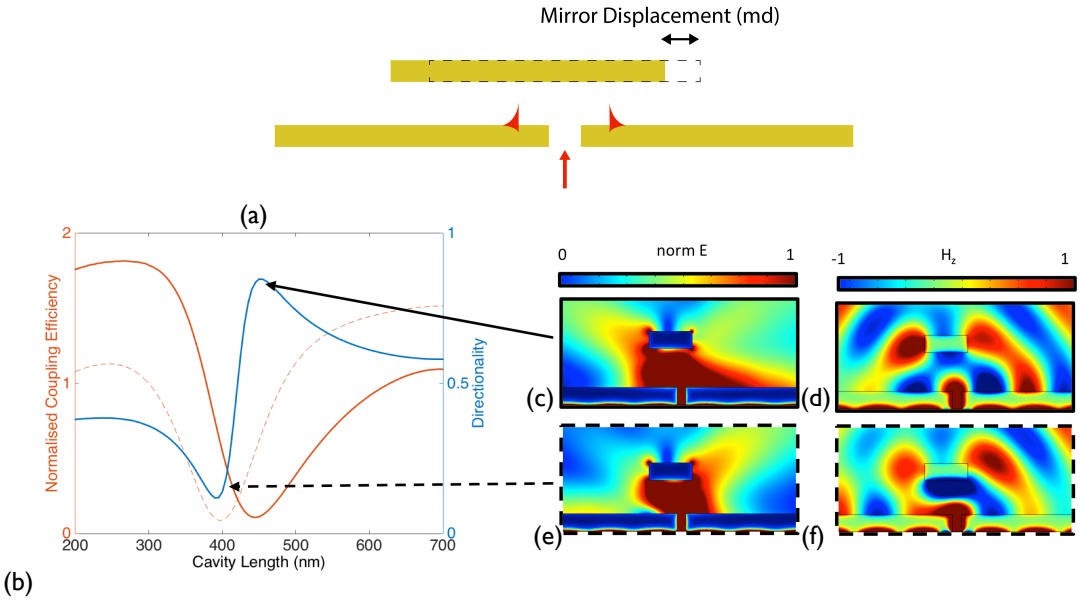

Figure 7.6 (a) Schematic showing a displacement of the upper mirror by 125 nm to the left. (b) Directional signal as the cavity length is varied. As before, the SPP power flow is normalised to the cavity-less case. When the two power flow curves intersect, the directionality goes 0.5 (symmetric excitation). (c-f) Field distributions in and around the cavity for the SPP excitation to the right (c,d) and left (e,f). The simulations have been performed for W = 500 nm and an incident wavelength of 850 nm, with the gold films both 200 nm in thickness. (c, e) are the norm of the electric field, while (d, f) are the out of plane magnetic field.

7.2.1 Mechanical Control

In order to demonstrate active coherent switching with the present geometry, two different schemes are implemented, based on either driving the cavity in and out of resonance, or on changing the resonance conditions for the cavity (i.e. the Q-factor). The first scheme may be illustrated by mechanically controlling the position of the top mirror piezoelectrically, thereby changing the cavity length and, as a result, shifting the FP resonance frequencies as $\Delta\omega_r \sim \Delta L(r\pi c)/L^2$. This allows for a fine sweep, at a set frequency, of the mutual phase relationship between source and FP cavity, leading to a controlled modulation of the power emitted by the slit source.

As previously discussed, Figures 7.3a and 7.3b show the SPP cross-sections for

slit and mirror feed conditions, whereas Figures 7.7a and 7.7b show these cross-sections as the upper mirror is displaced. A large modulation may be achieved, for instance, with a change in length $\Delta L \sim 200nm$ corresponding to a shift in the resonance frequency of $\hbar\omega_r \sim 0.06\,\mathrm{eV}$ for *r*=18, resulting in an observed 80% change in the SPP intensity at selected wavelengths across the FP resonances (Figure 7.7), equivalent to 7 dB. In this case of these experimental results, the resonances are quite broad due in part to the presence of the slit, roughness of the films and any deviation from parallelism, which all contribute to cavity losses. Moreover, narrower resonances would be beneficial to mechanical switching as the broad resonances obtained in the experiment are not especially sensitive to changes in the mirror separation (Figure 7.7), and thus may be improved upon to provide a larger change in signal for a smaller mirror displacement.

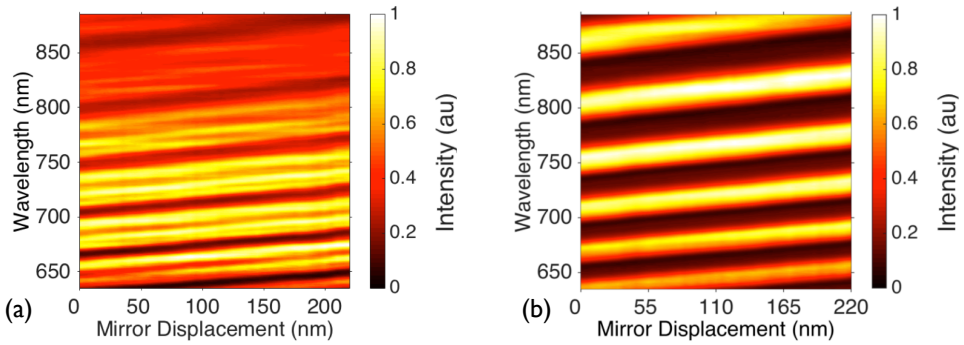

Figure 7.7 Experiment: (a) SPP intensity, under slit illumination, as the upper mirror is displaced upwards, thereby increasing the cavity length. (b) SPP intensity, under mirror illumination, as the upper mirror is displaced upwards.

7.2.2 All-Optical Control

Whilst a mechanically controlled switch provides a significant modulation depth, the corresponding modulation speeds, on the order of 10^{-6}-10^{-3}s, remain modest for displacements of a few hundred nm or more. Ultrafast switching on the picosecond timescale can be achieved all-optically, providing the applicative flexibility of using the broadband source for self-modulation, thus further illustrating the broad adaptability of the proposed switch.

In this regard, all-optical control was experimentally validated by implementing a two-colour pump-probe experiment in which a narrow 200 fs transform-limited pump pulse controls the state of the switch while a time-delayed, chirped 300 fs broadband super continuum probe pulse acts as the signal. A delay line was used to

adjust the relative arrival time of the two pulses on the sample, yielding a time step on the order of 50 fs. Figure 4.8 displays this ultrafast pump-probe spectroscopy setup, in combination with k-space imaging of the leakage radiation.

This configuration is equivalent to the slit illumination conditions described in Figure 7.2c, as the signal pulse is incident normally upon mirror containing the slit. To achieve all-optical modulation the control pulse takes the same path as the white light signal beam, both being incident on the switch from the slit side. Nonetheless, different pumping conditions can be considered, depending on which pathway(s) are to be modified. In the present geometry, the most efficient modulation scheme is to alter the sharp FP resonance, for the high-Q factor is highly sensitive to the mirrors' reflectivity. The latter property is modified by the control beam primarily through a change in the imaginary part of the Au permittivity subsequent to optical absorption via both interband and intraband electronic excitation processes[106]. The pump-induced rise in the electronic energy is then dissipated to the environment, typically with relaxation times on the order of the picosecond, as the process is mainly governed by the electron-phonon scattering rate.

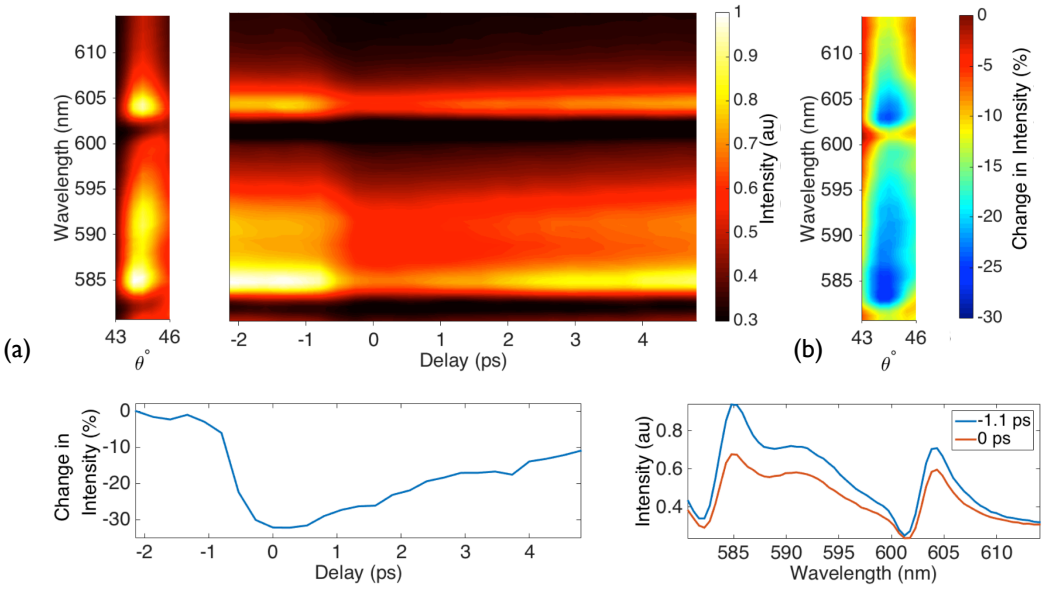

Figure 7.8 Experimental pump-probe measurements. (a) Left panel, SPP dispersion obtained from leakage radiation under slit illumination, equivalent to Figure 7.2c. Right panel, SPP intensity, taken from the dispersion, as the delay line is scanned, changing the temporal overlap between control and signal pulses. (b) Percentage change in SPP dispersion between -1.1 ps and 0 ps delay times. (c) Cross-section showing the dynamics corresponding to a resonance peak (585 nm) (d) Cross-section, displaying the Fano resonances for two delay times, illustrating the effect of the control pulse on the lineshape.

Hence, the nonlinearity of Au permits the resonance conditions for the FP cavity to be adjusted on a picosecond timescale, resulting in a change in the cavity Q-factor. This disrupts the balance in the Fano interference process, and subsequently allows the SPP power emitted by the slit source to be controlled. The left panel of Figure 7.8a shows the reflection dispersion of the signal beam for a small angular interval corresponding to the SPP leakage radiation. This dispersion was obtained with an interpulse time delay τ=-1.1 ps such that the signal beam characterises the ground state response of the source-cavity system, i.e. $\tau \rightarrow \infty$. Note that Figure 7.8 presents raw data, only normalised to the intensity of the incident signal spectrum. The two minima in the SPP dispersion, shown as extracted cross section in Figure 7.8d (τ=-1.1 ps), are the result of the resonant excitation of the FP cavity for modes $r = 17$ at λ=602 nm and $r = 18$ at λ=584 nm, again illustrating the distinctive asymmetric Fano lineshape.

The transient reflection dispersion of the signal pulse, obtained for an off-resonance control pulse with a centre wavelength of 460 nm, an incident fluence of 0.45 mJ cm^{-2}, and for the same collection angle of 45°, is plotted in the right panel of Figure 7.8a as the time delay is varied. The origin is placed at τ=0 ps, relating to the maximum temporal overlap between control and signal pulses. As is evident in Figures 7.8a and 7.8d, the general Fano lineshape is never lost throughout the transient response, with the strongest effect coming from the attenuation of the Fano peak, giving rise to a change in SPP transmission on the order of 30%. Thus the principal effect of the pump is in the modification of the resonance lineshape, where profile changes from a highly asymmetric lineshape to become more symmetric when the pulses are fully overlapped. In the Fano description, this observation can be interpreted as a modification of the ratio of direct (nonresonant) to resonant scattering between the source and the cavity, described by a Fano parameter q decreasing upon optical excitation of the cavity mirrors. Experimentally, this is the result of a variation in the FP Q factor by ΔQ~80 from Q~380 in the ground state to a Q~300 when both beams fully overlap temporally. The switching energy, leading to the observed 30% change in SPP intensity, can be estimated from the pump fluence incident on the cavity to be on the order of 350 pJ.

COMSOL simulations of the nonlinear Kerr response via the RPA confirm these

estimates, showing that this excitation energy corresponds to a peak electronic temperature increase of the lower mirror to ~1,580 K from the ground state of 300 K, subsequent to an absorption of about 65% of the incident energy, while the upper mirror reaches a maximum temperature of 620 K with an absorption of approximately 10% of the pump energy. Figures 7.8b and 7.9d clearly illustrates the change in SPP lineshape upon optical excitation of the cavity system. Figure 7.9c also highlights the modification of the Q factor, with the optical resonance becoming shifted and broadened.

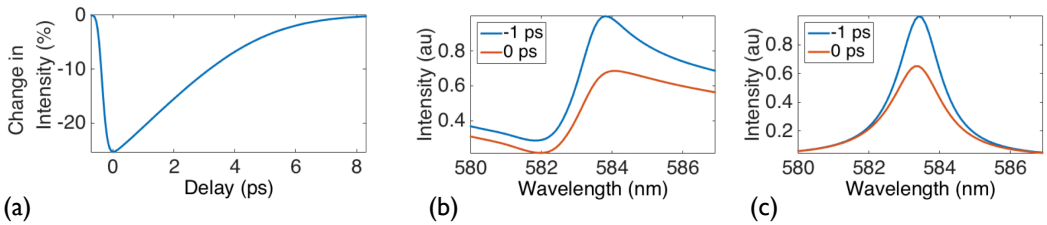

Figure 7.9 Simulation of the ultrafast response: (a) SPP intensity as the pump-probe delay is varied, equivalent to Figure 7.6c, which highlights the recovery of the SPP signal. (b) SPP lineshape for two time delays, equivalent to a portion of Figure 7.6d, illustrating the modification in the Fano asymmetry parameter. (c) Direct transmission through the cavity for two time delays, showing a change in Q factor.

The resulting maximum change in the permittivity of Au are on the order of 3% for $\Delta Re(\varepsilon_{Au})/ Re(\varepsilon_{Au})_{300K}$ while $\Delta Im(\varepsilon_{Au})/ Im(\varepsilon_{Au})_{300K}$ is on the order of 125% in the same spectral range, also confirming the predominant role of the imaginary component of the Au permittivity in the switching mechanism. The dynamics of the system, as determined experimentally from Figure 7.8c, is on the order of 1.5 ps, mainly governed by electron-phonon scattering in Au as recovered through transient nonlinear simulations of Figure 7.9, which retrieve the nonlinear dynamic response observed experimentally both qualitatively and quantitatively. However, whilst we are only considering the Kerr response in the modeling, there may be other nonlinear effects in the experiment that are not accounted for by the simulation.

7.2.3 Electro-optical Control

In addition to all-optical and mechanical modulation, there exists the opportunity for electro-optical control of the switch. For example, this may be

realised via the refractive index modulation that occurs in Indium Tin Oxide (ITO) under application of a voltage, a phenomenon that stems from an increased carrier concentration, thereby shifting the plasma frequency[166,167]. In order to employ this effect, without strongly affecting the SPPs propagating within the cavity, we numerically investigated a multilayer as the upper reflector. This consisted of two optically transparent gold films, acting as electrodes, separated by layers of ITO and HfO_2, as illustrated by Figure 7.10a.

In this geometry, a voltage of 5 V applied between the electrodes leads to a change in the SPP coupling efficiency of up to 30%. Whilst the SPP Fano resonance (Figure 7.9b) maintains the same general shape upon applying a voltage, it is blue-shifted, implying that the resonance frequency is modified. This is confirmed by the cavity transmission peak moving to a shorter wavelength (Figure 7.10c), due to the formation of an accumulation layer that in effect reduces the cavity length. Hence, whereas the cavity Q factor changes from Q~110, without an applied voltage, to Q~100 when 5 V is applied, the SPP modulation primarily stems from a reduction in the effective cavity length. This change in lineshape results in the SPP signal being enhanced of suppressed, depending on the incident probe wavelength.

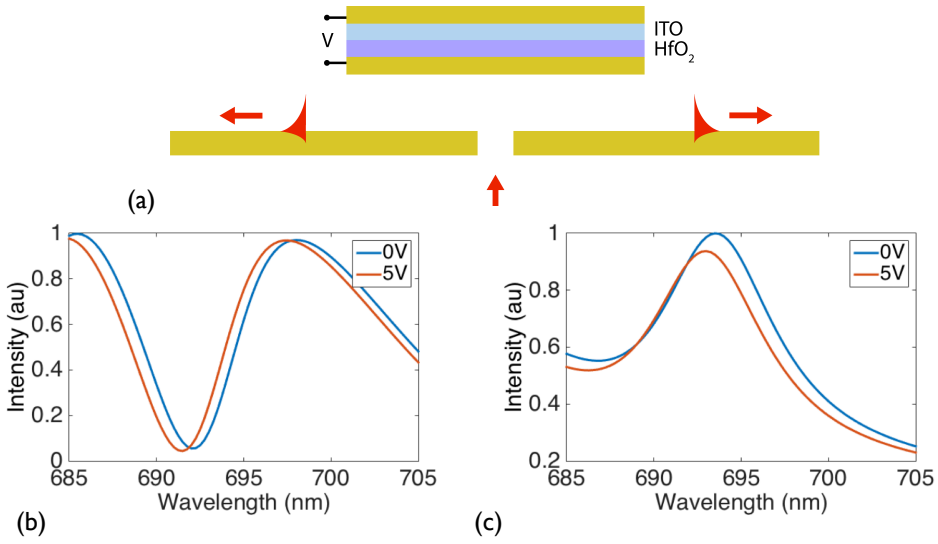

Figure 7.10 (a) Schematic of the electro-optical switching: the multilayer mirror Au/ITO/HfO_2/Au with the layers thicknesses of 50 nm, 2 nm, 2 nm and 2 nm, respectively, is positioned above the slit. The 2 nm thin Au layer acts as an electrode whilst also allowing significant optical transmission. Applying a voltage across multilayer mirror results in a reflection change at the ITO-HfO_2 interface due to charge accumulation. Simulations: (b) The SPP power flow with and without an applied voltage of 5V. (c) Direct cavity transmission through the top mirror with and without an applied voltage of 5V.

Whilst the change in transmission is not as large as that obtained using the optical and mechanical control schemes, electro-optical operation is particular beneficial for on-chip integration. Moreover, the general switching geometry presented thus far should only be regarded as serving the purpose as a proof of concept, for the general principle of a Fano-based switching mechanism can be easily extended to more functional, energy efficient and practically viable geometries. For instance, the source may be tailored to the required operation wavelength, or designed for the possibility of directional control, thereby increasing the breadth of its functionality. Furthermore, to improve the energy efficiency of this Fano-based switching device we can consider the incorporation of strong nonlinear materials, serving in conjunction with the metallic mirrors. Embedding this material in the FP cavity itself could benefit from the resonant operation of the device, providing an opportunity to design multistable outputs. Additionally, the geometry may also function via plasmonic resonances when the separation between the metal films is sufficiently small.

7.3 Plasmonic Cavity Switch

Reducing the Au film separation, such that it is on the order of 10s of nanometres, ensures that the structure supports plasmonic slot modes[168], propagating parallel to the gold films. Single interface SPPs are consequently generated at the end of the slot mode waveguide, for scattering provides the necessary shift in momentum. Also, since the cavity length is well below $\lambda/2$, no purely optical resonances are supported by the structure. The finite nature of the slot mode waveguide results in partial reflection of the slot modes at the boundaries, and correspondingly the geometry functions as a plasmonic cavity, as outlined by Figure 7.10.

In contrast with the previously discussed optical cavity, changing the Au film separation W alters the slot mode dispersion, as addressed by Figure 2.4a, whilst the length of the upper gold film defines the cavity length. Essentially the slit is coupling to resonant plasmonic modes of the system, however the Fano lineshapes, as seen in the optical cavity, are not apparent in this geometry when monitoring the SPP intensity on the adjacent smooth film. In this case, the SPP source is the

aperture at end of the slot mode waveguide, which does not concurrently feed a cavity mode, and thus no destructive interference occurs.

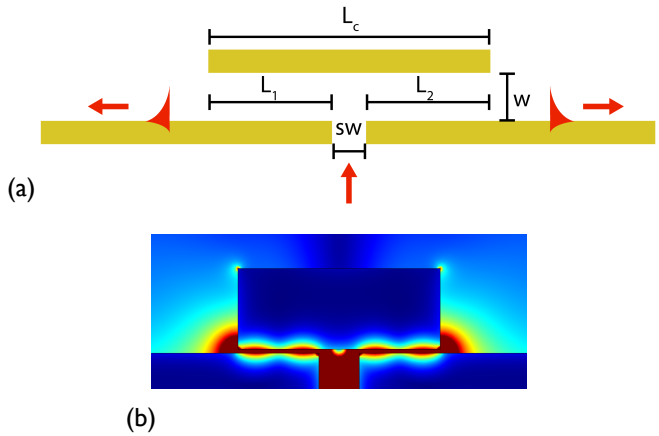

Figure 7.11 Plasmonic cavity: (a) Schematic of the structure that supports slot plasmonic mode resonances either side of the slit. (b) norm E distribution on resonance, where L_c = 500 nm, W = 10 nm, sw = 100 nm and the wavelength is 760 nm. The Au films are both 200 nm in thickness.

As before, we may mechanically control the signal via changing either W or L_1 (and thus L_2). In addition, all-optical control via altering the system losses is another possibility, in similar regard to the optical cavity switch. However, here we will examine switching scheme unique to the plasmonic cavity geometry.

7.3.1 Electro-optical switching

Electro-optically controlling the optical cavity switch in section 7.2.3 entailed modulating the reflectively of the upper mirror due the formation of an accumulation layer at the ITO-HFO_2 interface. In the case of the plasmonic cavity, we may employ the same ITO-based index modulation, not to affect the cavity reflectivity, but rather to increase the mode propagation losses, as previously numerically demonstrated by Krasavin et al. in MIM nanowire waveguides[166]. Applying a voltage results in a large increase in imaginary part of the permittivity, which is determined by electron scattering losses that are proportional to the free carrier concentration. Hence, to illustrate this switching scheme, 5 nm layers of HfO_2 and ITO respectively are sandwiched between two thick Au films, and a 4V subsequently applied across the metal layers. Marked damping of the plasmonic resonances, resulting from the increased losses, is subsequently displayed in Figure 7.12.

Essentially the effect of the ITO is to increase the losses experienced by the slot modes, extinguishing the resonances and hence smooth film SPPs are no longer efficiently excited on the adjacent Au film. Notably, the off resonance magnitude is also decreased when a voltage is applied, however this effect is not as pronounced. Looking at the resonance at 950 nm, the change in SPP transmission is approximately 90% for an applied voltage of 4V, highlighting the large modulation depth.

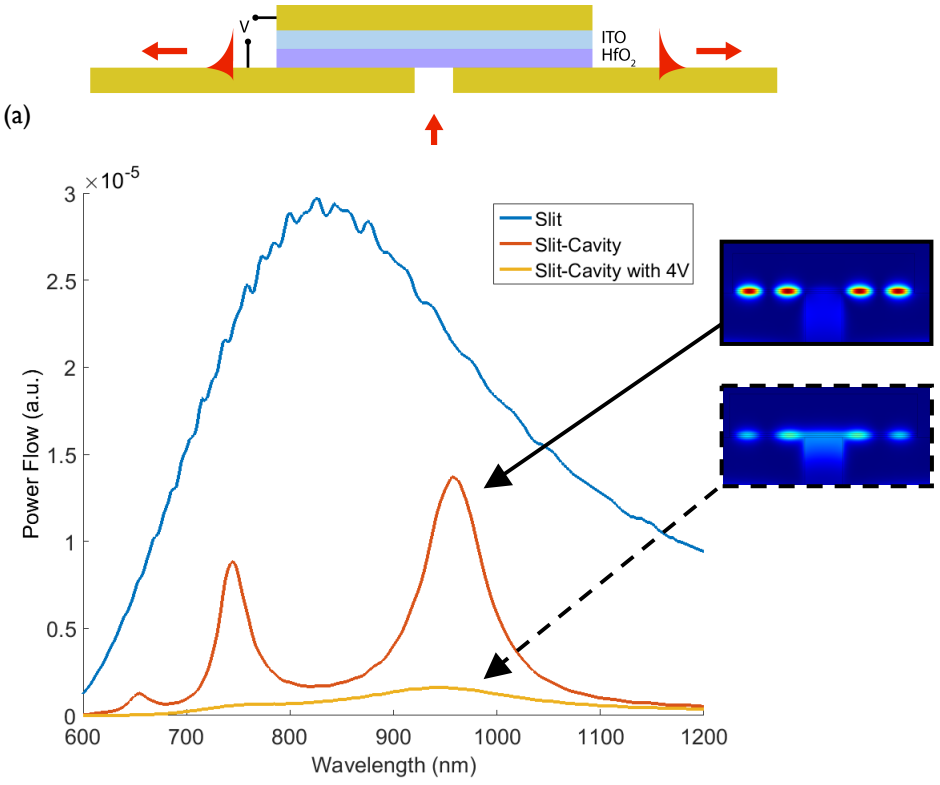

Figure 7.12 Electro-optical switching of a plasmonic cavity by incorporating an ITO-HFO_2 bilayer into the cavity: (a) Schematic of the active plasmonic cavity (b) Simulation of electro-optical control, where, L_c = 500 nm and sw = 100 nm, and the ITO and HFO_2 layers are 5 nm in thickness. The blue line corresponds to SPPs launched by an isolated slit; the red line is the SPP power flow due to the presence of the cavity, with the orange line denoting the SPP power following upon application of 4V across the cavity. Inserts show $|H_z|^2$ distribution with and without an applied voltage.

7.4 Summary

The preceding chapter has dealt with a cavity structure that may operate with optical or plasmonic resonances, depending upon its dimensions. These systems offer both high switching depths and a large degree of flexibility with regards to their implementation. The optical cavity has the benefit of effectively having a greater coupling efficiency that the case of a single film, for the off resonance

intensity is greater than the case without the second mirror. Additionally, the plasmonic cavity provides for very small switch dimensions, which is beneficial for high-density integration.

Moreover, ultrafast, all-optical switching has been experimentally demonstrated with the optical, Fano resonance based cavity. Driving the cavity near resonance provides an interference pathway of controllable phase and amplitude between the cavity and the field emitted by the source, effectively controlling the power emitted by the slit source. Mechanical operation allowed for a large SPP change in transmission, exceeding 80%, whilst a two-colour transient experiment demonstrated ultrafast power switching with a change in transmission of approximately 30% on a ps timescale using pJ level switching energies. These experimental observations were fully supported by both analytical and numerical calculations. A change in transmission of 30% corresponds to an extinction ratio Θ of ~ 1.5 dB, where $\Theta = 10\log_{10}(P_1/P_0)$ and P_1 and P_0 are the on and off states of respectively of the switch. To implement an efficient optical switch, an extinction ratio on the order of 20-30 dB is often required, and thus the presented plasmonic switch needs to be optimised.

With regards to the directionality, actively displacing the mirror laterally may prove to be cumbersome for both plasmonic and optical cavities. However, if we consider the plasmonic cavity, we may electrically isolate the two slot mode cavities either side of the slit. Hence, inserting an insulator into the upper mirror would allow a voltage to be applied independently to either side. This would enable directional control, as the right and left slot mode losses could be modified separately.

In summary, the choice of geometry for implementing the described plasmonic switch will heavily depend upon the application, and in the case of VCSELs, an electro-optically controlled plasmonic cavity is perhaps the most viable option in terms of integration.

Chapter 8

Conclusions and Outlook

8.1 Summary

This thesis essentially has two themes: manipulating plasmonic signals on VCSELs and harnessing the novel physics of cavities to actively control SPPs. With regards to the former, we have successfully developed a VCSEL that forms a platform for on-chip plasmonic components. The design was fabricated by effectively adding a few additional steps to a typical VCSEL manufacturing process, and as a result the diode is compatible with current industrial fabrication methods. Furthermore, gold stripes were incorporated into the design, permitting on-chip waveguiding of SPP signals, as illustrated by the near-field images in Chapter 5. Interferometric structures also naturally lend themselves to integration with VCSELs, as verified by the presented SEM and SNOM images, with the latter confirming the splitting and subsequent recombination of an SPP beam.

Frequency conversion of SPPs was additionally demonstrated on VCSELs, via placing a layer of PbS quantum dots on the surface of a diode. Excitation of the quantum dots by SPPs, and the ensuing relaxation, resulted in the plasmonic wavelength being red-shifted by approximately 650 nm. Moreover, effective detection of plasmonic modes was illustrated using VCSELs, as evidenced by a localised peak in the photocurrent when a plasmonic excitation structure was illuminated with the appropriate wavelength and polarisation.

In Chapter 6 we explored unidirectional excitation of SPPs from an engineering perspective, in terms optimising an asymmetric, nanoapertured structure. The resulting slit-groove gratings proved to be efficient, robust and compact, making them ideal for coupling VCSEL emission to SPPs in a unique direction.

Lastly, optical and plasmonic cavities offering modulation and switching of plasmonic signals have been both experimentally and numerically demonstrated. The planar structure of these resonators ensures they are amenable to integration with VCSELs, and consequently may provide additional functionality. What is more, the interplay between optical and plasmonic modes in these cavities makes them fascinating from a physics point of view.

In summary, the work outlined in this thesis essentially demonstrates the potential of VCSEL based plasmonic circuitry, together with illustrating compatible active plasmonic elements.

8.2 Outlook

The development of plasmonic circuitry based on VCSELs will naturally benefit from advances in VCSEL research, which is driven by a multi-million pound global industry. Furthermore, the plasmonic components addressed by this thesis may be easily expanded upon - for instance dielectric-loaded[169] and slot waveguides[170] can be conveniently incorporated. More exotic plasmonic modes may also be supported, such as non-diffracting SPPs beams[171], including airy SPPs that exhibit self-bending[172], a property that could be exploited for waveguiding around corners without the need for additional elements.

Currently the foremost application for plasmonics involves bio- and chemical sensing, which are not prohibitively hindered by the micron scale propagation length of SPPs[173]. In this context, VCSEL based plasmonic components offer an almost immediate opportunity for realising on-chip LSP and SPP based sensing. For example, two VCSELs connected together with a metal waveguide may be envisioned as a simple sensor. In this regard, the first diode generates SPPs, with the second one detecting the plasmonic signal following propagation on the waveguide. This system effectively constitutes a fully realised, on-chip circuit, and its fabrication is well within current industrial means. Additionally, Surface-Enhanced Raman Spectroscopy (SERS) is another major prospect[21] for the VCSEL platform.

Heat Assisted Magnetic Recording (HAMR) will likely prove to be a significant application for VCSELs, as previously discussed in Chapter 3. In view of this, various nanoaperture designs have been patterned onto the emission area of Au coated diodes, which thus provide high intensity, sub-diffraction limit optical spots, enhanced by plasmonic effects. These subwavelength spots afford the opportunity of locally heating a high anisotropy medium to its Curie temperature, and resultantly lowering the coericity to a value within a practical range for writing[36]. In addition, such nano-aperture diodes may also be employed in other areas including near-field probing, single-molecule fluorescence and spectroscopy[174].

With regards to plasmonic circuitry, one of the principal, immediate challenges

entails reducing the system losses (e.g. ohmic resistance). To address this, gain media may be incorporated into waveguides to offset attenuation[175], and may even offer mode amplification[176].

Looking at the active cavities discussed in Chapter 7, effective implementation of the mechanically controlled optical cavity switch may be achieved via microelectromechanical or thermal methods, as per wavelength tuning of VCSELs[67]. Electro-optical operation is also readily feasible, as the materials and voltages involved are within practical limits. Lastly, integrated, ultrafast control of the cavity switch via optical pumping may become possible with future advances in laser technology. Whilst optically pumped VCSELs, and similar external cavity diodes, may offer subpicosecond emission, they do not lend themselves to on-chip integration, and in this regard electrically pumped diodes are preferable[177].

The electro-optically operated optical cavity described in section 7.2.3 effectively contains a slot plasmon cavity as the upper mirror. Thus tuning the dimensions of both optical and plasmonic cavities, such that both resonances are sustained concurrently, may yield rich physics. It is also worth noting that the plasmonic cavity structure discussed in section 7.3 also provides the opportunity to develop meta-molecules, arising due the strong coupling between adjacent resonators. Consequently, when two plasmonic cavities are separation by a sufficiently small distance, the single, isolated resonances split into two, equivalent to symmetric and anti-symmetric orbitals. Moreover, optical and plasmonic cavities have been employed extensively to illustrate mode hybridization and nonlinear effects[178-180].

In general, the switching structures are amenable to integration with other plasmonic and photonic components, including VCSELs or Si-photonic waveguides, making them ideal candidates for active nanophotonic applications, where electro-optical, all-optical or micromechanical control signals are required. Due to the sensitivity of the cavity resonances responsible for the modulation, we anticipate that these devices will also find many guiding-wave integrated applications within areas such as biosensing, and sensors for pressure and acoustic waves.

To conclude, this thesis has drawn upon many areas of plasmonics, as any plasmonic technique and process is, in theory, compatible with the VCSEL platform.

Bibliography

1 Alberts, D. & Papp, D. The information age: an anthology on its impact and consequences. *Natl. Defense Univ. Pr.* (1997).

2 Moore, G. M. Cramming more components onto integrated circuits. *Electronics* **38**, 114-117 (1965).

3 Keyes, R. W. The impact of Moore's law. *Solid-State Circuits Society Newsletter* **11**, 25-27 (2006).

4 Zayats, A. V. & Smolyaninov, I. I. Near-field photonics: surface plasmon polaritons and localized surface plasmons. *J. Opt. A: Pure Appl. Opt.* **5**, S16-S50 (2003).

5 Abbe, E. Beiträge zur Theorie des mikroskops und der mikroskopischen wahrnehmung. *Archiv für Mikroskopische Anatomie* **9**, 413-418 (1873).

6 Rayleigh, J. W. On the theory of optical images, with special reference to the microscope. *Philos. Mag. Ser. 5* **42**, 474-482 (1896).

7 Zayats, A. & Richards, D. Nano-optics and near-field optical microscopy. *Artech House, inc.* (2009).

8 Gaponenko, S. V. Introduction to nanophotonics. *Cambridge University Press* (2010).

9 Novotny, L. & Hecht, B. Principles of nano-optics. *Cambridge University Press* (2006).

10 Ebbesen, T. W., Genet, C. & Bozhevolnyi, S. I. Surface-plasmon circuitry. *Physics Today* **44**, 44-50 (2008).

11 Editorial, Surface plasmon resurrection. *Nature Photon.* **6**, 707-707 (2012).

12 Freestone, I., Meeks, N., Sax, M. & Higgitt, C. The Lycurgus cup - A Roman nanotechnology. *Gold Bull.* **40**, 270-277 (2007).

13 Mie, G. Beiträge zur Optik trüber medien, speziell kolloidaler metallösungen. *Ann. Phys.* **330**, 377-445 (1908).

14 Wood, R. W. On a remarkable case of uneven distribution of light in a diffraction grating spectrum. *Philos. Mag.* **4**, 396-402 (1902).

15 Sommerfeld, A. Über die Fortpflanzung elektrodynamischer wellen an längs eines drahtes. *Ann. Phys.* **67**, 233–290 (1899).

16 Zenneck, J. Über die Fortpflanzung ebener elektromagnetischer wellen längs

einer ebenen Leiterfläche und ihre beziehung zur drahtlosen telegraphie. *Ann. Phys.* **328**, 846–866 (1907).

17 Kretschmann, E. & Raether, H. Radiative decay of non radiative surface plasmons excited by light. *Z. Naturforsch.* **23** 2135-2136 (1968).

18 Ritchie, R. H. Plasma losses by fast electrons in thin films. *Phys. Rev.* **106**, 874-881 (1957).

19 Ebbesen, T. W., Lezec, H. J., Ghaemi, H. F., Thio, T. & Wolff, P. A. Extraordinary optical transmission through sub-wavelength hole arrays. *Nature* **391**, 667-669 (1998).

20 Feng, J., Siu, V. S., Roelke, A., Mehta, V., Rhieu, S. Y., Palmore, G. T. R. & Pacifici, D. Nanoscale plasmonic interferometers for multispectral, high-throughput biochemical sensing. *Nano Lett.* **12**, 602-609 (2012).

21 Le Ru, E. & Etchegoin, P. Principles of surface-enhanced Raman spectroscopy. *Elsevier* (2008).

22 Kauranen, M. & Zayats, A. V. Nonlinear plasmonics. *Nature Photon.* **6**, 737-748, (2012).

23 Heber, J. Plasmonics: Surfing the wave. *Nature* **461**, 720-722, (2009).

24 Mansuripur, M., Zakharian, A. R., Lesuffleur, A., Oh, S.-H., Jones, R. J., Lindquist, N. C., Im, H., Kobyakov, A. & Moloney, J. V. Plasmonic nano-structures for optical data storage. *Opt. Express* **17**, 14001-14014 (2009).

25 Challener, W. A., Peng, C., Itagi, A. V., Karns, D., Peng, W., Peng, Y., Yang, X., Zhu, X., Gokemeijer, N. J., Hsia, Y. T., Ju, G., Rottmayer, R. E., Seigler, M. A. & Gage, E. C. Heat-assisted magnetic recording by a near-field transducer with efficient optical energy transfer. *Nature Photon.* **3**, 220-224 (2009).

26 Pillai, S., Catchpole, K. R., Trupke, T. & Green, M. A. Surface plasmon enhanced silicon solar cells. *J. Appl. Phys.* **101**, 093105 (2007).

27 Neumann, O., Urban, A. S., Day, J., Lal, S., Nordlander, P. & Halas, N. J. Solar vapor generation enabled by nanoparticles. *ACS Nano* **7**, 42-49, (2013).

28 Sorger, V. J., Oulton, R. F., Ma, R. M. & Zhang, X. Toward integrated plasmonic circuits. *MRS Bulletin* **37**, 728-738 (2012).

29 Zayats, A. V. & Maier, S. A. Active plasmonics and tuneable plasmonic metamaterials. *Wiley* (2013).

30 MacDonald, K. F. & Zheludev, N. I. Active plasmonics: current status. *Laser Photon. Rev.* **4**, 562-567 (2009).

31 Assefa, S., Shank, S., Green, W., Khater, M., Kiewra, E., Reinholm, C., Kamlapurkar, S., Rylyakov, A., Schow, C., Horst, F., Pan, H., Topuria, T., Rice, P., Gill, D. M., Rosenberg, J., Barwicz, T., Yang, M., Proesel, J., Hofrichter, J., Offrein, B., Gu, X., Haensch, W., Ellis-Monaghan J. & Vlasov, Y. A 90nm CMOS integrated nano-photonics technology for 25Gbps WDM optical communications applications. *2012 IEEE International Electron Devices Meeting (IEDM)* (2012).

32 Barnes, W. L., Dereux, A. & Ebbesen, T. W. Surface plasmon subwavelength optics. *Nature* **424**, 824-830 (2003).

33 Ozbay, E. Plasmonics: Merging photonics and electronics at nanoscale dimensions. *Science* **311**, 189-193 (2006).

34 Brongersma, M. L. & Shalaev, V. M. Applied physics. The case for plasmonics. *Science* **328**, 440-441 (2010).

35 Iga, K. Vertical-cavity surface-emitting laser: Its conception and evolution. *Japan. J. Appl. Phys.* **47**, 1-10 (2008).

36 Michalzik, R. VCSELs: Fundamentals, technology and applications of vertical-cavity surface-emitting lasers. *Spinger-Verlag* (2013).

37 BCC Research, Available: http://www.bccresearch.com/pressroom/pho/global-market-vertical-cavity-surface-emitting-lasers-reach-nearly-$2.1-billion-2018

38 Li, H., Wolf, P., Moser, P., Larisch, G., Lott, J. A. & Bimberg, D. Vertical-cavity surface-emitting lasers for optical interconnects. *SPIE Newsroom* (2014).

39 Bringer, C., Bardinal, V., Fontaine, C., Averseng, L., Camps, T., Dubreuil, P. & Munoz-Yague, A. Dual-purpose single-cavity oxide-confined VCSEL-photodetector. *VCSELs and Optical Interconnects* **4942**, 355-362 (2003).

40 UN General Assembly 68th Session proclaimed 2015 as the International Year of Light and Light-based Technologies, Available: www.light2015.org/Home/About.

41 Rider, A. E., Ostrikov, K. & Furman, S. A. Plasmas meet plasmonics Everything old is new again. *EPJD* **66**, 226 (2012).

42 Maradudin, A., Sambles J. & Barnes, W. L. Modern plasmonics. *Elsevier* (2014).

43 Raether, H. Surface plasmons on smooth and rough surfaces and on gratings. *Spinger-Verlag* (1988).

44 Maier, S. A. Plasmonics: fundamentals and applications. *Springer* (2007).

45 Barnes, W. L. Surface plasmon–polariton length scales: a route to sub-wavelength optics. *J. Optics A-Pure Appl. Opt.* **8**, S87-S93 (2006).

46 Johnson, P. B. & Christy, R. W. Optical constants of the noble metals. *Phys. Rev. B* **6**, 4370-4379 (1972).

47 West, P. R., Ishii, S., Naik, G. V., Emani, N. K., Shalaev, V. M. & Boltasseva, A. Searching for better plasmonic materials. *Laser Photon. Rev.* **4**, 795–808 (2010).

48 Corti, C. & Holliday, R. Gold: Science and applications. *CRC Press* (2009).

49 Vu, C. Made in IBM Labs: Holey optochip first to transfer one trillion bits of information per second using the power of light. *IBM press release* (2012) https://www-03.ibm.com/press/us/en/pressrelease/37095.wss

50 Simonite, T. Intel's laser chips could make data centers run better. *MIT Technology Review* (2013). Available: https://www.technologyreview.com/s/518941/intels-laser-chips-could-make-data-centers-run-better/

51 Shahbazyan, T. V. & Stockman, M. I. Plasmonics: Theory and applications. *Springer* (2013).

52 Dionne, J. A., Sweatlock, L. A., Sheldon, M. T., Alivisatos, A. P. & Atwater, H. A., Silicon-based plasmonics for on-chip photonics. *IEEE J. Sel. Top. Quantum Electron.* **16,** 295-306 (2010).

53 Naik, G. V., Schroeder, J. L., Ni, X., Kildishev, A. V., Sands, T. D. & Boltasseva, A. Titanium nitride as a plasmonic material for visible and near-infrared wavelengths. *Opt. Mater. Express* **2**, 478 (2012).

54 Bozhevolnyi, S. I. & Sondergaard, T. General properties of slow-plasmon resonant nanostructures: nano-antennas and resonators. *Opt. Express* **15**, 10869-10877 (2007).

55 Kurokawa, Y. & Miyazaki, H. T. Metal-insulator-metal plasmon nanocavities: Analysis of optical properties. *Phys. Rev. B* **75**, 035411 (2007).

56 Bozhevolnyi, S. I. Effective-index modeling of channel plasmon polaritons. *Opt. Express* **14**, 9467-9476 (2006).

57 Zayats, A. V., Smolyaninov, I. I. & Maradudin, A. A. Nano-optics of surface plasmon polaritons. *Phys. Rep.* **408**, 131-314 (2005).

58 Maier, S. A. & Atwater, H. A. Plasmonics: Localization and guiding of electromagnetic energy in metal/dielectric structures. *J. Appl. Phys.* **98**, 011101 (2005).

59 Sanchez-Gil, J. A. & Maradudin, A. A. Near-field and far-field scattering of surface plasmon polaritons by one-dimensional surface defects. *Phys. Rev. B* **60**, 8359-8367 (1999).

60 Mikhailov, V., Wurtz, G. A., Elliott, J., Bayvel, P. & Zayats, A. V. Dispersing light with surface plasmon polaritonic crystals. *Phys. Rev. Lett.* **99**, 083901 (2007).

61 Barnes, W. L., Preist, T. W., Kitson, S. C. & Sambles, J. R. Physical origin of photonic energy gaps in the propagation of surface plasmons on gratings. *Phys. Rev. B Condens. Matter* **54**, 6227-6244 (1996).

62 Bharadwaj, P., Bouhelier, A. & Novotny, L. Electrical excitation of surface plasmons. *Phys. Rev. Lett.* **106**, 226802 (2011).

63 McCarron, R., Dickson, W., Krasavin, A. V., Wurtz, G. A. & Zayats, A. V. Dipolar emission in trench metal–insulator–metal waveguides for short-scale plasmonic communications: numerical optimization. *J. Opt.* **16**, 114006 (2014).

64 Barnes, W. L. Fluorescence near interfaces: the role of photonic mode density. *J. Mod. Opt.* **45**, 661-699 (1998).

65 Towe, E., Leheny, R. F. & Yang, A. A historical perspective of the development of the vertical-cavity surface-emitting laser. *IEEE J. Sel. Top. Quantum Electron.* **6**, 1458-1464 (2000).

66 Mönch, H. & Derra, G. High Power VCSEL Systems. *Laser Technik Journal* **2**, 43-47 (2014).

67 Gierl, C., Gruendl, T., Debernardi, P., Zogal, K., Grasse, C., Davani, H. A., Bohm, G., Jatta, S., Kuppers, F., Meißner, P. & Amann, M.-C. Surface micromachined tunable 1.55 mum-VCSEL with 102 nm continuous single-mode tuning. *Opt. Express* **19**, 17336-17343 (2011).

68 Wang, Z., Zhang, B. & Deng, H. Dispersion engineering for vertical microcavities using subwavelength gratings. *Phys. Rev. Lett.* **114** (2015).

69 Grabherr, M., Intemann, S., Wabra, S., Gerlach, P., Riedl, M. & King, R. 25 Gbps and beyond: VCSEL development at Philips. *Proc. SPIE* **8639**, 86390J-1 (2013).

70 Shinada, S., Hashizume, J. & Koyama, F. Surface plasmon resonance on microaperture vertical-cavity surface-emitting laser with metal grating. *Appl. Phys. Lett.* **83**, 836 (2003).

71 Rao, Z., Vo, S. & Harris, J. S. A review of progress on nano-aperture VCSEL. *Chin. Opt. Lett.* **6**, 748-754 (2008).

72 Stockman, M. I. Spasers explained. *Nature Photon.* **2**, 327-329 (2008).

73 Wang, L., Li, T., Li, L., Xia, W., Xu, X. G. & Zhu, S. N. Electrically generated unidirectional surface plasmon source. *Opt. Express* **20**, 8710-8717 (2012).

74 Noginov, M. A., Zhu, G., Belgrave, A. M., Bakker, R., Shalaev, V. M., Narimanov, E. E., Stout, S., Herz, E., Suteewong, T. & Wiesner, U. Demonstration of a spaser-based nanolaser. *Nature* **460**, 1110-1112 (2009).

75 Khurgin, J. B. & Sun, G. Comparative analysis of spasers, vertical-cavity surface-emitting lasers and surface-plasmon-emitting diodes. *Nature Photon.* **8**, 468-473 (2014).

76 Zhu, X., Zhang, J., Xu, J. & Yu, D. Vertical plasmonic resonant nanocavities. *Nano Lett.* **11**, 1117-1121 (2011).

77 Chow, W. W., Choquette, K. D., Crawford, M. H., Lear, K. L. & Hadley, G. R. Design, fabrication, and performance of infrared and visible vertical-cavity surface-emitting lasers. *IEEE J. Quant. Electron.* **33**, 1810-1824 (1997).

78 Koyama, F. Recent advances of VCSEL photonics. *J. Lightwave Technol.* **24**, 4502-4513 (2006).

79 Volkert, C. A. & Minor, A. M. Focused ion beam microscopy and micromachining. *MRS Bulletin* **32**, 389-399 (2007).

80 Kollmann, H., Piao, X., Esmann, M., Becker, S. F., Hou, D., Huynh, C., Kautschor, L. O., Bosker, G., Vieker, H., Beyer, A., Golzhauser, A., Park, N., Vogelgesang, R., Silies, M. & Lienau, C. Toward plasmonics with nanometer precision: nonlinear optics of helium-ion milled gold nanoantennas. *Nano Lett.* **14**, 4778-4784 (2014).

81 Novotny, L. & Stranick, S. J. Near-field optical microscopy and spectroscopy with pointed probes. *Annu. Rev. Phys. Chem.* **57**, 303-331 (2006).

82 Betzig, E. & Trautman, J. K. Near-field optics: microscopy, spectroscopy, and surface modification beyond the diffraction limit. *Science* **257**, 189-195 (1992).

83 Synge, E. H. An application of piezoelectricity to microscopy. *Philos. Mag.* **13**, 297 (1932).

84 Synge, E. H. A suggested method for extending microscopic resolution into the ultra-microscopic region. *Philos. Mag.* **6**, 356-362 (1928).

85 Pohl, D. W., Denk, W. & Lanz, M. Optical stethoscopy: Image recording with resolution λ/20. *Appl. Phys. Lett.* **44**, 651-653 (1984).

86 Lewis, A., Isaacson, M., Harootunian, A. & Muray, A. Development of a 500-A spatial-resolution light-microscope. *Ultramicroscopy* **13**, 227-231 (1984).

87 Rotenberg, N. & Kuipers, L. Mapping nanoscale light fields. *Nature Photon.* **8**, 919-926 (2014).

88 Bouillard, J. S., Vilain, S., Dickson, W. & Zayats, A. V. Hyperspectral imaging with scanning near-field optical microscopy: applications in plasmonics. *Opt. Express* **18**, 16513-16519 (2010).

89 Bouillard, J. S., Dickson, W., Wurtz, G. A. & Zayats, A. V. Near-field hyperspectral optical imaging. *ChemPhysChem* **15**, 619-629 (2014).

90 Porto, J. A., Carminati, R. & Greffet, J. J. Theory of electromagnetic field imaging and spectroscopy in scanning near-field optical microscopy. *J. Appl. Phys.* **88**, 4845-4850 (2000).

91 Gersen, H., Karle, T. J., Engelen, R. J., Bogaerts, W., Korterik, J. P., van Hulst, N. F., Krauss, T. F. & Kuipers, L. Direct observation of Bloch harmonics and negative phase velocity in photonic crystal waveguides. *Phys. Rev. Lett.* **94**, 123901 (2005).

92 le Feber, B., Rotenberg, N., Beggs, D. M. & Kuipers, L. Simultaneous measurement of nanoscale electric and magnetic optical fields. *Nature Photon.* **8**, 43-46 (2013).

93 Bouhelier, A. & Wiederrecht, G. P. Excitation of broadband surface plasmon polaritons: Plasmonic continuum spectroscopy. *Phys. Rev. B* **71**, 195406(2005).

94 Ye, F., Merlo, J. M., Burns, M. J. & Naughton, M. J. Optical and electrical mappings of surface plasmon cavity modes. *Nanophotonics* **3**, 33-49 (2014).

95 Studying the interaction of short pulsed lasers with matter, Available: https://jila.colorado.edu/cundiff/research/spectroscopy.

96 COMSOL Multiphysics User's Guide. *Version 4.3a*.

97 Finite Element Analysis (FEA) Software, Available: https://www.comsol.com/multiphysics/fea-software

98 Bhavikatti, S. S. Finite element analysis. *New Age International Pvt Ltd Publishers* (2010).

99 Shannon, C. E. Communication in the presence of noise. *Proc. IEEE* **86**, 447-457 (1998).

100 Farhang, A. & Martin, O. J. Plasmon delocalization onset in finite sized nanostructures. *Opt. Express* **19**, 11387-11396 (2011).

101 Paret, M. A simple guide to using monte carlo simulation to estimate pi. Available: http://blog.minitab.com/blog/michelle-paret/a-simple-guide-to-using-monte-carlo-simulation-to-estimate-pi-v2

102 Optimization module, User's Guide, COMSOL 4.3a

103 Boyd, R. W. Nonlinear Optics. *Boston: Academic Press* (2008).

104 Zheludev, N. I. Nonlinear optics on the nanoscale. *Contemp. Phys.* **43**, 365-377 (2002).

105 Bigot, J. Y., Merle, J. Y., Cregut, O. & Daunois, A. Electron Dynamics in Copper Metallic Nanoparticles Probed with Femtosecond Optical Pulses. *Phys. Rev. Lett.* **75**, 4702-4705 (1995).

106 Wurtz, G. A., Pollard, R., Hendren, W., Wiederrecht, G. P., Gosztola, D. J., Podolskiy, V. A., Zayats, A. V. Designed ultrafast optical nonlinearity in a plasmonic nanorod metamaterial enhanced by nonlocality. *Nature Nanotech.* **6**, 106-110 (2011).

107 Hohlfeld, J., Wellershoff, S. S., Gudde, J., Conrad, U., Jahnke, V. & Matthias, E. Electron and lattice dynamics following optical excitation of metals. *J. Chem. Phys.* **251**, 237-258 (2000).

108 Neira, A. D., Olivier, N., Nasir, M. E., Dickson, W., Wurtz, G. A. & Zayats, A. V. Eliminating material constraints for nonlinearity with plasmonic metamaterials. *Nat. Commun.* **6**, 7757 (2015).

109 Pines, D. & Nozières, P. Quantum Theory of Liquids. *W.A. Benjamin* (1966)

110 Louis, C. & Pluchery, O. Gold Nanoparticles for Physics, Chemistry and Biology. *Imperial College Press* (2012).

111 Stalmashonak, A., Seifert, G. & Abdolvand, A. Ultra-Short Pulsed Laser Engineered Metal-Glass Nanocomposites. *Springer* (2013).

112 Corbett, B., Lamy, J.-M., Justice, J. & Lévêque, G. Manipulation of surface plasmons on a vertical cavity surface emitting laser platform. *Proc. SPIE* **7712**, 771213, (2010).

113 Porta, R. A., Justice, J., Lévêque, G. & Corbett, B. Vertical-Cavity Surface-Emitting Lasers With Integrated Excitation of Surface Plasmon Polariton Modes. *IEEE Photon. Technol. Lett.* **21**, 221-223 (2009).

114 Lamy, J. M., Justice, J., Lévêque, G. & Corbett, B. Monolithic excitation and manipulation of surface plasmon polaritons on a vertical cavity surface emitting laser. *Appl. Phys. A* **103**, 665–667 (2011).

115 Shalaev, V. M. & Kawata, S. Nanophotonics with Surface Plasmons. *Elsevier* (2007).

116 Zia, R., Schuller, J. A. & Brongersma, M. L. Near-field characterization of guided polariton propagation and cutoff in surface plasmon waveguides. *Phys. Rev. B* **74**, 165415 (2006).

117 Zia, R., Selker, M. D. & Brongersma, M. L. Leaky and bound modes of surface plasmon waveguides. *Phys. Rev. B* **71**, 165431 (2005).

118 Gao, Y., Gan, Q., Xin, Z., Cheng, X. & Bartoli, F. J. Plasmonic Mach-Zehnder interferometer for ultrasensitive on-chip biosensing. *ACS Nano* **5**, 9836-9844, (2011).

119 Hakala, T. K., Toppari, J. J., Pettersson, M., Kuzyk, A., Tikkanen, H., Kunttu, H. & Törmä, P. Frequency conversion of propagating surface plasmon polaritons by organic molecules. *Appl. Phys. Lett.* **93**, 123307 (2008).

120 DeCusatis, C. & Kaminow, I. The Optical Communications Reference *Academic Press Inc* (2009).

121 Akbari, A., Tait, R. N. & Berini, P. Surface plasmon waveguide Schottky detector. *Opt. Express* **18**, 8505-8514 (2010).

122 Heeres, R. W., Dorenbos, S. N., Koene, B., Solomon, G. S., Kouwenhoven, L. P. & Zwiller, V. On-chip single plasmon detection. *Nano Lett.* **10**, 661-664

(2010).

123 Falk, A. L., Koppens, F. H. L., Yu, C. L., Kang, K. de Leon Snapp, N., Akimov, A. V., Jo, M.-H., Lukin, M. D. & Park, H. Near-field electrical detection of optical plasmons and single-plasmon sources. *Nature Phys.* **5**, 475-479 (2009).

124 Ditlbacher, H., Aussenegg, F. R., Krenn, J. R., Lamprecht, B., Jakopic, G. & Leising, G. Organic diodes as monolithically integrated surface plasmon polariton detectors. *Appl. Phys. Lett.* **89**, 161101 (2006).

125 Dragas, M., White, I. H., Penty, R. V., Rorison, J., Heard, P. J. & Parry, G. Dual-Purpose VCSELs for Short-Haul Bidirectional Communication Links. *IEEE Photon. Technol. Lett.* **11**, 1548-1550 (1999).

126 Knodl, T., Choy, H. K. H., Pan, J. L., King, R., Jäger, R., Lullo, G., Ahadian, J. F., Ram, R. J., Fonstad, Jr. C. G. & Ebeling, K. J. RCE Photodetectors Based on VCSEL Structures. *IEEE Photon. Technol. Lett.,* **11**, 1289-1291 (1999).

127 Sonnefraud, Y., Kerman, S., Di Martino, G., Lei, D. Y. & Maier, S. A. Directional excitation of surface plasmon polaritons via nanoslits under varied incidence observed using leakage radiation microscopy. *Opt. express* **20**, 4893-4902 (2012).

128 Li, X., Tan, Q., Bai, B. & Jin, G. Experimental demonstration of tunable directional excitation of surface plasmon polaritons with a subwavelength metallic double slit. *Appl. Phys. Lett.* **98**, 251109 (2011).

129 Lu, J., Petre, C., Yablonovitch, E. & Conway, J. Numerical optimization of a grating coupler for the efficient excitation of surface plasmons at an Ag-SiO2 interface. *J. Opt. Soc. Am. B* **24**, 2268-2272 (2007).

130 Chen, J., Li, Z., Yue, S. & Gong, Q. Efficient unidirectional generation of surface plasmon polaritons with asymmetric single-nanoslit. *Appl. Phys. Lett.* **97**, 041113 (2010).

131 Huang, X. & Brongersma, M. L. Compact aperiodic metallic groove arrays for unidirectional launching of surface plasmons. *Nano Lett.* **13**, 5420-5424 (2013).

132 Liao, H., Li, Z., Chen, J., Zhang, X., Yue, S. & Gong, Q. A submicron broadband surface-plasmon-polariton unidirectional coupler. *Sci. Rep.* **3**, 1918 (2013).

133 Lu, C., Hu, X., Yang, H. & Gong, Q. Ultrawide-Band Unidirectional Surface

Plasmon Polariton Launchers. *Adv. Opt. Materials* **1**, 792-797, (2013).

134 Baron, A., Devaux, E., Rodier, J. C., Hugonin, J. P., Rousseau, E., Genet, C., Ebbesen, T. W. & Lalanne, P. Compact antenna for efficient and unidirectional launching and decoupling of surface plasmons. *Nano Lett.* **11**, 4207-4212 (2011).

135 Liu, Y., Palomba, S., Park, Y., Zentgraf, T., Yin, X. & Zhang, X. Compact magnetic antennas for directional excitation of surface plasmons. *Nano Lett.* **12**, 4853-4858 (2012).

136 Lerosey, G., Pile, D. F., Matheu, P., Bartal, G. & Zhang, X. Controlling the phase and amplitude of plasmon sources at a subwavelength scale. *Nano Lett.* **9**, 327-331 (2009).

137 Koev, S. T., Agrawal, A., Lezec, H. J. & Aksyuk, V. A. An Efficient Large-Area Grating Coupler for Surface Plasmon Polaritons. *Plasmonics* **7**, 269-277 (2012).

138 López-Tejeira, F., Rodrigo, S. G., Martín-Moreno, L., García-Vidal, F. J., Devaux, E., Ebbesen, T. W., Krenn, J. R., Radko, I. P., Bozhevolnyi, S. I., González, M. U., Weeber, J. C. & Dereux, A. Efficient unidirectional nanoslit couplers for surface plasmons. *Nature Phys.* **3**, 324-328, (2007).

139 Xu, T., Zhao, Y., Gan, D., Wang, C., Du, C. & Luo, X. Directional excitation of surface plasmons with subwavelength slits. *Appl. Phys. Lett.* **92**, 101501 (2008).

140 Wang, Y., Wang, J., Gao, S. & Liu, C. Two-Way Directional Plasmonic Excitation with Two Unsymmetrical Metallic Slits. *Appl. Phys. Exp.* **6**, 02200 (2013).

141 Bonod, N., Popov, E., Li, L. & Chernov, B. Unidirectional excitation of surface plasmons by slanted gratings. *Opt. Express* **15**, 11427-11432 (2007).

142 Raghunathan, S. B., Gan, C. H., van Dijk, T., Ea Kim, B., Schouten, H. F., Ubachs, W., Lalanne, P. & Visser, T. D. Plasmon switching: observation of dynamic surface plasmon steering by selective mode excitation in a sub-wavelength slit. *Opt. Exp.* **20**, 15326-15335, (2012).

143 Rodriguez-Fortuno, F. J., Marino, G., Ginzburg, P., O'Connor, D., Martinez, A., Wurtz, G. A. & Zayats, A. V. Near-field interference for the unidirectional excitation of electromagnetic guided modes. *Science* **340**, 328-

330 (2013).

144 Laluet, J. Y., Drezet, A., Genet, C. & Ebbesen, T. W. Generation of surface plasmons at single subwavelength slits: from slit to ridge plasmon. *New J. Phys.* **10**, 105014 (2008).

145 Lezec, H. J. & Thio, T. Diffracted evanescent wave model for enhanced and suppressed optical transmission through subwavelength hole arrays. *Opt. express* **12**, 3629-3651 (2004).

146 Gravel, Y. & Sheng, Y. Rigorous solution for optical diffraction of a sub-wavelength real-metal slit. *Opt. Express* **20**, 2149-2162 (2012).

147 Liu, J. S., White, J. S., Fan, S. & Brongersma, M. L. Side-coupled cavity model for surface plasmon-polariton transmission across a groove. *Opt. Express* **17**, 17837-17848 (2009).

148 Kuttge, M., de Abajo, F. J. G. & Polman, A. How grooves reflect and confine surface plasmon polaritons. *Opt. Express* **17**, 10385-10392 (2009).

149 Lezec, H. J., Degiron, A., Devaux, E., Linke, R. A., Martin-Moreno, L., Garcia-Vidal, F. J. & Ebbesen, T. W. Beaming light from a subwavelength aperture. *Science* **297**, 820-822 (2002).

150 Jun, Y. C., Huang, K. C. & Brongersma, M. L. Plasmonic beaming and active control over fluorescent emission. *Nat. Commun.* **2**, 283 (2011).

151 Kocabas, A., Senlik, S. S. & Aydinli, A. Slowing down surface plasmons on a moire surface. *Phys. Rev. Lett.* **102**, 063901 (2009).

152 Bouillard, J.-S., Vilain, S., Dickson, W., Wurtz, G. A. & Zayats, A. V. Broadband and broadangle SPP antennas based on plasmonic crystals with linear chirp. *Sci. Rep.* **2**, 829 (2012).

153 Pohl, M., Belotelov, V. I., Akimov, I. A., Kasture, S., Vengurlekar, A. S., Gopal, A. V., Zvezdin, A. K., Yakovlev, D. R. & Bayer, M. Plasmonic crystals for ultrafast nanophotonics: Optical switching of surface plasmon polaritons. *Phys. Rev. B* **85**, 081401(R) (2012).

154 Wurtz, G. & Zayats, A. V. Nonlinear surface plasmon polaritonic crystals. *Laser and Photon. Rev.* **2**, 125-135 (2008).

155 Rotenberg, N., Caspers, J. N. & van Driel, H. M. Tunable ultrafast control of plasmonic coupling to gold films. *Phys. Rev. B* **80**, 245420 (2009).

156 MacDonald, K. F., Sámson, Z. L., Stockman, M. I. & Zheludev, N. I., Ultrafast

Active Plasmonics, *Nature Photon.* **3**, 55 - 58 (2009).

157 Neira, A. D., Wurtz, G. A., Ginzburg, P. & Zayats, A. V. Ultrafast all-optical modulation with hyperbolic metamaterial integrated in Si photonic circuitry. *Opt. Express* **22**, 10987-10994 (2014).

158 Dennis, B. S., Aksyuk, V., Haftel, M. I., Koev, S. T. & Blumberg, G. Enhanced coupling between light and surface plasmons by nano-structured Fabry–Pérot resonator. *J. Appl. Phys.* **110**, 066102 (2011).

159 Miroshnichenko, A. E., Flach, S. & Kivshar, Y. S. Fano resonances in nanoscale structures. *Rev. Mod. Phys.* **82**, 2257-2298 (2010).

160 Galli, M., Portalupi, S. L., Belotti, M., Andreani, L. C., O'Faolain, L. & Krauss, T. F. Light scattering and Fano resonances in high-Q photonic crystal nanocavities. *Appl. Phys. Lett.* **94**, 071101 (2009).

161 Fano, U. Effects of configuration Interaction on Intensities and Phase Shifts, *Phys. Rev.* **124**, 1866-1878 (1961).

162 Joe, Y. S., Satanin, A. M. & Kim, C. S. Classical analogy of Fano resonances. *Physica Scripta* **74**, 259-266, (2006).

163 Gallinet, B. & Martin, O. J. F. Ab initio theory of Fano resonances in plasmonic nanostructures and metamaterials. *Phys. Rev. B* **83**, 235427 (2011).

164 Avrutsky, I., Gibson, R., Sears, J., Khitrova, G., Gibbs, H. M., & Hendrickson, J. Linear systems approach to describing and classifying Fano resonances. *Phys. Rev. B* **87**, 125118 (2013).

165 Luk'yanchuk, B., Zheludev, N. I., Maier, S. A. Halas, N. J., Nordlander, P., Giessen, H. & Chong, C.T. The Fano resonance in plasmonic nanostructures and metamaterials, *Nature Mater.* **9**, 707-710 (2010).

166 Krasavin, A. V. & Zayats, A. V. Photonic signal processing on electronic scales: electro-optical field-effect nanoplasmonic modulator. *Phys. Rev. Lett.* **109**, 053901 (2012).

167 Feigenbaum, E., Diest, K. & Atwater, H. A. Unity-order index change in transparent conducting oxides at visible frequencies. *Nano Lett.* **10**, 2111-2116 (2010).

168 Krasavin, A. V. & Zayats, A. V. Three-dimensional numerical modeling of photonic integration with dielectric-loaded SPP waveguides. *Phys. Rev. B* **78**, 045425 (2008).

169 Wang, Y., Zhang, X., Tang, H., Yang, K., Wang, Y., Song, Y., Wei, T. H. & Wang, C. H. A. Tunable unidirectional surface plasmon polaritons source. *Opt. Express* **17**, 20457-20464, (2009).

170 Dionne, J. A., Sweatlock, L. A., Atwater, H. A. & Polman, A. Plasmon slot waveguides: Towards chip-scale propagation with subwavelength-scale localization. *Phys. Rev. B* **73**, 035407 (2006).

171 Lin, J., Dellinger, J., Genevet, P., Cluzel, B., de Fornel, F. & Capasso, F. Cosine-Gauss Plasmon Beam: A Localized Long-Range Nondiffracting Surface Wave. *Phys. Rev. Lett.* **109**, 093904 (2012).

172 Salandrino, A. & Christodoulides, D. N. Airy plasmon: a nondiffracting surface wave. *Opt. Lett.* **35**, 2082-2084 (2010).

173 Stockman, M. I. Nanoplasmonics: The physics behind the applications. *Physics Today* **64**, 39-44 (2011).

174 Hashizume, J. & Koyama, F. Plasmon Enhanced Optical Near-field Probing of Metal Nanoaperture Surface Emitting Laser. *Opt. Express* **12**, 6391-6396 (2004).

175 De Leon, I. & Berini, P. Amplification of long-range surface plasmons by a dipolar gain medium. *Nature Photon.* **4**, 382-387 (2010).

176 Bolger, P. M. Dickson, W., Krasavin, A. V., Liebscher, L., Hickey, S. G., Skryabin, D. V. & Zayats, A. V. Amplified spontaneous emission of surface plasmon polaritons and limitations on the increase of their propagation length. *Opt. Lett.* **35**, 1197-1199 (2010).

177 Jiang, W., Shimizu, M., Mirin, R. P., Reynolds, T. E. & Bowers, J. E. Electrically pumped mode-locked vertical-cavity semiconductor lasers. *Opt. Lett.* **18**, 1937-1939 (1993).

178 Biris, C. G. & Panoiu, N. C. Nonlinear pulsed excitation of high-Q optical modes of plasmonic nanocavities. *Opt. Express* **18**, 17165-17179 (2010).

179 Ameling, R., Dregely, D. & Giessen, H. Strong coupling of localized and surface plasmons to microcavity modes. *Opt. Lett.* **36**, 2218-2220 (2011).

180 Chen, S. M., Li, G. X., Lei, D. Y. & Cheah, K. W. Efficient energy exchange between plasmon and cavity modes via Rabi-analogue splitting in a hybrid plasmonic nanocavity. *Nanoscale* **5**, 9129-9133 (2013).